University of Strathclyde

Department of Physics

Submitted in partial fulfilment of the requirements

for the degree of Doctor of Philosophy

Applications of principal modes to imaging, control and surface enhancement in nanoparticles

Duncan McArthur

1st *Supervisor*:

Dr. Francesco Papoff

2nd *Supervisor*:

Dr. Ben Hourahine

August 2017

This thesis is the result of the authors original research. It has been composed by the author and has not been previously submitted for examination which has led to the award of a degree.

Signed:

Date:

Dedicated to my mother

Morag

and in loving memory of my father

Roddy

Acknowledgements

First and foremost, I wish to thank Ben and Francesco for all their guidance, wisdom, and kindness. I would also like to thank Hiromi, Kohei, and the researchers and students at Waseda and the IMS for their collaboration and gracious hosting. I would like to acknowledge everyone in the CNQO group at Strathclyde. In particular, Gian-Luca Oppo for recommending me as a PhD candidate and all that he has done for me since my early years as an undergraduate and Alison Yao for her encouragement, and for allowing me to finish writing up when I should have really been working. I am also grateful to Pierre-François Brevet and Yu Chen, my examiners, for providing experimental insights and thoughtful discussion regarding this work.

I cannot express the extent of my gratitude to my mother Morag, for her unwavering support, without which none of this would have been possible, and to my brother Colin, sister Caroline, and girlfriend Heather, who have always been by my side, making things better. Finally, thanks to all of my wonderful friends. And of course, Sally.

Contents

Published material

Papers published or submitted to peer-reviewed journals

- D. McArthur, B. Hourahine, and F. Papoff. "Evaluation of E. M. fields and energy transport in metallic nanoparticles with near field excitation," *Phys. Sci. Int. Jour.*, vol. 4, pp. 564-575, 2014.

- K. Imura, K. Ueno, H. Misawa, H. Okamoto, D. McArthur, B. Hourahine, and F. Papoff. "Plasmon modes in single gold nanodiscs," *Opt. Express*, vol. 22, pp. 12189-12199, 2014.

- F. Papoff, D. Mcarthur, and B. Hourahine. "Coherent control of radiation patterns of nonlinear multiphoton processes in nanoparticles," *Sci. Rep.*, vol. 5, p. 12040, 2015.

- D. McArthur, B. Hourahine, and F. Papoff. Dataset on coherent control of fields and induced currents in nonlinear multiphoton processes in a nanosphere," *Sci. Data*, vol. 2, p. 150064, 2015.

- D. McArthur, B. Hourahine, and F. Papoff. "Coherent control of plasmons in nanoparticles with nonlocal response," *Opt. Comm.*, vol. 382, pp. 258-265, 2017.

- D. McArthur, B. Hourahine, and F. Papoff. "Enhancing ultraviolet spontaneous emission with a designed quantum vacuum," *Opt. Express*, vol. 25, pp. 12189-12199, 2017.

- D. McArthur, and F. Papoff. "Gap enhanced fluorescence as a road map for the detection of very weakly fluorescent emitters from visible to ultraviolet," *Sci. Rep.*, vol. 7, p. 14191, 2017.

- B. Hourahine, D. McArthur, and F. Papoff. "Chap. 1: Principal Modes of Maxwell's Equations" in "The Generalized Multipole Technique for Light Scattering", Ed. T. Wriedt, and Y. Eremin, Springer, 2018.

Conference contributions: Talks and poster presentations

- *Light trapping states in media with longitudinal electric waves*, talk at Photon14, Conference, Imperial college, London, 2014

- *Plasmon modes in single gold nanodiscs*, poster at Photon14, Conference, Imperial college, London, 2014

- *Theory of SNOM images*, talk at Nanolight, Symposium, University of Strathclyde, Glasgow, 2013

- *Understanding the SNOM of metal nanostructures*, poster at NanoTP, Scientific Meeting, Helmholtz-Zentrum, Berlin, 2012

Papers published unrelated to this thesis

- M. Eslami, R. Kheradmand, D. McArthur, and G-L. Oppo. "Complex structures in media displaying electromagnetically induced transparency: pattern multistability and competition," *Phys. Rev. A*, vol. 90, p. 023840, 2014.

Abstract

The theory of principal modes allows a computationally efficient generalisation of Mie's analytical approach for the sphere to obtain semi-analytical solutions for general geometries with smooth surfaces. In this thesis, we apply this method to investigate a range of single and multiple particle metallic structures in the linear, non-linear and non-local response regimes outside of the quasi-static limit. We propose schemes for the coherent control of light waves and currents in metallic nanospheres, using conventional laser sources, in all three of these regimes. The conditions on the external control field we derive lead to a reduction of absorption, suppression of radiative losses and high sensitivity to small variations in the local environment, including subwavelength spatial shifts. As part of an international collaboration with researchers from Waseda University and the Institute for Molecular Science in Japan, the optical properties of single gold nanodiscs were studied by scanning near-field optical microscopy. The modal analysis indicates that the complex spatial features observed in the transmission images originate mainly from a few fundamental plasmon modes of the discs. By reformulating the principal modes in terms of Green's functions we are able to describe systems containing multiple particles, in which both particles and host medium may be inhomogeneous. Using this formalism, the enhancement of the rates of both the emission and far field radiation of dipoles placed in the gap between metallic nanorods, nanospheres, and substrates are investigated numerically. For aluminium structures, bright mode resonances are tunable over tens or hundreds of nanometres in the ultraviolet by changing the size of the nanoparticles, with far field radiative enhancements of up to three orders of magnitude. These results show that aluminium nanostructures are ideal for applications to nano lasing and label-free detection of weakly fluorescent DNA bases and proteins in the ultraviolet.

Introduction

The interaction of light with matter is fundamental to our perception of the physical world. Optical frequencies encompass the energy range where most electronic and vibrational resonances in matter occur; this is why our eyes have evolved to detect light from this narrow spectrum. As a consequence, light scattered by an object can be used not only to produce an image of that object but also to determine its chemical composition, as well as spectral and dynamical properties.

Nanophotonics is the study of the interaction of light and matter at the nanoscale, where the physical, chemical, and structural nature of matter with subwavelength dimensions controls the interactions. The study of optical phenomena related to the electromagnetic response of metals has been of particular interest, and forms a sub-field of nanophotonics termed plasmonics. Plasmons are the collective oscillations of the conduction electrons in a metal (or semiconductor). Optical waves can couple to these electron oscillations in the form of propagating surface waves or localized excitations, depending on the geometry of the system. As far back as 1957, Richie predicted the existence of self-sustained collective excitations of electrons at metal surfaces, while studying energy loss of fast electrons passing through thin metal films [1]. Two years later, Powell and Swan demonstrated experimentally the existence of these excitations [2, 3]. Optically excited plasmons are hybrid modes of optical fields and the electronic oscillations and thus are called as plasmon-polaritons [4], hereafter simply referred to as plasmons. The surface charge-density oscillations associated with surface plasmons at the interface between a metal and a dielectric can give rise to strongly enhanced optical near-fields, which are spatially confined near the metal surface, and have resonances which are strongly dependent upon the geometry

and material composition.

Plasmonics has become an important research field in optics and materials science, with various applications that utilize the unique optical characteristics of plasmonic materials, such as chemical sensors [5, 6], surface enhanced spectroscopies [7, 8, 9, 10], nano-optical devices [11, 12, 13], while carefully designed particles are the building blocks of metamaterials [14, 15, 16]. The investigation of the spectral and spatial features of plasmons is important both for understanding the basic physical properties of plasmonic materials and to develop practical and useful applications of plasmons [17, 18, 19].

To provide a theoretical understanding of these optical properties, a variety of models and methods have been developed. At the start of the 20^{th} century, Mie derived exact analytical solutions for the optical response of systems with geometries that enable the separation of variables, such as spheres or infinite cylinders [20]. These are rigorous solutions of Maxwell's equations, satisfying the boundary conditions, and predict the scattering and absorption properties for these systems, in excellent agreement with experiment. Shortly after, Gans extended this theory to include oblate and prolate spheroids, for particles smaller than the excitation wavelength, by introducing depolarization factors related to the aspect ratios of the particle along each of its axes, in order to approximate the absorption coefficients [21], obtaining expressions which closely resemble those for spheres. As a result, spherical particles have been extensively studied in both arrays, and as single particles.

However, in the quest for better confinement, larger enhancements, stronger interactions, and the possibility of observing new phenomena, more complex geometries are desired. Unfortunately, closed analytical expressions cannot be obtained for non-spherical particles and so to determine their optical properties, Maxwell's equations must be calculated numerically. The most popular methods are finite difference time domain (FDTD), the discrete dipole approximation (DDA), the finite element method (FEM) and boundary element method (BEM), as well as integral equations based on Green's functions. Each of these methods have their benefits. FDTD calculations, for example, are a computational method

based on numerically evaluating the temporal evolution of electromagnetic fields using the complementary nature, and spatial-temporal relations, of the electric and magnetic fields in Maxwell's curl equations. Dynamical information of the electromagnetic wave in the scattering system can be obtained in addition to static properties, and both complex shapes and arrangements of multiple particles can be studied. Although FDTD, as well as the other methods mentioned, can accurately predict the spectral response of arbitrarily shaped nanostructures, they employ brute-force calculations and provide little physical insight into the nature and origin of optical phenomena. Therefore, it is difficult to rationally design nanostructures with predictable plasmon resonances based on these methods.

The discrete dipole approximation (DDA) is a volume integral method, which uses a regular lattice of closely packed *dipoles* (actually polarizable points) to represent a solid scattering target of arbitrary geometry. Each dipole represents the polarizability of a small subvolume of the target material. Once the polarizabilities have been determined, typically from the lattice dispersion (as opposed to the material properties), based on the local field (including dipole-dipole coupling) the scattering properties can be easily calculated. A cubic lattice of points is employed to discretize the volume, such that the interdipole distance is much smaller than the wavelength, and for a large enough set of points such that the target volume is well approximated. This method can be highly efficient when solved with FFTs and conjugate-gradient iterations, although large targets may require a computationally prohibitive number of points, also it has trouble with particles with dimensions much smaller than the wavelength.

The finite element method (FEM), traditionally solved in the frequency domain, employs a series of partial differential equations and integrals. In this method the entire domain must be discretized, which allows for inhomogeneous materials and boundaries, and makes it very effective at calculating localized fields and solving nonlinear problems. The constitutive relations, of Maxwell's equations, are employed to express the vector wave equation solely in terms of the electric field and currents, providing a second order partial differential equa-

tion (PDE) which must be solved globally. In each element (subdivision) of the domain test functions, approximating the PDE using linear (polynomial) basis functions, are solved by minimizing the residual error in their approximation. The solution for each element is then used to formulate a set of equations to solve for the full domain. Precision can be increased by further subdivision of the domain, or by increasing the order of the basis functions.

For the boundary element method (BEM) only surfaces need be discretized, as a set of points, reducing open boundary problems to surface boundary problems. This means that far fewer computations are typically required compared with FEM, for suitable domains. The method involves expressing PDE's, in terms of scalar and vector potentials, as integrals, generally using Green's functions. The surface boundary conditions are imposed to form boundary value integrals, which are solved using a known solution of the PDE. Once the solution on the surface has been determined, the fields anywhere in space can be calculated (for linear homogeneous media). As a fundamental solution of the PDE is required, solving for inhomogenoeus or nonlinear systems can be problematic.

A recent review detailing the procedures, applications and limitations of the most popular numerical methods for nanophotonic systems can be found in Ref. [22].

For this reason, the theory of principal modes (TPM) was recently developed by my supervisors [23], Dr. Papoff and Dr. Hourahine. The TPM provides a generalisation of Mie's solutions to particles with non-spherical geometries. By orthogonalizing sets of solutions to Maxwell's equations, internal and scattered modes are defined that are correlated pair-wise at the surface of the particle, as the Mie modes of a sphere. The spatial correlation between paired modes gives a condition for describing resonances: the higher the degree of spatial correlation between a pair of principal modes on the particle surface, the more likely they are to resonate when coupled to an external field. This resonance condition is defined irrespective of the external field and is governed by the particle geometry and material composition of the particle and environment, analogous to the plasmon resonances. This theory is general, semi-analytical and can be applied

to any particle with smooth boundaries. Furthermore it can be used to define super-modes for systems containing multiple particles by hybridizing the single particle modes, including the effects of multiple scattering to all orders. This theoretical framework forms the basis for the research presented in this thesis. In particular, we use this theory of modes and resonances to investigate and describe optical phenomena in the following nanophotonic applications: near-field optical microscopy, the coherent control of nanophotonic processes, and surface enhancement effects.

Near-field optical imaging

As plasmons are confined to the surface of nanostructures, the characteristic spatial distributions of their optical fields have features which are deeply sub-wavelength at optical frequencies. Consequently, conventional (far-field) optical microscopy techniques are unable to resolve these features. The development of near-field scanning probe techniques has provided a method for observing and measuring surface plasmons locally. Near-field optical imaging techniques, in particular scanning near-field optical microscopy (SNOM), provide an opportunity to observe and measure the optical properties of plasmons directly [24], with a spatial resolution well below the diffraction limit [25, 26, 27]. In SNOM, the optical probe is maintained within the near-field of the sample, where the optical fields associated with plasmons are confined. Information about a variety of optical processes can be accessed with this technique. The correlation between hotspots for second harmonic generation and plasmon resonances have been investigated in thin gold films using SNOM [28]. And with ultrashort pulses, the characteristic features in two-photon-induced photoluminescence imaging can be attributed to plasmon waves, and related to the local density of optical states [24]. Transmission images of long thin nanorods indicate that the plasmons have both transverse and longitudinal resonances, the latter shifts spectrally as the length of the nanorod changes [29]. Similar images can be produced using techniques such as cathodoluminescence spectroscopy [30, 31], and electron energy-loss spec-

troscopy [32, 33, 34, 35]. The resonances for these types of particles are easy to assign to plasmon modes, as long rods are quasi-one-dimensional and display an "organ pipe" node structure, similar to the standing waves of a vibrating string. For more complex, higher dimensional, geometries assigning specific plasmon modes of the system to particular resonances or spatial features can be quite difficult. Standard theoretical techniques, such as FDTD and DDA, do not support the definition of modes in the calculations and so cannot offer any clarification. The TPM, on the other hand, can be a very effective tool for dealing with these types of systems.

Coherent control

The concept of coherent control was introduced in the 1980s to control molecular systems and chemical reactions. The control was originally based on the directed interference of the different quantum pathways of an optical excitation in order to specify the final state of an atom or molecule, using phase modulation [36, 37]. In nanophotonics, coherent control is similarly achieved using the interference between optical excitations and surface fields, or plasmons. The control parameters are the amplitude, phase and polarization of the optical excitation. This concept was first demonstrated theoretically in nanophotonic systems using chirped laser pulses to excite plasmons at different frequencies on planar nanostructures where, assuming the lifetime of the plasmons is greater than the pulse duration, interference effects would lead to localised hotspots [38]. Theoretical studies have subsequently investigated guiding plasmons around nanoparticle junctions [39], optimization of coupling through coherent absorption [40] and time reversal [41], and the control of second-harmonic generation using monochromatic light [42], and pulses [43]. Experimental results to tailor the optical near-field using pulse shaping have been demonstrated by several groups in linear [44, 45, 46, 47] and non-linear media [48], while interference between fields has been recently applied to show control of light with light in linear plasmonic metamaterials [49]. These methods enable a selectivity of photonic processes, where interactions can be ei-

ther enhanced, suppressed, or localised leading to possible applications in optical switching, data storage and computations [50]. Due to the characterization of the modes and their resonances, the TPM is ideal for designing coherent control schemes which target the dominant modes of a system and tailor the optical response accordingly. This has already been demonstrated for linear media, using multiple plane wave excitations to control lineshapes [51]. In this thesis, we will extend this work by considering the coherent control of the optical response of both non-linear and nonlocal media, using conventional light sources.

Surface enhanced effects

The size, shape and composition of a metallic nanoparticle affects the properties of its plasmon resonances [4]. These plasmon resonances then affect the local electromagnetic environment. The emission rates of nearby atoms, molecules or fluorophores can be strongly influenced by these effects and in some cases can result in enhancements of several orders of magnitude. These effects are widely used in spectroscopic techniques involving plasmonic materials. It is this effect which makes surface enhanced Raman spectroscopy (SERS) so effective near rough surfaces [52, 53, 54]. Taking advantage of the interaction between an emitter and its surroundings allows one to dramatically improve the detection efficiency of fluorescence. These improvements in emission have been used to enhance fluorescence collection using evanescent cavity modes [55], make a quantum dot act as a single-photon emitter [56], and design alternative photovoltaic cells [57]. Gaps between closely spaced plasmonic structures greatly increase confinement and can lead to greater increases in enhancement [58]. Such minute gaps are made by using thin layers of dielectric spacer material. Most of the study of these effects in nanophotonics has been done in the visible range with gold or silver nanoparticles [59, 60]. Many important organic molecules have a fluorescent response in the ultraviolet, at frequencies where the noble metals do not have plasma resonances. In order to enhance fluorescent signals in the ultraviolet other metals must be used, typically the *poor* metals like rhodium, gallium and aluminium. The in-

terest in aluminium in nanophotonics is relatively more recent than for gold and silver, and it is due to aluminium being abundant, low cost and with plasmon modes in the visible and the ultraviolet [61, 62, 63]. Aluminium nano clusters have strong spectral sensitivity to variation of the local dielectric constant [63] and enhanced fluorescence factors of over 80 have been reported [62]. Hence, using well designed aluminium structures, plasmonic resonances could be tuned via the particle geometry in order to enhance the emission of molecules fluorescing in the ultraviolet, leading to applications in biological/chemical sensing.

Layout of thesis

We will begin by reviewing the theory of principal modes in Chap. 1, for single and multi-particle systems. This will introduce the framework that we will use throughout this thesis. In Chap. 2, we will discuss the origins and operations of SNOM, including the modelling of a near-field probe excitation, and apply the principal modes to investigate the complex spatial distributions observed in the near-field transmission images of various gold nanodiscs. Schemes for the coherent control of principal modes will be discussed in Chap. 3, and we will derive conditions for control in both nonlocal and non-linear media. Next, in Chap. 4, we will derive Green's functions, using the principal modes, to describe systems containing multiple disjoint particles, in which both the particles and host medium may be inhomogeneous. With these Green's functions, we will investigate how the surface enhanced fields of nanostructures can affect the emission rates of nearby dipoles. Finally, we will conclude with a summary of the results, and a discussion of future work.

Chapter 1

Principal modes of Maxwell's equations

In this Chapter we review the theory of principal modes, which provides the theoretical framework used throughout this thesis, that has been recently developed for particle geometries without sharp edges [23]. This theory employs partial differential equations evaluated at the surface of the particles, and requires that the surface normal can be defined, and the 1^{st} order derivatives of the fields can be calculated, at any point on the surface. The mathematical theory of angles between subspaces of functions [64, 65] is used to highlight the profound relation between resonances and the geometry of function spaces in Maxwell's equations. With this theory we can predict resonances of particles, independently of the particular incident field, calculate near and far field properties of optical modes and optimise their excitation with appropriate incident fields. We will then show that this theory can be used to define supermodes of multiple particles, and investigate the collective resonances of this type of system.

1.1 Principal modes of single particles

The theory of principal modes can be applied to metallic and dielectric particles without sharp edges. When all the characteristic dimensions of the particle (and the skin depth in the case of metallic particles) are larger than the free propagation

length of charges, local macroscopic permittivities and susceptibilities describe the interaction between light and the matter inside the particle.

The energy scattered by a particle propagates towards infinity [66], and the tangential components of electric and magnetic fields E, H are continuous at the particle boundaries. Hence, for any incident field, the internal and scattered fields are determined by finding the solutions of Maxwell's equations in the internal and the external media that satisfy the boundary conditions. We use vectors $F = [E, H]^{\mathrm{T}}$ with six component for electromagnetic fields [67]; in the case of a local macroscopic permittivity and susceptibility, the tangential components, together with the radiation condition then fully determine the boundary conditions for valid solutions to Maxwell's equations. Hence only the projections, f, of the six components of the field onto the boundary of the particle are required. These surface fields have four components, two electric and two magnetic, and form a space, $\mathcal{H}$, with scalar products that are defined in terms of overlap integrals on the surface of the particle,

$$f \cdot g = \int_S f_j^* g_j \mathrm{d}S \ , \tag{1.1}$$

where $\boldsymbol{f}^*$ is the complex conjugate of f, j labels the components and we sum over repeated indexes. In this notation the boundary conditions become

$$f^0 = f^i - f^s \ , \tag{1.2}$$

which can be interpreted geometrically in $\mathcal{H}$: the projection, f^0, of the incident field, $F^0(x)$, onto the surface is equal to the difference between the projections of the internal and scattered fields, f^i and f^s. Therefore, an incident field with small tangential components can excite large amplitude internal and scattered surface fields, provided that both of these two fields closely match (nearly cancelling each other at the surface). This happens when the difference between these two fields, and therefore the "angle" between them, is small. These angles are rigorously defined as being between solutions of Maxwell's equations for the internal and external media; these solutions are standing and outgoing waves, respectively, and form two subspaces of $\mathcal{H}$. The electromagnetic response of each particle

is completely characterised by these angles and their associated waves, which can be calculated with arbitrary precision from *any* complete set of solutions of Maxwell's equations for the internal and external media.

Several sets of exact solutions of the Maxwell equations are linearly independent and complete [66, 68] on Lyapunov surfaces. Such surfaces are mathematically characterised by the following three conditions: the surface normal is well defined at every point; the angle between the normals at any two points on the surface is bounded from above by a function of the distance between these points; all the lines parallel to a normal at an arbitrary point on the surface intercept only once the patches of surface contained in balls centred at the point and smaller than a critical value [69].

We use two sets of electric and magnetic multipoles, $\{\tilde{i}_n\}_{n=1}^{\infty}$ for internal fields and $\{\tilde{s}_n\}_{n=1}^{\infty}$ for scattered fields, centred at points within the particle [70, 71]. Any function in $\mathcal{H}$ can be approximated to arbitrary precision by a finite and sufficiently large number of multipoles [72]. In other words, $\{\tilde{i}_n\}_{n=1}^{\infty} \cup \{\tilde{s}_n\}_{n=1}^{\infty}$ is complete and no function in this set is the closure of the linear combinations of all the remaining functions. We note that both the internal and scattered fields exist at the surface of real metallic and dielectric particles, *i.e.* the union of internal and scattered fields provides completeness in the space $\mathcal{H}$ of the surface fields f. Neither the scattered or the internal fields separately are complete. An example of this property is given by spherical particles, where both internal and scattered modes are necessary to form the complete basis that underpins Mie theory.

For numerical applications, we could use any set of solutions of the Maxwell equations which satisfy the Silver-Müller radiation conditions [73, 74] in the external region and form standing waves in the interior. For time harmonic fields, the Silver-Müller radiation conditions are,

$$\boldsymbol{E}(\boldsymbol{r}) \times \hat{\boldsymbol{r}} + \sqrt{\frac{\mu_0}{\varepsilon_0}}\boldsymbol{H}(\boldsymbol{r}) = 0 + \mathcal{O}(1/r^2), \tag{1.3}$$

$$\boldsymbol{H}(\boldsymbol{r}) \times \hat{\boldsymbol{r}} - \sqrt{\frac{\varepsilon_0}{\mu_0}}\boldsymbol{E}(\boldsymbol{r}) = 0 + \mathcal{O}(1/r^2), \tag{1.4}$$

for $r = |\boldsymbol{r}| \to \infty$. These two expressions are equivalent and are sufficient for the existence of unique solutions to the scattering problem, containing only outgoing

waves. They also imply that fields evaluated approaching infinity are *radiating* solutions (*i.e.* the radial dependence of the Poynting vector $\boldsymbol{S} = (\boldsymbol{E}\times\boldsymbol{H}) \propto 1/r^2$). The results shown here are derived using distributed multipoles [66].

We can show [72] that the coefficients of the internal and scattered fields, $\{\tilde{a}_n^i, \tilde{a}_n^s\}$, that minimise the discrepancy between an incident field and the expansion of internal and scattered fields,

$$\left| f^0 + \sum_{n=1}^{N} \tilde{a}_n^s \tilde{\boldsymbol{s}}_n - \tilde{a}_n^i \tilde{\boldsymbol{i}}_n \right| , \tag{1.5}$$

are the solutions of

$$\begin{bmatrix} \tilde{\Upsilon}^\dagger\tilde{\Upsilon} & \tilde{\Upsilon}^\dagger\tilde{\Xi} \\ \tilde{\Xi}^\dagger\tilde{\Upsilon} & \tilde{\Xi}^\dagger\tilde{\Xi} \end{bmatrix} \begin{bmatrix} \tilde{\mathbf{a}}^i \\ -\tilde{\mathbf{a}}^s \end{bmatrix} = \begin{bmatrix} \tilde{\Upsilon}^\dagger f^0 \\ \tilde{\Xi}^\dagger f^0 \end{bmatrix} , \tag{1.6}$$

with $\tilde{\mathbf{a}}^{i/s} = [\tilde{a}_1^{i/s}, .., \tilde{a}_N^{i/s}]^{\mathrm{T}}$ and $\tilde{\Upsilon}, \tilde{\Xi}$ being matrices whose columns are the functions $\{\tilde{i}_n\}_{n=1}^N$ and $\{\tilde{s}_n\}_{n=1}^N$. The Gram matrix on the left of Eq. (1.6), *i.e.* the matrix of all possible inner products, can always be inverted because the functions used are linearly independent and complete. However, the inversion is numerically challenging [71] and for this reason this approach has received little attention. Instead, we exploit the block structure of the matrix in Eq. (1.6) to give a complete characterisation of the geometry of the internal and scattered fields and analytical expressions for the expansion coefficients of the fields.

First, we find orthogonal modes for the scattering and internal fields: for any number, N, of multipoles, we obtain orthogonal modes through the matrix decomposition

$$\tilde{\Upsilon} = U^i Q^i, \tag{1.7}$$

$$\tilde{\Xi} = U^s Q^s, \tag{1.8}$$

where Q^i, Q^s are invertible matrices determined through SVD or QR decomposition [75, 76] and U^i, U^s are unitary matrices whose columns are the orthogonal internal and scattering modes respectively. Scalar products between internal and scattering modes form a matrix with the decomposition

$$U^{i\dagger} U^s = V^i C V^{s\dagger} , \tag{1.9}$$

where C is a diagonal matrix with positive elements, and V^i, V^s are unitary matrices acting on the internal and scattered fields, respectively.

By using the identities in Eqs. (1.7,1.8), the Gram matrix in Eq. (1.6) can be rewritten as

$$\begin{bmatrix} Q^{i\dagger}U^{i\dagger}U^iQ^i & Q^{i\dagger}U^{i\dagger}U^sQ^s \\ Q^{s\dagger}U^{s\dagger}U^iQ^i & Q^{s\dagger}U^{s\dagger}U^sQ^s \end{bmatrix}, \tag{1.10}$$

upon which we perform the following unitary transformation,

$$\begin{bmatrix} V^{i\dagger}Q^{i\dagger^{-1}} & 0 \\ 0 & V^{s\dagger}Q^{s\dagger^{-1}} \end{bmatrix} \begin{bmatrix} Q^{i\dagger}U^{i\dagger}U^iQ^i & Q^{i\dagger}U^{i\dagger}U^sQ^s \\ Q^{s\dagger}U^{s\dagger}U^iQ^i & Q^{s\dagger}U^{s\dagger}U^sQ^s \end{bmatrix} \begin{bmatrix} Q^{i^{-1}}V^i & 0 \\ 0 & Q^{s^{-1}}V^s \end{bmatrix} \tag{1.11}$$

$$= \begin{bmatrix} V^{i\dagger}Q^{i\dagger^{-1}}Q^{i\dagger}U^{i\dagger}U^iQ^iQ^{i^{-1}}V^i & V^{i\dagger}Q^{i\dagger^{-1}}Q^{i\dagger}U^{i\dagger}U^sQ^sQ^{s^{-1}}V^s \\ V^{s\dagger}Q^{s\dagger^{-1}}Q^{s\dagger}U^{s\dagger}U^iQ^iQ^{i^{-1}}V^i & V^{s\dagger}Q^{s\dagger^{-1}}Q^{s\dagger}U^{s\dagger}U^sQ^sQ^{s^{-1}}V^s \end{bmatrix}. \tag{1.12}$$

Using the properties of the component matrices, $AA^\dagger = A^\dagger A = \mathbb{I}$ for orthonormal matrices (U and V) and $BB^{-1} = B^{-1}B = \mathbb{I}$ for invertible matrices (Q) where $\mathbb{I}$ is the identity matrix, we can reduce Eq. (1.12) to

$$\begin{bmatrix} \mathbb{I} & V^{i\dagger}U^{i\dagger}U^sV^s \\ V^{s\dagger}U^{s\dagger}U^iV^i & \mathbb{I} \end{bmatrix}. \tag{1.13}$$

Finally, applying the decomposition of Eq. (1.9) to the off-diagonal terms in the above matrix results in the much simplified form of the Gram matrix

$$\begin{bmatrix} \mathbb{I} & V^{i\dagger}V^iCV^{s\dagger}V^s \\ V^{s\dagger}V^sC^\dagger V^{i\dagger}V^i & \mathbb{I} \end{bmatrix} = \begin{bmatrix} \mathbb{I} & C \\ C^\dagger & \mathbb{I} \end{bmatrix}. \tag{1.14}$$

We now perform a similar procedure upon the right-hand side of Eq. (1.6), again substituting in Eqs. (1.7,1.8) and applying the same transformation

$$\begin{bmatrix} V^{i\dagger}Q^{i\dagger^{-1}} & 0 \\ 0 & V^{s\dagger}Q^{s\dagger^{-1}} \end{bmatrix} \begin{bmatrix} Q^{i\dagger}U^{i\dagger}f^0 \\ Q^{s\dagger}U^{s\dagger}f^0 \end{bmatrix} = \begin{bmatrix} V^{i\dagger}U^{i\dagger}f^0 \\ V^{s\dagger}U^{s\dagger}f^0 \end{bmatrix}, \tag{1.15}$$

which leads to the original matrix equation, Eq. (1.6), becoming

$$\begin{bmatrix} \mathbb{I} & C \\ C^\dagger & \mathbb{I} \end{bmatrix} \begin{bmatrix} \mathbf{a}^i \\ -\mathbf{a}^s \end{bmatrix} = \begin{bmatrix} \Upsilon^\dagger f^0 \\ \Xi^\dagger f^0 \end{bmatrix}. \tag{1.16}$$

On the right-hand side of Eq. (1.16), $\Upsilon = U^i V^i$ and $\Xi = U^s V^s$ are matrices whose columns are formed by the so called principal internal and scattering modes, $\{i_n\}$ and $\{s_n\}$, which are one of the main tools in this theory. The coefficients of the principal modes in the fields' expansions are $\mathbf{a}^i$ and $\mathbf{a}^s$.

We can understand the above procedure as a (repeated) change of basis for describing the electromagnetic fields of the excited particle. The first, using only the decompositions of Eqs. (1.7,1.8), forms an orthonormal basis which enables us to determine the coefficients $\tilde{\mathbf{a}}^i$ and $\tilde{\mathbf{a}}^s$, using the method of least squares, and solve the scattering problem (see Appendix A for an example). In this basis, however, each scattering mode is coupled to, potentially, every internal mode and vice-versa. The second change of basis, via the unitary transformations and decomposition of Eq. (1.9), ensures that, as C is a diagonal matrix, the principal modes are coupled pairwise, *i.e.* each mode is orthogonal to all but at most *one* mode in the other space. This is the essential feature of this theory, which is also the main property of the Mie modes of spheres. As a result, we can gain valuable information about the behaviour of individual mode pairs for arbitrary particle geometries (without sharp edges), as shall be discussed throughout this thesis.

The principal angles, ξ_n, between s_n and i_n are defined in terms of the positive diagonal elements of C as

$$i_n \cdot s_n = \cos(\xi_n) \; . \tag{1.17}$$

The terms on the right-hand side of Eq. (1.17) are the principal cosines [64]: $\cos(\xi_n)$ and $\sin(\xi_n)$ are the statistical correlation [77] and the orthogonal distance between s_n and i_n respectively. Note that the spatial correlation of two modes is defined by an integral over the particle surface for the scalar product of their projections. In other words, each scattering mode, s_n, is spatially correlated to only *one* internal mode, i_n, and vice versa at the particle boundary.

The angles $\{\xi_n\}$ are invariant under unitary transformation [65] and completely characterise the geometry of the subspaces of the internal and scattered solutions in $\mathcal{H}$. This geometry is generated by the specific scattering particle through the surface integrals of the scalar products. Principal cosines are important for two reasons: they provide analytic equations for the coefficients of the

internal and scattered principal modes, generalising the Mie formulae and clarifying the nature of all scattering channels of a particle; they allow us to reduce large matrices to their sub-blocks and eliminate the need for numerical inversion in the determination of the mode coefficients. We give more details for the numerical process of calculating the principal modes in Appendix A, comparing the stability and performance of the discrete source method solved by QR factorisation against two numerical schemes to form the unitary transformations required to obtain the scattering problem in the form of Eq. (1.16).

For spherical particles, each pair of modes can be divided into two categories, the electric multipoles (transverse magnetic modes) having magnetic fields with null radial components, and the magnetic multipoles (transverse electric modes) having electric fields with null radial components. As a consequence of the spherical symmetry, the modes in each of these sets can be labelled with two discrete indices, l and m, which are related to the eigenvalues of the total angular momentum and of the angular momentum along z, respectively. Electric and magnetic multipoles are divergence free, *i.e.* the condition $\nabla \cdot E = 0$ applies. From Maxwell's equations [78], we can find that this condition has two physical consequences: these modes cannot produce a charge density inside the medium in which they are supported; furthermore, at each point in space the electric fields of these modes are orthogonal to the local wave vector. When the response of the system is local, for example in the case that the current density at any point inside a metallic particle depends only on the electric field at that point, the interaction of the particle with light is fully described by these electric and magnetic multipoles. More specifically, internal and scattering electromagnetic fields are expanded in terms of electric and magnetic multipoles: in spherical coordinates the internal and external electric (magnetic) multipoles of indexes l, m have the same angular dependence, while the radial dependence is a function of the medium in which the multipole is defined. As a result of the spherical symmetry, the surface integral of the scalar product of a mode with the complex conjugate of another mode, *i.e.* the spatial correlation at the surface, is non-null only if the two modes are both transverse electric or transverse magnetic and

have the same value of l and m. This property can be used to find the amplitudes of the modes by imposing the continuity of the tangent components of the electric and magnetic fields at the surface of the sphere and identifying the principal modes for the internal and scattered fields that are correlated at the surface. For non-spherical particles, instead, principal modes are linear superpositions of multipoles (although in some cases one multipole can be dominant).

We can now interpret the interaction of particles with light in terms of eigenvalues and orthogonal eigenvectors, $w_n^{\pm} = (i_n \pm s_n)/\sqrt{2}$, of the Hermitian operator in Eq. (1.16). This provides useful analogies between the electromagnetic response of classical particles with the quantum-mechanical response of atoms or molecules. In experiments however, we measure either the internal or scattered fields so, transforming the eigenfunctions, $\{w_n^{\pm}\}$, we find the principal modes' coefficients:

$$a_n^i = \frac{i_n - \cos(\xi_n) s_n}{\sin^2(\xi_n)} \cdot f^0 = \frac{i'_n}{i'_n \cdot i_n} \cdot f^0, \tag{1.18}$$

$$a_n^s = -\frac{s_n - \cos(\xi_n) i_n}{\sin^2(\xi_n)} \cdot f^0 = -\frac{s'_n}{s'_n \cdot s_n} \cdot f^0. \tag{1.19}$$

Here $i'_n = i_n - \cos(\xi_n) s_n$, $s'_n = s_n - \cos(\xi_n) i_n$ are biorthogonal to i_n, s_n ($i'_n \cdot s_n = s'_n \cdot i_n = 0$) with $i'_n \cdot i_n = s'_n \cdot s_n = \sin^2(\xi_n)$. Either the principal or the biorthogonal modes fully specify the response of the particle at any point inside, on the surface and outside the particle. A graphical representation of the principal and the biorthogonal modes is shown in Fig. (1.1). A pair of (normalised) principal modes, and their bi-orthogonal counterparts, are depicted on a unit circle highlighting the angles between them and the importance of the bi-orthogonal modes in defining the scattering mode amplitudes, Eq. (1.19). From this graphical representation we can see that an incident field (with unit amplitude) which perfectly matches the spatial distribution of the scattering mode (on the surface of the particle) will produce an excitation of the scattering mode with a unit amplitude, while an incident field which matches the spatial distribution of the bi-orthogonal mode will instead excite the maximum possible amplitude for that particular scattering mode, see Sec. 3.1.2 for further discussion. This is shown by

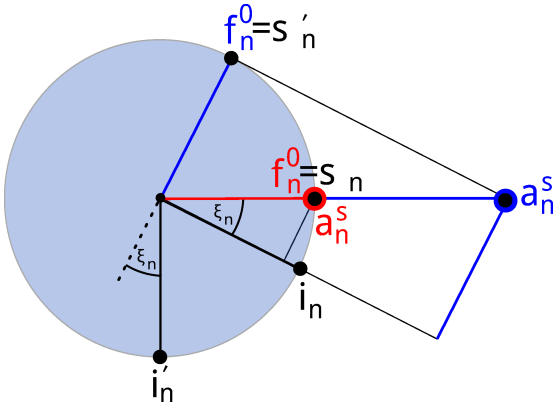

Figure 1.1: Schematic of one pair of principal modes of a nano-structure interacting with different incident fields. All modes and incident fields have been normalised to unit magnitude (the marked circle). For a given incident field, F^0, the amplitudes $(a_n^s,\, a_n^i)$ of the scattered and internal mode $(s_n,\, i_n)$ pair are given by the triangle with sides of $a_n^s s_n$, $a_n^i i_n$ and the component of the incident field in this plane, f_n^0. We can see that a field of magnitude 1 with f_n parallel to s_n induces amplitudes $a_n^s = 1$, $a_n^i = 0$—shown in red—while a unit field with f_n parallel to s'_n (and orthogonal to i_n) induces the largest amplitude possible for a_n^s from a unit magnitude incident field, along with a non-vanishing internal amplitude a_n^i—in blue. Equivalently [79], the amplitudes are proportional to the scalar products of the incident field with the biorthogonal modes i'_n and s'_n.

recasting the expansions of internal and scattered field as

$$\begin{aligned} F^{s/i}(x) =& G_S(x,s)\cdot f^0(s)\ , \\ =& \left(\frac{\mathcal{T}^i(x) I_n(x) i'_n(s)}{i'_n\cdot i_n} - \frac{\mathcal{T}^s(x) S_n(x) s'_n(s)}{s'_n\cdot s_n}\right)\cdot f^0(s)\ , \end{aligned} \tag{1.20}$$

where $G_S(x,s)$ is the surface Green's function [72, 67] of the particle and the indicator function $\mathcal{T}^i(x)$ $(\mathcal{T}^s(x))$ is 1 inside (outside) the particle and null elsewhere. In numerical calculations, propagation of the fields away from the surface $(I(x)$ and $S(x))$ is performed for Eq. (1.20) at a very low computational cost by evaluation of known solutions of Maxwell's equations, *i.e.* of Bessel or Hankel functions and vector spherical harmonics. From Eq. (1.20) we can see that the convergence of principal modes and principal angles as $N \to \infty$ is a consequence of the convergence of the surface Green's function [72] for any complete set of solutions of the Maxwell equations. We can monitor this convergence with the

surface residual

$$\left| f^0 + \sum_{n=1}^{N} a_n^s s_n - a_n^i i_n \right| , \tag{1.21}$$

which provides an upper bound for the maximum error in the scattered and internal fields that decreases with the distance from the surface [66, 80]. Furthermore, the form of Eqs. (1.18, 1.19) remains unchanged as $N \to \infty$, even if ξ_n, i_n, s_n change. The angles relevant to this work are the point angles $0 < \xi < \pi/2$ of the infinite dimensional theory [65], together with the corresponding subspaces (principal modes) and their orthogonal complements (biorthogonal modes).

The modal decomposition in Eq. (1.20) has several unique advantages. The left-hand terms in the scalar products depend exclusively on the particle, *i.e.* are independent of the particular incident field, which enables us to strongly reduce the number of modes used in the calculations by finding the modes that are coupled to a given exciting field and discarding the others. Similarly this also allows the optimisation of an incident field to excite a specific principal mode, or combination of modes. We remark that a_n^i, a_n^s in Eq. (1.18) and Eq. (1.19) are calculated by projecting the incident field f^0 onto non-orthogonal vectors, i_n and s_n, while $\sin(\xi_n)$ is defined as the Petermann factor in unstable optical cavities [81], which gives the order of magnitude of transient gain and excess noise.

The modes of a cavity can be decomposed as a pair of counter-propagating waves. The Petermann factor K for each mode can be defined as the product of the integrals of the absolute values of the (spatially varying complex) amplitudes of the counter-propagating waves squared, normalised by the correlation integral of the product of the two amplitudes, where the integration is performed over the entire beam cross-section. For stable cavity modes, which are power orthogonal[1], this factor is effectively unity ($K \approx 1$) when the mode is appropriately normalized. However, in unstable cavities, where the modes are non-power orthogonal, if the two counter-propagating waves have very different waveforms (e.g. converging

[1]When modes are power orthogonal, the total power is the sum of the power in each mode. When modes are non-power orthogonal, the total power contains also cross-terms between modes.

vs. diverging) the correlation intergal in the denominator may approach zero, making (very) large K factors possible for that mode. This is (the mathematical description of) the source of gain and excess noise in these types of cavities.

Therefore the existence of strongly aligned vectors with $\sin(\xi_n) << 1$ determines large surface fields in nano-particles as well as large transient gain and excess noise [82] in macroscopic unstable cavities and dissipative systems governed by non-Hermitian operators [83]. Macroscopic cavities and scattering particles are open systems in which both internal and external modes are necessary to provide a full description of the interaction with the environment: reducing the theory to one set of modes implies loss of information, and this is the origin of the similarities of these systems. Mathematically, as a consequence of oneness and losses, internal and scattered principal modes are not modes of a Hermitian operator and their optimal excitation is given by the corresponding biorthogonal modes. Physically, the biorthogonal modes are surface fields that are either totally reflected or totally absorbed. The experimental realisations of these surface fields may be challenging (see Sec. 3.4 for one approach), but they can be used theoretically to find and optimise incident fields able to couple to the principal modes. For well aligned mode pairs (small ξ_n), the coefficients a_n^i, a_n^s are of the same order, but this is not the case for weakly aligned pairs ($\xi_n \to \pi/2$), which can have qualitatively different absorption and scattering cross sections. Furthermore, modes can have null amplitudes for *specific* incident fields but couple well to other incident fields, see Eq. (1.18) and Eq. (1.20).

To completely determine the response of particles to electromagnetic fields, we need also to assess the ability of principal modes to transport energy. This is determined by the integral of the Poynting vector of each mode over the surface of the particle,

$$\Phi_n^{s/i} = \int_s Re\left(\hat{n}^{s/i} \cdot E_n^{s/i} \times H^{s/i*}_n\right) \mathrm{d}s \,, \tag{1.22}$$

where $\hat{n}^{s/i}$ is the outward (inward) pointing normal to the surface for scattered (internal) modes and $E_n^{s/i}, H_n^{s/i}$ are the electric and magnetic components of the principal mode with $|a_n^{i/s}| = 1$. Radiative modes that are very effective at transporting energy from the particle surface to infinity are identified by large values

of this "intrinsic" mode flux, Φ_n^s, while small values correspond to modes that can only transport energy effectively in the surface's vicinity. Similarly, strongly (weakly) absorbing modes are identified by large (small) values of Φ_n^i.

This theory generalises the definition of Mie resonances to any particle without sharp edges and is computationally efficient. Principal modes and scalar products depend on the size parameters of the particle and the frequency dependent permittivity and susceptibility of the particle; as a consequence, the principal angles, $\{\xi_n\}$, vary with the frequency of incident light. The mode coefficients diverge when the denominators of Eq. (1.18) and Eq. (1.19) vanish. This happens when a pair of normalised internal and scattering modes are perfectly parallel. For a sphere it can be shown by factoring out the angular dependence of the modes that this condition is the usual Mie resonance condition, which can be interpreted geometrically in terms of alignment between internal and scattered modes [51]. For spheres, the resonance $i_n = s_n$ occurs at complex wavelengths; for real wavelengths, resonances correspond to minima of the principal angles. This holds true for any smooth non-spherical particle, because perfect alignment is impossible with the linear independence and completeness of the principal modes. Therefore, as with spherical particles [84], physical resonances correspond to minimum angles ($\xi_n \neq 0$) of pairs in $\mathcal{H}$, which are also minima of the eigenvalues of the Hermitian operator in Eq. (1.16).

We also need to consider the energy transported by resonances. A resonant pair of modes can have very different values of Φ_n^s and Φ_n^i, which means that the effect of the resonance can be strong or weak depending on whether the detection is made in the near or far field, or if scattering or absorption are measured. Note that the total flux of energy scattered or absorbed by non-spherical particles (integrals of the Poynting vector over all directions) is given by the sum of principal mode contributions plus interference terms between modes, which are absent for spherical particles. Interference terms are absent in spheres because both surface fields and power fluxes of Mie modes are orthogonal, as a consequence of spherical symmetry. Hence for non-spherical particles, interference effects can lead to strong efficiency peaks or to sharp asymmetric features resulting from

Fano-like interference between broad and narrow resonances. Examples of these phenomena are given in the following.

In terms of numerical calculations, this approach is a surface method that relies on the convergence of

$$\left\{ \sum_{n=1}^{N} a_n^i I_n, \sum_{n=1}^{N} a_n^s S_n \right\} \tag{1.23}$$

to the exact fields at any point inside and outside the particle [67, 72] as $N \to \infty$. Eq. (1.21) gives the numerical error in the evaluation of the surface fields; in practice the scattered power is calculated both at infinity and on the surface of the particle to estimate the error in the field propagation, *i.e.* in the evaluation of the special functions. The Stratton-Chu relations [85] can also be used to test both the propagation of the scattered light and also the reliability of the internal field [76].

Calculations were compared with Mie theory [19] for metallic spheres, in Ref. [23], and demonstrated that this method is numerically very accurate for particles with radii between 10^{-2}–4×10^{0} times the wavelength of light.

1.2 Optical resonances of single particles

As the size of the particle becomes comparable to, or smaller than, the wavelength of light, the geometric description of resonances as closed orbits of light rays [86] becomes less and less effective, eventually requiring the solution of Maxwell's equations. Analytical solutions [20, 87], based on symmetry and separation of coordinates, provide exact results for a few specific shapes of particle. For spheres, electric and magnetic multipoles are used to expand internal and scattered fields and each multipole in one field is correlated only to the corresponding multipole in the other field. Resonances depend on the size of the particle and on the dielectric permittivity and magnetic permeability of the internal and external media and occur when the correlation of one pair of modes reaches a maximum. However, it is important to realise that a resonance can be observed only if the incident light has the appropriate frequency *and spatial structure* on the surface of the particle,

otherwise the incident field does not couple to the resonant modes of the internal and scattered fields.

For particles of arbitrary shape, resonances are often defined empirically by maxima in properties such as the far field extinction or scattering efficiency spectra. While there are several methods that can find spectra and their maxima [88], this approach to resonances is unsatisfying because it fails to disentangle the intrinsic properties of the resonance from those of the incident field, and depends on an arbitrary choice of the property which is monitored to determine the resonance. For instance, a resonance of a surface mode that does not efficiently transport energy to infinity, would not be distinguishable in any far field measure; these resonances, however, can be extremely important in near field applications or through interference with radiative modes able to transport energy into the far field. We use the principal modes of Sec. 1.1 to define field expansions and resonances for any smooth particle, where Mie's treatment of the sphere is a special case of this more general theory.

For all particles presented in this section a fitted dielectric function [89, 90] for gold was used.

1.2.1 Gold nano-rods

We examine here light interaction with a type of particles extensively used in experiments, gold particles. For simplicity, we consider these particles in vacuum without considering supporting substrates. The calculations presented for rounded cylinders have been verified by comparison with prolate ellipsoids using a Mie-Gans code, which provides an analytical estimate of the efficiencies, where both exhibited very similar behaviour.

As a consequence of the axial symmetry of these particles, all fields in the problem can be decomposed into components with a well defined azimuthal angular dependence, $\exp im\phi$, where m is a natural number. In the case of axially incident plane wave light, functions transforming as $m = \pm 1$ fully describe the incident light and the optical response of the particle.

Figure (1.2a) and Fig. (1.2b) shows the calculated optical efficiencies and

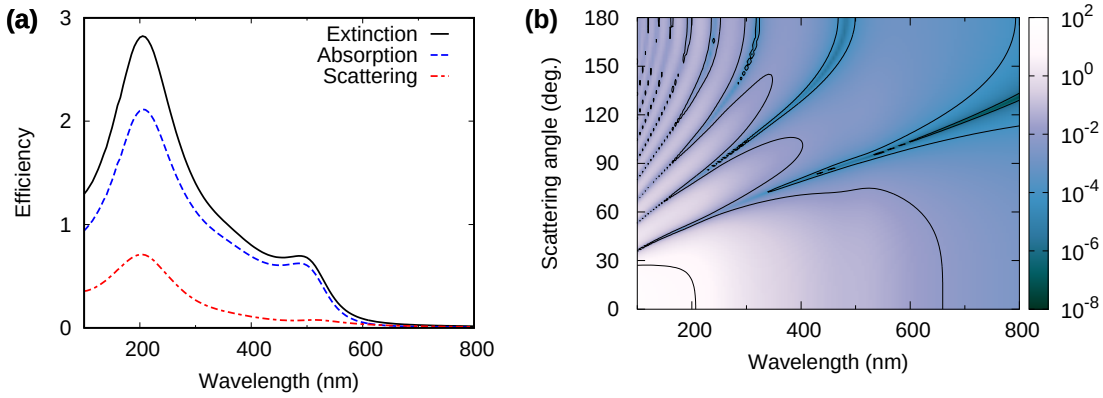

Figure 1.2: a) Scattering, absorption and extinction efficiencies of the gold rod showing the 205 nm mode and weaker absorption peak at 486 nm. Other resonances can be excited for different angles of incidence. b) DSCS showing that this particle has strong forward scattering.

differential scattering cross section (DSCS) of a 480 nm long rod with diameter 40 nm, illuminated with plane-wave light incident along its axis. The dominance of absorption over scattering for these particles can be intuitively understood in terms of resistance. In a homogeneous conductor, with a uniform cross-section (as is the rod, except for the semi-spherical end-caps), the resistance depends inversely upon the cross-sectional area. Therefore, we would expect thin rods to have a larger resistance, and hence be more dissipative or absorbing, than thick rods, or spheres (of the same scale as the long dimension of the rod). There is a strong resonance at 205 nm and a weaker absorption peak at ∼515 nm. The DSCS shows that the incident light is strongly forward scattered, particularly at short wavelengths.

We see from Fig. (1.3a) and Fig. (1.3d) that most mode pairs are either strongly radiative or absorbing, with the exception of one weakly aligned pair that is both absorbing and radiating. The peak at 205 nm results from the constructive interference of several weakly aligned principal mode pairs as shown by Fig. (1.3c). Most of these mode pairs are weakly radiating in the far field and collectively they very efficiently extract energy from the incident field. Interference between scattering modes leads to enhanced sensitivity to perturbations near to the scattering surface, therefore these multi-mode resonances can be very advantageous in sensing applications. A few modes cause the absorption feature

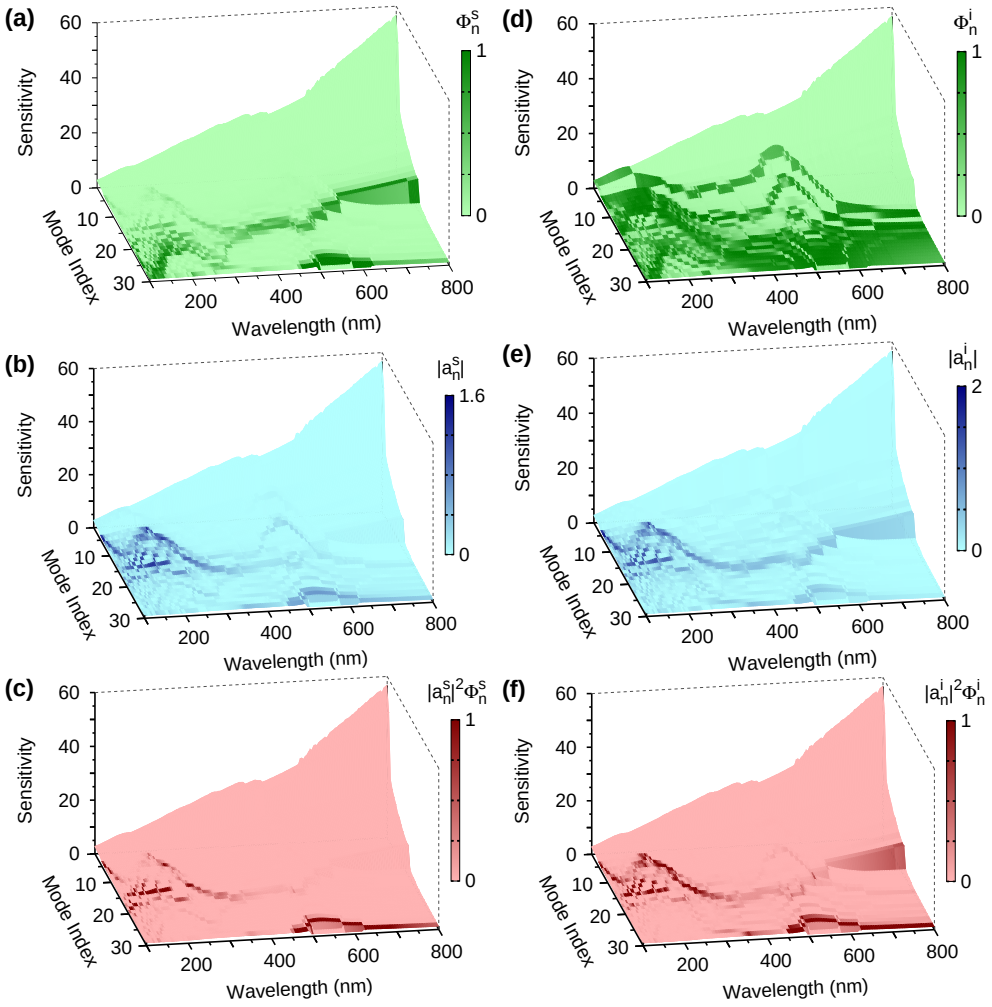

Figure 1.3: Principal angle landscapes of a rounded nano-rod: mode pairs are plotted according to their principal cosines (mode index), the wavelength of the incident light, and sensitivity $(\sin^2(\xi))^{-1}$, the largest possible values of $|a_n^{i/s}|^2$ for $|f^0| = 1$. Landscapes are overlaid with traces colour coded according to: a) the intrinsic mode fluxes, Φ_n^s, normalised for each wavelength to the range $[0, 1]$, b) the amplitudes $|a_n^s|$, c) the mode fluxes $|a_n^s|^2\Phi_n^s$ again normalised to $[0, 1]$. d)–f) as a)–c) but for internal modes. Discontinuities in the traces are due to crossings between different modes which occur when the values of their principal cosines become degenerate, leading to a change in ordering of the mode indices. b) and c) show that a multi-mode resonance produces the peak at 205 nm, with several principal modes contributing similarly to the scattered power. A group of internal modes, which become more aligned at 515 nm, determine the weak absorption peak around this wavelength. In these pairs internal and scattering modes couple differently to the incident field the radiative mode with the weakest alignment dominates the far field, as shown in c).

at ∼515 nm. Two of these modes are weakly aligned and absorb comparable

amounts of energy ; they become more strongly aligned at around this resonance. The scattering mode of the pair with the weakest alignment is instead dominant, as shown in Fig. (1.3c), where the resonance at ∼515 nm is enhanced, but in absolute terms this resonance is barely observable in the far field scattering efficiency of Fig. (1.2a) at that wavelength.

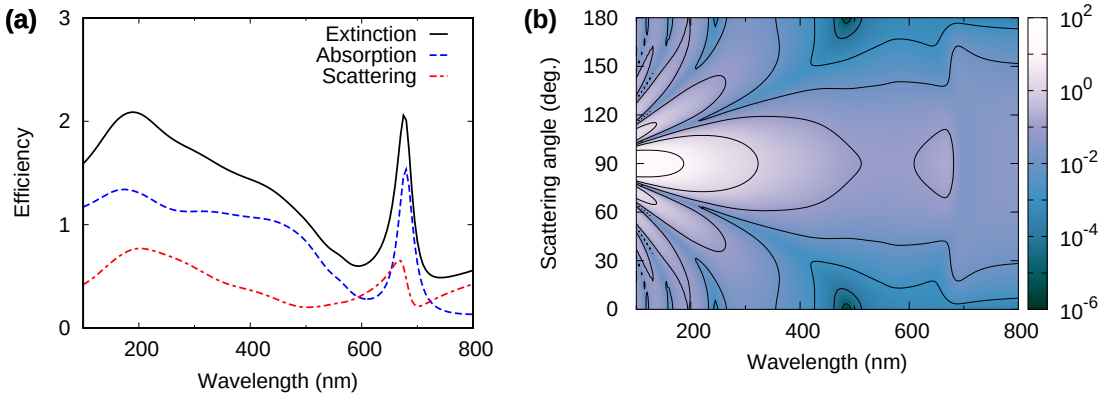

Figure 1.4: The particle from Fig. (1.2), but now illuminated from the side with an incident light polarisation of 45° with respect to its long axis. a) Far field scattering efficiencies showing the presence of both a broad feature similar to Fig. (1.2) at around 200–450 nm and also a sharp resonance at 676 nm. Note the strongly asymmetric Fano-like resonance (sharper than the resonance in the extinction spectrum) in the scattering efficiency at this wavelength. b) The DSCS for equatorial illumination.

Figure (1.4) shows the same particle, now illuminated equatorially with an incident light polarisation of 45° with respect to its long axis, where now modes with $m = 0$ character dominate the response of the system. The broad feature at around 200–450 nm, containing structures similar to the composite modes of Fig. (1.2), is insensitive to the particle length, as shown by examining particles with varying length and the same diameter. No clear hot or cold spots can be observed on the particle surface, see Fig. (1.5a). The sharp resonance at 676 nm shifts with rod length, and its surface field as shown in Fig. (1.5b), has the strong nodal, local structure of a "waveguide" mode on the long axis, remarkably similar to the experimental results of Ref. [91].

Figure (1.6) shows only mode pairs that cannot be excited by axially incident light, primarily the $m = 0$ channels; multi-mode resonances similar to the one discussed for axial incidence originate the broad features at short wavelength;

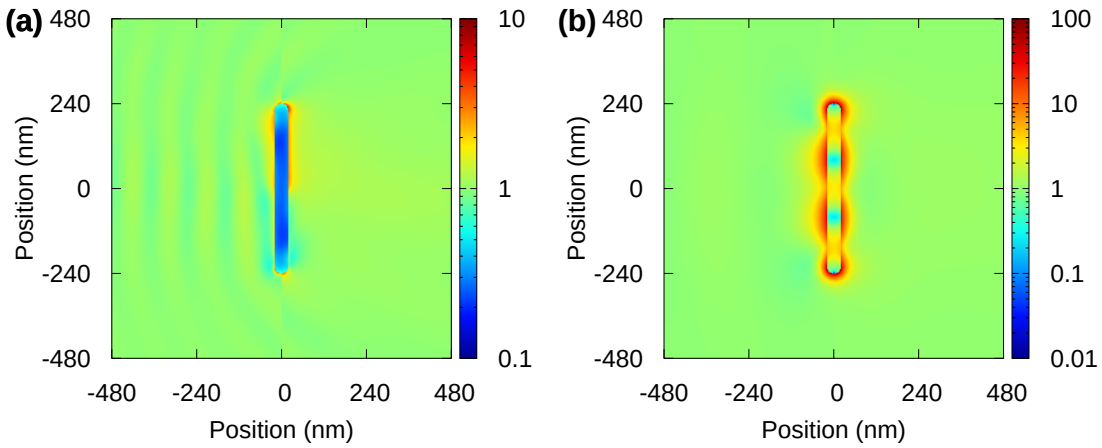

Figure 1.5: Near field intensity for the 480 nm length rod, shown at the a) broad feature (207 nm) and at the b) "waveguide" Mie-like mode at 676 nm of Fig. (1.4a).

most of the corresponding modes are not shown. Figure (1.6) shows that for most principal mode pairs of this particle, excitation occurs only for either the absorbing (internal) or radiating (scattering) member of the pair, and all the three resonances at around 550-700 nm are absorbing. The excitation paths in Fig. (1.6b) and Fig. (1.6e) show that only the best aligned of the three resonant pairs are excited for this particular field. This resonance is undetectable for incident light probating along the axis, but it is observable as the angle of incidence is rotated towards the equator at 90°, Fig. (1.4); at ∼600 nm the more weakly aligned mode pair becomes excited for incident angles of $\sim 50°$. Near the sharp resonance at 676 nm, the resonant mode and a weakly aligned, non-resonant, scattering mode transport the energy into the far field, see Fig. (1.6d). Interference between these two modes gives a Fano-like asymmetric feature in the total scattering cross-section that is sharper and more asymmetric than the single pair resonance. On the contrary, only the resonant mode determines the absorption, producing a symmetric feature in the absorption cross-section, with its maximum coinciding with the largest alignment of the mode pair.

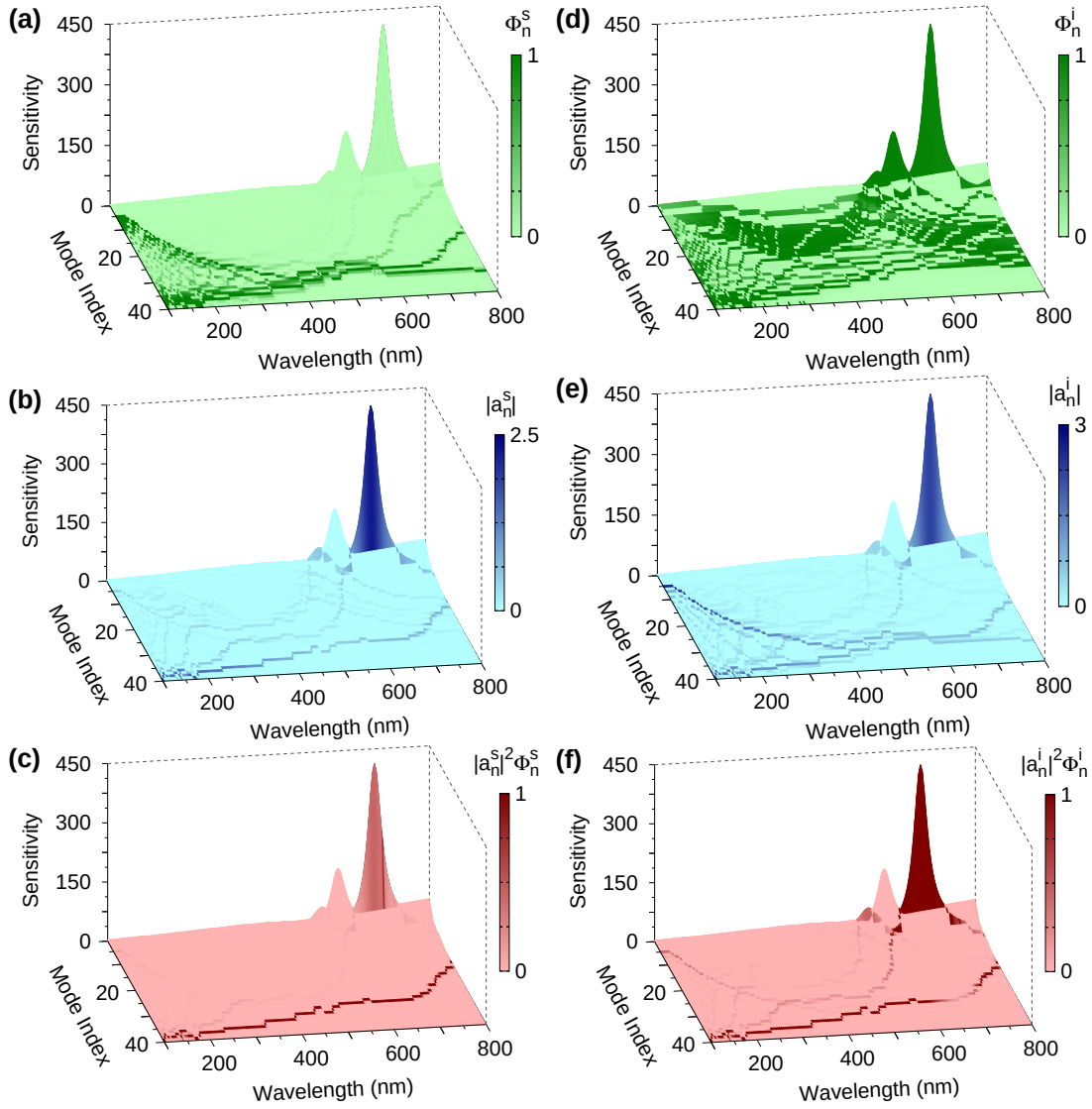

Figure 1.6: Principal angle landscapes for the rounded nano-rod for modes able to couple to illumination from the side of the rod, as in Fig. (1.4). The sharp mode is again a single well aligned principal pair, the best aligned of three (and the only one excited by this particular field). c) Shows that the energy is transported into the far field by the resonant mode and by a weakly aligned, non-resonant, scattering mode. These modes also interfere to give the total scattering cross section and produce the characteristic asymmetric and sharpened Fano-like resonance shown in the scattering efficiencies of Fig. (1.4a).

1.3 Supermodes of multiple particles

We now consider a collection of r particles at arbitrary positions. The full Hilbert space of this aggregate is the direct sum of the Hilbert spaces of each particle; we again have two distinct subspaces of solutions of Maxwell's equations, the

internal solutions and the external solutions. For each particle we can either use sets of electric and magnetic multipoles, as in Sec. 1.1, or the resulting internal and scattering principal modes of the single particles to expand the solutions of the system. The internal fields of each particle are identically null on the surfaces of the other particles in the system, while scattering fields have singularities only inside the originating particle itself but are non-null on all other particles' surfaces. Using the single particle principal modes of each of the particles as a basis, the resulting multi-particle Gram operator has the same structure as the single particle operator, *i.e.*

$$\begin{bmatrix} \mathbb{I} & I^\dagger S \\ S^\dagger I & S^\dagger S \end{bmatrix}, \tag{1.24}$$

so we can define principal modes and resonances as we have done before. The dependence on the particles of Eq. (1.24) is given by

$$I^\dagger S = diag\{C_1, \ldots, C_r\} + \begin{bmatrix} 0 & \ldots & I_1^\dagger S_r \\ \vdots & \ddots & \vdots \\ I_r^\dagger S_1 & \ldots & 0 \end{bmatrix}, \tag{1.25}$$

and

$$S^\dagger S = \mathbb{I} + \begin{bmatrix} \hat{S}_1^\dagger \hat{S}_1 & \ldots & S_1^\dagger S_r \\ \vdots & \ddots & \vdots \\ S_r^\dagger S_1 & \ldots & \hat{S}_r^\dagger \hat{S}_r \end{bmatrix}, \tag{1.26}$$

where the index identifies the particle to which the fields belong, the hat over the matrices mean that the integrals are calculated on the surfaces of the other particles in the system and C_r is a diagonal block with the r^{th} particle's principal cosines on the diagonal. In order to implement the principal mode theory, the first step is to transform the matrix in Eq. (1.26) into an identity matrix. This can be done using the block structure of the matrix, in analogue to the single particle case of Sec. 1.1. This results in a set of supermodes for the composite system, which are again pairwise coupled at the interface between the external medium and the internal space of *all* of the particles.

Analogous to the problem [92, 93] of treating a sub-region of electronic states of a crystal, we can also define an embedding operator, Σ, for the multiple scatter-

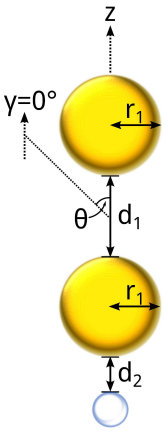

Figure 1.7: Geometry of the three nanoparticle system, for two gold spheres of radius r_1 and separation d_1 with a smaller dielectric particle d_2 away from the second sphere. The incident orientation and polarisation directions (θ and γ) of the exciting light is also shown.

ing effects to all orders from the other particles on the j^{th} particle of the system, leading to a matrix problem in the form of Eq. (1.16),

$$\begin{bmatrix} \mathbb{I} & C - \Sigma\hat{S}_j \\ (C - \Sigma\hat{S}_j)^\dagger & \mathbb{I} \end{bmatrix} \begin{bmatrix} \mathbf{a}^i \\ -\mathbf{a}^s \end{bmatrix} = \begin{bmatrix} \Upsilon^\dagger \left(f^0 - \Sigma\hat{f}^0 \right) \\ \Xi^\dagger \left(f^0 - \Sigma\hat{f}^0 \right) \end{bmatrix}, \tag{1.27}$$

where again the matrix $C - \Sigma\hat{S}_i$ is diagonal, and the incident field at the particle surface is augmented by the light scattered from the other particles in the system. Similarly, an optical analogue of the Dyson equation for the surface Green function of the composite system can be derived, $G_s = G_s^0 + G_s^0 \Sigma' G_s$. Equivalent, using functions to expand the scattered space of the single particle which are themselves exact solutions of Maxwell's equations for an external region which includes all of the other particles in the system, can be applied. Embedding the particle next to a layered material, [94] or a more complex geometry such as a photonic crystal, results in equivalent expressions.

As the distances among the particles increase, the particles become independent from one another. This means that the off diagonal terms in Eq. (1.24) and the terms with the hats in Eq. (1.25) will vanish, so perturbative schemes for resolvent operators, $(\mathbb{I} + A)^{-1}$, could be used to provide approximate solutions. These are based on the binomial expansion and are convergent if the eigenvalues of A are

$$1 \geq \lambda(A)_1 \geqslant \ldots \lambda(A)_n \geqslant -1.$$

Metallic dimers are particularly interesting from the point of view of sensing applications, as a strong enhancement of the electromagnetic field can be

achieved in the gap region between particles. However, a metallic dimer will always be only one of the elements to be considered in a sensing configuration, the other being the molecules to be detected, a point often overlooked. As a matter of fact, any type of sensing in which metallic nano-particles are used will detect a signal that results from the optical interaction, induced by the incident field, between the nano-particle(s) and the molecule, assuming that these are not adsorbed by the particles. For instance, the basic model of an aperture-less SNOM used to study the near field of complex molecules of biological interest near metallic nano-particles, consists of a dimer of metallic spheres with a nearby dielectric particle. The detected SNOM signal is due to the collective response of all the particles interacting through light. In this Section we are interested in studying theoretically how the linear response of the complex system formed by the molecules and the metallic nano-particles emerges from the optical interaction of its constituent parts and depends on their geometrical and material properties. We analyse the simplest configuration relevant for experiments, which consists of a homogeneous medium containing two gold nano-spheres and a smaller dielectric sphere representing a simplified small globular protein. The metallic spheres have a radius of 50 nm; the variations of the fields over spheres of this size, also known as retardation effects, are too large for the quasi-static approximation, but for this case could be taken into account exactly using the electromagnetic modes for the spheres, the Mie modes. For a given incident field and configuration of the spheres, internal and scattered fields can then be found using the Generalised Mie Theory [95], with each configuration of the spheres and each incident field requiring a new calculation.

We study instead how the collective response and resonances of this system of particles depends on the frequency of the incident field and the relative positions of the particles by forming, out of the modes of each particle, internal and scattered modes of the whole system that are coupled pairwise over all the surfaces of the particles using the multi-particle Gram matrix defined in Eq. (1.24).

The geometry of the system is shown in Fig. (1.7). The extinction and scattering cross sections of the metallic dimer as a function of the frequency for

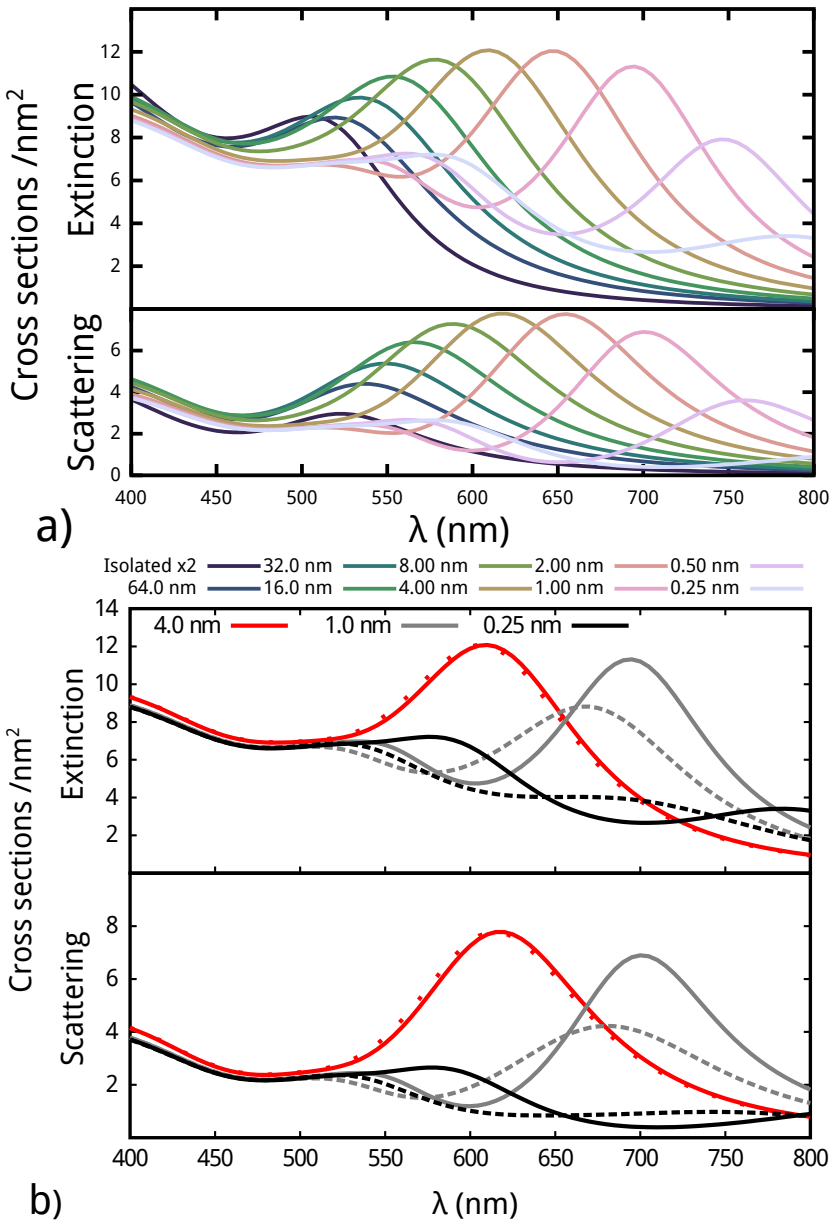

Figure 1.8: 50 nm radius gold sphere dimer in vacuum a) Optical Spectra of metallic particles for a range of d_1 gaps, and the isolated sphere. b) Effect of non-locality (dotted lines) on resonant features in the spectra compared to a local dielectric model (solid lines) for a range of inter-particle gaps, d_1.

various values of the gap and for both local and non-local permittivity is shown in Fig. (1.8) for light with an incident electric field parallel to the dimer axis (the perpendicular case closely resembles the isolated sphere, since modes associated with the inter-particle gap cannot be strongly excited in this case). With the incident electric field parallel to the axis, extinction and scattering cross sec-

tions show a collective dipolar resonance at long wavelengths that moves towards longer wavelengths as the gap increases until it disappears; while the gap has no significant effect for incident electric field perpendicular to the dimer axis. A comparison of the scattering and extinction cross-sections for local and non-local responses is shown in Fig. (1.8b). As already noted by other authors [96, 97], the non-local permittivity affects the behaviour of the dimer most strongly for (very) small gaps when the incident electric field is parallel to the axis. A small (10 nm radius) dielectric sphere, of similar size and dielectric properties ($\epsilon_r = 3.0$) to a globular protein [98], is then added close to the outside of the dimer at a distance of d_2 ∼1–4 nm. The isolated dielectric particle does not exhibit any resonances in the range of 400–800 nm, and its addition does not visibly change the optical cross sections of the resulting three particle system from those of Fig. (1.8b) for either local or non-local response models of the gold particles.

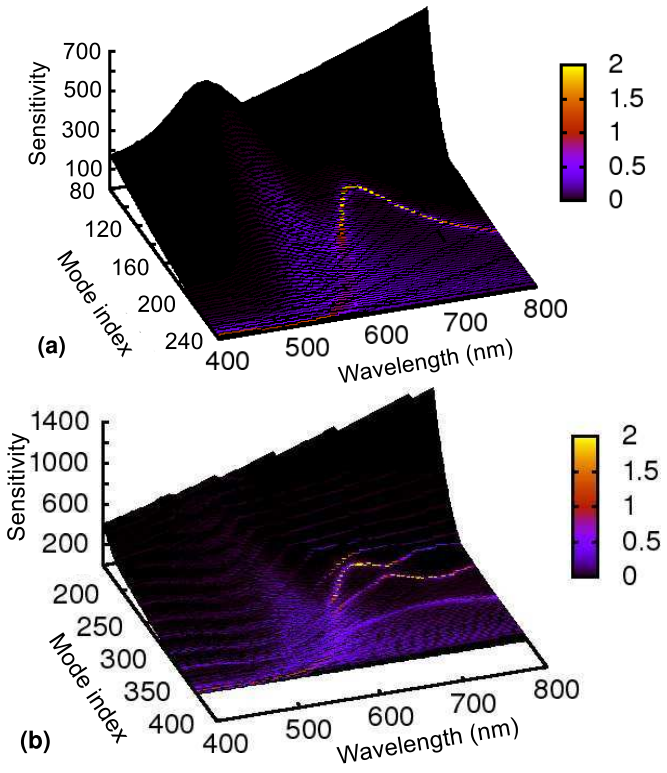

Figure 1.9: a) Principle modes of the metallic dimer. b) Anti-crossing induced by the small neighbouring dielectric particle of Fig. (1.7). The sensitivity of the modes is equivalent to $(\sin \xi)^{-1}$

Figure (1.9a) shows the mode landscape for the principal supermodes of the dimer with the incident field consisting of a linearly polarised plane wave with electric field parallel the axis of symmetry and incident at 90° to the axis. From these two Figures we can see how the presence of the small dielectric particle modifies the structure of the supermodes, even if the extinction cross section of the dielectric particle on its own is much smaller than the extinction cross section of the metallic dimer: the dominant supermode of the metallic dimers is replaced by a combination of three supermodes for the three-particle system, with two of these modes showing an avoided crossing. The supermodes have the same dependence upon particle size as modes of the single particles, showing a red-shifting and broadening of resonances as the dimensions are increased. The supermodes of the three particle system instead depend very weakly on the size of the small dielectric particle as it does not have any resonances within this spectral range.

1.4 Summary

In this Chapter we have reviewed the theory of principal modes that can be derived for any smooth particle starting from a set of distributed electric and magnetic multipoles. We have shown how this theory can be used to identify resonances in nano-particles. The theory can also be extended to collective principal modes, or supermodes, of several nano-particles interacting through light. This has shown that supermodes that efficiently transport energy in the far field can emerge from combinations of principal modes of different particles that do not transport much energy into the far field individually. This is relevant for all types of microscopy that require the interaction of the object investigated with nearby metallic particles or tips, such as, for instance, SNOM and aperture less SNOM, which we shall discuss in the following Chapter.

Chapter 2

Near field imaging

Optical microscopy offers many advantages over other techniques as light is versatile to a range of experimental conditions, non-destructive, relatively cheap and easy to produce, and capable of providing spectral, spatial and temporal information about a sample due to our knowledge of light's interaction with matter.

For traditional optical microscopes, both the input and collection of light are performed in the far field. This configuration imposes a fundamental limit on the spatial resolution which can be attained. This limit, as defined by Abbe [99], is known as the diffraction limit,

$$\Delta x = \frac{\lambda}{2(n \sin \alpha)}, \tag{2.1}$$

where Δx is the spatial resolution, λ is the vacuum wavelength, and $n \sin \alpha$ is equivalent to the numerical aperture NA of the collection lens, with n the refractive index of the propagation medium and α the acceptance angle of the lens. At optical wavelengths, with $\Delta x \approx \lambda/2$, this gives a maximum spatial resolution of around 200 nm. This limit can be understood in terms of Fourier optics [100] by using an angular spectrum representation of light: any wave can be represented as an infinite sum of plane and evanescent waves. In traditional optics, with the detection element many wavelengths from the sample, only plane waves contribute to the signal – ignoring spatial frequencies associated with evanescent waves[1]. When evanescent waves can be included, the bandwidth of spatial fre-

[1]Evanescent waves are non-propagating waves, which decay exponentially away from a

quencies is unlimited and, in principle, there is no limit to the resolution which can be attained.

Near-field optics techniques employ either a localised light source or detector, or both, positioned at a distance $R \ll \lambda$ from a sample, where the limit to the spatial resolution is principally imposed by the geometry of the near-field element(s) which typically have dimensions on the order of tens of nanometres. In this Chapter, we will investigate one of these techniques, termed SNOM (or NSOM) which stands for scanning near-field optical microscopy, or microscope. In Sec. 2.1 we discuss the principles of operation of this technique, and the modelling of the localised excitation field. Then in Sec. 2.2, we apply the theory of principal modes to investigate the near-field transmission images obtained via SNOM, providing a physical description of the complex spatial structure, and evolution with frequency, of the plasmon modes responsible for these images. This research, published in Ref. [101], was conducted as part of an international collaboration with the experimental groups of Prof. Hiromi Okamoto of the Institute for Molecular Science in Okazaki, and Prof. Kohei Imura of Waseda University, Tokyo.

2.1 Scanning near-field optical microscopy

Scanning near-field optical microscopy is the general term applied to a selection of near-field techniques, developed over the last four decades, which can be broadly categorised according to the method of illumination or collection as either *aperture* or *apertureless* (also known as scattering type) SNOM. These techniques combine the excellent spectroscopic and temporal selectivity of classical optical microscopy with a deeply sub-wavelength lateral resolution. The diverse range of applications, to name but a few, includes single-molecule fluorescence imaging [27], Raman spectroscopy [102, 103], investigation of nonlinear processes such as second-harmonic generation and two-photon photoluminescence [24], and the visualisation of confined surface fields [104, 105, 91]. In this Section, we briefly

surface or light source.

review some of the developments in near-field optical microscopy, and discuss the operating principles of aperture SNOM and the modelling of a near field excitation.

2.1.1 Conception and development

In a letter to Einstein (and subsequent paper) in 1928, Synge proposed a novel idea for a near-field microscope using a light source incident on a thin, opaque screen with a sub-wavelength aperture, positioned at a distance from the sample no greater than the aperture diameter [106]. The field through the aperture would provide a localised field, which could be scanned over the sample taking measurements at each point, providing sub-wavelength spatial resolution. The feasibility of this aperture method was first tested in the 1970s by Ash and Nicholls, with $\lambda = 3$ cm microwaves, achieving a resolution of $\lambda/60$ [107]. The invention of the scanning tunnelling microscope (STM) [108] in 1981, earning the 1986 Nobel prize in Physics, introduced nanometre-scale positioning technology. Over a decade after the work of Ash and Nicholls, the first demonstration of this technique in the optical regime was by Pohl and his colleagues, Denk and Duerig, at IBM's lab in Zurich [109]. Instead of a screen with an aperture, they used an etched quartz crystal coated with layers of chromium, aluminium and gold as a probe and fashioned a small opening at the apex of the structure. Scanning over a sample, they reported a resolution of $\lambda/20$ using $\lambda = 488$ nm light. Another technique was independently reported shortly after by Lewis *et al.* at Cornell University, using nano-holes in opaque screens, made via electron beam lithography, for the aperture [110] similar to Synge's original idea. Nanoscopic probes are more practical when scanning over rough surfaces, and became a staple component in the rapid development of this area of research. The first marked improvement in imaging came with the adoption of adiabatically heated and pulled optical fibres as the core for SNOM probes [27], which also improved reproducibility.

The tip must be maintained within nanometres of the sample surface during scanning in order to produce high-resolution optical images. Various mechanisms have been adopted for this purpose, but the most popular is the shear-force

feedback technique, which was introduced independently by two groups in the 1990s [111, 112], similar to non-contact atomic force microscopy (AFM). In the shear-force method, the tip is dithered laterally at one of its mechanical resonances. To avoid diminishing the resolution of the optical images, the amplitude of this vibration is typically kept < 10 nm. The shear-forces between the tip and sample, as the the tip approaches the sample surface (at a distance ≤ 20 nm), dampen the vibration and the amplitude and phase modulation can be monitored to control the gap between the two via a feedback signal.

The resolution limit of aperture SNOM is proportional to the aperture diameter, the dimensions of which are limited by the light throughput (this is discussed in Sec. 2.1.2), and is around $30-50$ nm [113]. In order to improve upon this limit, and to take optical microscopy closer to the nanometre scale, a new technique was proposed using a sharp metallic probe illuminated from the far-field [114]. In this apertureless configuration, the "lightning rod" effect causes field lines to concentrate at the tip of the probe, creating a localised field source. The resolution for this technique is related to the radius of curvature of the sharp end of the probe, and can reach ≤ 5 nm. This technique suffers from poor contrast due to the strong background signal of the illumination source. However, parasitic effects, which can limit the achievable resolution by saturating the detected signal, such as interference due to bulk scattering and spurious signals arising from the sample-probe coupling, can be minimized using cross-polarization schemes [105].

In order to combine the best features of both types of SNOM, namely the resolution of apertureless and the contrast of apertured, a method of growing a nano-antenna at the apex of a SNOM probe has been proposed [115]. We consider a similar geometry in Sec. 4.2.2, without an external light source, to enhance the fluorescence signal of a dipolar emitter. Other developments include the photon scanning tunnelling microscope (PSTM) [116] and scanning tunnelling optical microscope (STOM) [117], where the evanescent field due to the frustrated total internal reflection (FTIR) of a light beam in a prism couples to a probe held above a transparent sample. These methods are analogous to STM, where a tip is scanned over a conducting sample and a bias voltage applied. The tun-

nelling current depends exponentially on height, as do the evanescent excitations in PTSM/STOM, and an image is formed by keeping the current constant.

A full review of the many developments and uses for SNOM is beyond the scope of this thesis, and has been extensively reported elsewhere over the last three decades. For the interested reader, comprehensive reviews are available on: the history and development of SNOM [25, 26], developments in probe technology [118], image formation and near-field optics theory [119, 120], and recent applications to surface reactions [121]. In addition, the textbooks of Kawata [4] and Novotny and Hecht [122] provide a wealth of information on these subjects. We shall focus in the following on the method relevant to the research presented in the final Section of this Chapter: aperture SNOM.

2.1.2 Aperture SNOM

A typical modern aperture SNOM tip consists of a mono-mode fibre which is either pulled, or chemically etched, to a fine point at one end, that is then coated using an opaque metal leaving a narrow aperture at the apex. The metal coating is usually either aluminium or gold, with a thickness $\approx 50 - 100$ nm to confine the light, and to prevent leakage from the fibre near the tapered end. In general, throughput for a given aperture size increases as the taper angle of the tip steepens. Fibres shaped by etching provide sharper, more consistent taper angles and hence allow for greater throughput of light at the aperture. However, the probe surface is much smoother for pulled fibres, meaning that less metal coating is required. For both techniques, etching and pulling, the aperture is formed during the evaporation, used for aluminium, or sputtering, used for gold, of the metal coating.

The spatial resolution of the resulting optical images obtained for this type of probe is approximately given by the size of the aperture. However, the diameter of the aperture itself is limited by the skin-depth of the metal coating [122]. Because the aperture diameter is usually smaller than the cut-off radius of the modes propagating in the probe, all modes run into cut-off, and only an extremely small fraction of the light input power is emitted by the aperture. The aperture

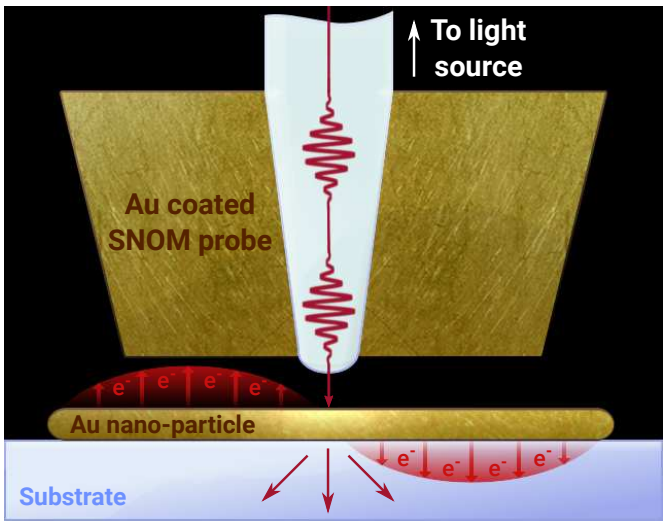

Figure 2.1: Illustration showing the probe of an aperture SNOM probe operating in illumination mode, irradiating a metallic sample, prepared on a dielectric substrate. The localised field excites plasmon modes of the particle, which can convert evanescent waves into scattered light and in some cases enhance the field transmitted in the direction of the detector.

diameter and the taper angle cannot be reduced arbitrarily because a minimum light throughput must be ensured. As a consequence, low transmission becomes the main limiting factor for the improvement of resolution in aperture SNOM.

The main configuration modes for operation of an aperture SNOM are,

- Illumination mode, where the near-field probe is used to illuminate the sample and detection is done in the far field, for the transmitted or reflected fields depending on the opacity of the sample.
- Collection mode, where the sample is illuminated from the far field and the near-field response is collected by the probe, coupling evanescent modes of the sample into propagating waveguide modes.
- Illumination/collection mode, where the probe is used to both illuminate the sample and collect the signal.

In the most commonly used mode, illumination, the detector and probe share an optical axis. The light emitted from the aperture illuminates the sample of interest in close proximity. So that the optical path does not change during

imaging, the sample is typically raster-scanned using a mechanical XYZ piezo-stage, and at each position the corresponding transmitted far-field radiation is recorded.

In illumination mode, the capacity for super-resolution arises from the coupling of evanescent waves from the probe, emanating from the aperture, to the sample. The closer the probe can be positioned to the sample, the stronger the coupling and the greater is the confinement of the excitation. The sample has sub-wavelength features which scatter this light into the far field detector, carrying with it information of these features. In collection mode, the far-field illumination excites evanescent scattering waves at the sample surface. If the probe is suitably close, these waves couple to the optical fibre through scattering processes, converting the evanescent scattering fields into evanescent and propagating waveguide modes of the fibre. These waveguide modes then propagate through the fibre, carrying information of the sample near-field. The reciprocity theorem in electromagnetism illustrates that the illumination and collection modes can be considered identical. For a particular collection mode configuration, there is an equivalent illumination mode configuration that will produce identical images. This reciprocity relation has been tested experimentally [123].

In addition to these configuration modes, the SNOM apparatus can be operated in three different signal modes. These are: constant height mode, constant intensity mode, and constant gap mode. In constant height mode, the tip or sample is moved only in the lateral plane. In constant intensity mode, the optical signal is kept constant using a feedback system, forcing the tip/sample to move vertically as it is scanned laterally. This path of the tip/sample does not generally reflect the topography of the sample. In this mode, the motion of the tip is recorded to produce the image. This mode is used extensively in PTSM/STOM, in analogy with STM. Constant height and constant intensity can be considered equivalent assuming that the maximum height of the sample surface is much smaller than the excitation wavelength. Finally, in constant gap mode, the tip is forced to follow a path by an auxiliary control mechanism, and moves vertically to follow the topography of the sample. This mode can lead to artefacts due to

the vertical motion of the tip. This can be reduced by using a pseudo-constant height mode, where a small protrusion outside the aperture makes the tip keep a constant height above the substrate instead, and leads to the artefact appearing spatially shifted, reducing interference with the transmission images [123].

2.1.3 Modelling the field from an aperture tip

The localised field from an aperture tip is generated from the coupling of a light source into an optical fibre, which is converted into cylindrical waveguide modes of the fibre core. In most cases, the diameter of the aperture is smaller than the cut-off radius of the propagating modes and so at the tapered end of the probe, as the fibre diameter decreases, all modes eventually run into cut-off. For linearly polarized light, the fundamental mode, which propagates furthest, is the analytically known HE_{11} mode [124]. This mode also runs into cut-off near the apex (for diameters less than ≈ 160 nm), and exponentially decays towards the aperture plane giving the localised tip field [122]. In order to describe the excitation field for SNOM, we need to model the near-field distribution in the region of the aperture.

In 1944, Bethe famously derived an analytical model [125] for the diffraction of plane waves through a small circular aperture in an infinitely thin screen made of a perfectly conducting metal; showing that Kirchhoff's scalar theory [126] failed to solve the boundary conditions for apertures much smaller than the wavelength of incident light[2]. To represent the diffracted field, Bethe employed fictitious charges and currents at the aperture to solve the boundary conditions: a magnetic dipole was aligned anti-parallel with the magnetic component field incident on the aperture, and an electric dipole was aligned normal to the the aperture plane. The electric dipole contribution would hence only be excited by an obliquely incident wave.

A discontinuity of the electric field at the aperture in this model, contrasting the requirements of the boundary conditions, was discovered by Bouwkamp [128], although the far field representation proved to be correct [129]. Bouwkamp in-

[2]A vectorial form of Kirchhoff's theory, derived by Smythe [127], has similar limitations.

stead used the electromagnetic version of Babinet's principle [130][3] to translate the diffracted fields of a small two-dimensional disc, irradiated by a plane wave, to an equivalent aperture. By correcting the sign of the electric dipole moment in Bethe's model, the Bethe-Bouwkamp solution for an idealised aperture can be expressed, in terms of the effective electric and magnetic dipole moments respectively, as [131],

$$\boldsymbol{p} = -\frac{4a_r^3}{3}\left(\boldsymbol{E}_0 \cdot \hat{\boldsymbol{n}}\right)\hat{\boldsymbol{n}}, \tag{2.2}$$

$$\boldsymbol{m} = -\frac{8a_r^3}{3}\hat{\boldsymbol{n}} \times \left(\boldsymbol{H}_0 \times \hat{\boldsymbol{n}}\right), \tag{2.3}$$

where $\hat{\boldsymbol{n}}$ is the unit vector normal to the aperture plane in the direction of propagation, a_r is the aperture radius, and $\boldsymbol{E}_0$, $\boldsymbol{H}_0$ are the components of the incident field. The induced dipole moments are now *both* anti-parallel to the components of the field at the aperture. This model is attractive as it gives closed analytical expressions for the diffracted fields and, although it fails to accurately describe any real aperture, it gives the character of the fields from sub-wavelength apertures.

Such idealised apertures are unfortunately a poor model for a SNOM tip due to the very different geometries, and the fact that the incident field is due to waveguide modes, not plane waves, which interact with the metal cladding. Inspired by the Bethe-Bouwkamp model, Obermüller and Karrai used pairs of dipoles to fit the measured angular intensity distributions from SNOM tips and found that a pair of in-plane dipoles gave the best result [132]. A similar model was derived using a multipole expansion for a conical tip made of a real (finite) metal [133], accounting for the effects of the geometry of the tip: the aperture radius and half-angle β, from the symmetry axis, which defines the slope of the generatrix for the (truncated) cone. The effective dipole moments derived in relation to the local field at the centre of the aperture plane, $\boldsymbol{E}(0)$, $\boldsymbol{H}(0)$, were

[3]Babinet's principle states that sum of a wave transmitted through an apertured screen and the wave transmitted through a complementary screen, is equivalent to the wave with no screen present.

found to be,

$$\boldsymbol{p} = \frac{1}{4\sqrt{2}} \frac{a_r^3}{\sin \beta^3} \boldsymbol{E}(0), \tag{2.4}$$

$$\boldsymbol{m} = \frac{2}{4\sqrt{2}} \frac{a_r^3}{\sin \beta^3} \boldsymbol{H}(0). \tag{2.5}$$

The local field at the aperture can be determined numerically [134], however, a simple analytical model was later presented giving the field from the tip as the combination of the pair of dipoles for an electrostatic field, with moments related as[135],

$$\boldsymbol{m} = 2\hat{\boldsymbol{n}} \times \boldsymbol{p}, \tag{2.6}$$

which gave quantitative agreement with experimental observations. This model should effectively describe the field in both the near and far-field regions. We note that the expressions given in Eq. (2.6) were characterized by using fluorescent nanospheres, with dimensions much smaller than the aperture, and thus intrinsically contain information of the response of these scatterers, but it is assumed that this contribution is minimal and can be safely disregarded in most applications. For linearly polarized light coupled through the optical fibre[4], the electric dipole is aligned with the component of the electric field.

2.2 Imaging the plasmon modes of gold nanodiscs

It has been well established that optical properties of single nanoparticles, whose spatial scales are sufficiently smaller than that of the wavelength of the interacting light, are well explained by the dipolar approximation. The dependence of the optical properties on the size and shape of the nanoparticles can be also explained by introducing the depolarization factor [19]. In larger nanoparticles, on the other hand, the contribution of multipolar plasmon resonances becomes significant because of non-negligible retardation effects. In this situation, consideration of higher order plasmon modes is indispensable to correctly understand

[4]Assuming that polarization is conserved in the fibre.

the optical and spectroscopic properties of the nanoparticles. Moreover, an understanding of the spatial features of plasmons based on fundamental modes of the system is useful to provide clear physical pictures of the phenomena.

Gold nanorods are an example of the importance of multipolar modes and retardation effects. In these almost one-dimensional particles, transverse and longitudinal plasmon modes can be excited optically which are polarized across and along the nanorod, respectively [136]. The transverse mode appears in a frequency region similar to that of the plasmon resonance of a small spherical nanoparticle, near the bulk material resonance. The resonance frequencies of longitudinal plasmon modes instead appear over a wide frequency range, where modes with fewer nodes in its standing wave have a lower resonance frequency. The dipolar mode thus has the lowest resonance frequency, and all the resonances at higher frequencies are attributed to the excitation of multipolar modes. Multipolar modes are not excited efficiently by conventional far-field irradiation when the particle size is small enough compared to the wavelength of the light, but they become significant when the particle size is large and retardation effects are non-negligible. The spatial structures of these longitudinal modes have been visualized by near-field optical microscopy [136] or recently by electron-microscope based techniques [32, 33, 34].

In two-dimensional systems such as a circular gold nanoplate (nanodisc), the spatial structures of the plasmon modes are much more complicated. In addition, as the volume damping effect [137] becomes significant for these systems compared with nanorods, the spectral widths of individual modes are broad and consequently spectral overlaps between plasmon resonances are observed [138, 139]. As a result, the optical properties of plasmons in nanodiscs are not as well understood as those of nanorods. To fully utilize the unique properties of plasmonic materials in practical applications, detailed knowledge of the plasmon modes is essential. In this Section, we use principal modes to describe the formation, and evolution with frequency, of the complex mode structures experimentally visualized by scanning near-field optical microscopy (SNOM).

2.2.1 Experimental method

Arrays of gold nanodiscs (diameter $400 - 800$ nm, thickness 35 nm) were fabricated on a cover-slip by the electron-beam lithography/lift-off technique [140]. A home-made apertured scanning near- field optical microscope was operated under the ambient condition [29], using aperture near-field fibre probes fabricated by chemical etching[5]. The diameter of the aperture was determined to be $50 - 100$ nm by using scanning electron micrographs (SEM) and/or fluorescence images of single molecules. The sample substrate was mounted on a piezo-driven-stage for lateral scanning and the distance between the near- field aperture tip and the sample surface was regulated at $10 - 20$ nm by a shear-force feedback mechanism. For near-field transmission measurements, either a Ti:sapphire laser or a Xe discharge lamp was used as a light source. The incident polarization was controlled by a combination of a half and a quarter wave plates. A gold nanodisc was locally illuminated through the aperture of the near-field probe, and the transmitted light through the sample was collected by an objective lens and detected by a polychromator equipped with a charge- coupled device (CCD). At each point in a whole scan area the intensity spectrum was measured, and near-field extinction spectra were calculated as $-(I - I_0)/I_0$, where I denotes the far field transmitted intensity taken with the sample present and I_0 the intensity from the bare substrate. Near-field transmission images were obtained by mapping the transmission $T = I/I_0$ at a given spectral range. The polarization of the transmitted light was characterized by a polarizer installed in front of the detector.

2.2.2 Near-field transmission images

The dimensions of the fabricated gold nanodiscs were determined by SEM and topography measurements, the SEM image is shown in Fig. (2.2a). Plasmon resonances of the discs depend on the aspect ratio (diameter / height) and shape of the particle, and the dipolar resonance for the disc with 400 nm diameter is

[5]Produced by JASCO Corp.

expected to occur at wavelengths longer than 1000 nm [141]. The far field extinction spectrum for this disc is shown in Fig. (2.2b). The dipolar resonance of the disc is far beyond the observed spectral range, and a shoulder and a broad band were observed at around 620 nm and near the infrared spectral region, respectively. These features are assigned to higher order plasmon resonances with the aid of theoretical calculations, as discussed in Sec. 2.2.3. Figure (2.2c) shows a polarized near-field extinction spectrum taken near the edge of the disc. The spectrum exhibits multiple peaks in the visible to near-infrared region similar to the far field spectrum. A sharp negative extinction peak at ~ 650 nm is typical of the near-field extinction measurements, and is attributed to the conversion of near-field radiation to propagating light [141, 142]. The positive peaks at ~ 580 and ~ 780 nm are close to the shoulder and the band observed in the far field spectrum, Fig. (2.2b), and are attributed to plasmon resonances. The near-field transmission spectrum was found to depend on the position of the probe with respect to the disc. For example, the negative peak is more pronounced at the centre of the disc with respect to that observed at the edge. The position dependence of the near-field transmission spectrum implies that the spatial distribution of the oscillation amplitude of the mode excited at longer wavelength is not uniform over the disc surface. Since the spatial characteristics of the mode are not directly apparent in the spectrum, which is a frequency-resolved data set, mode assignments of the plasmon resonances are not straightforward using only information from the spectrum. Near-field imaging enables spatial visualization of the mode and facilitates assignment of the mode by combining the data with theoretical simulations.

polarized near-field transmission images of the gold nanodiscs observed at 780 nm are shown in Figs. (2.3a-b). The dashed circle indicates the approximate shape of the disc and the arrow shows the incident polarization direction. In the image, dark areas represent higher extinction (*i.e.* a larger reduction of transmitted light due to scattering and absorption of incident light). Dark lobes are roughly aligned perpendicularly to the polarization direction. The transmission image rotates 90 degrees as the polarization direction is rotated by the same

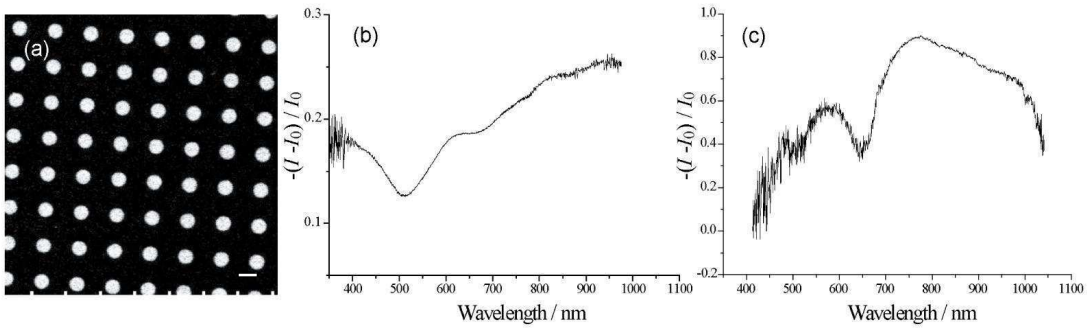

Figure 2.2: (a) A SEM image of gold nanodiscs (diameter 400 nm × height 35 nm). Scale bar: 500 nm. (b) Far field transmission spectrum of the disc. (c) Near-field transmission spectrum taken at the edge of the disc.

angle.

Profs. Imura and Okamoto have previously reported, on the near-field excitation of a gold nanorod, that the extinction intensity of the longitudinal plasmon mode showed a $\cos^2\theta$ dependence upon the incident polarization direction, where θ is the angle between the long axis of the rod and the polarization direction [24]. This indicates that the excitation near-field is almost linearly polarized, and that there is no significant transfer of energy between orthogonal polarizations due to the interaction of the rod with the probe. The polarized optical near-field at an apertured probe tip utilized to visualize orientations of single-molecule transition moments with fluorescence excitation imaging [143] also indicates approximately linear polarization near the tip.

In addition to the polarized near-field transmission measurements described above, near-field transmission measurements with unpolarized illumination and polarized light detection were performed, which found that the near-field images show essentially the same spatial features and polarization dependences observed in Figs. (2.3a-b). These observations support the hypothesis that the near-field images exhibit distributions of the polarized plasmon amplitudes excited by the incident light. An unpolarized near-field transmission image displays a doughnut-like spatial pattern as shown in Figs. (2.3c-d). Spatial features of the near-field transmission image strongly depend on the observed wavelength. The transmission image observed at 520 nm in Fig. 2.3(e) shows a monotonous spatial feature,

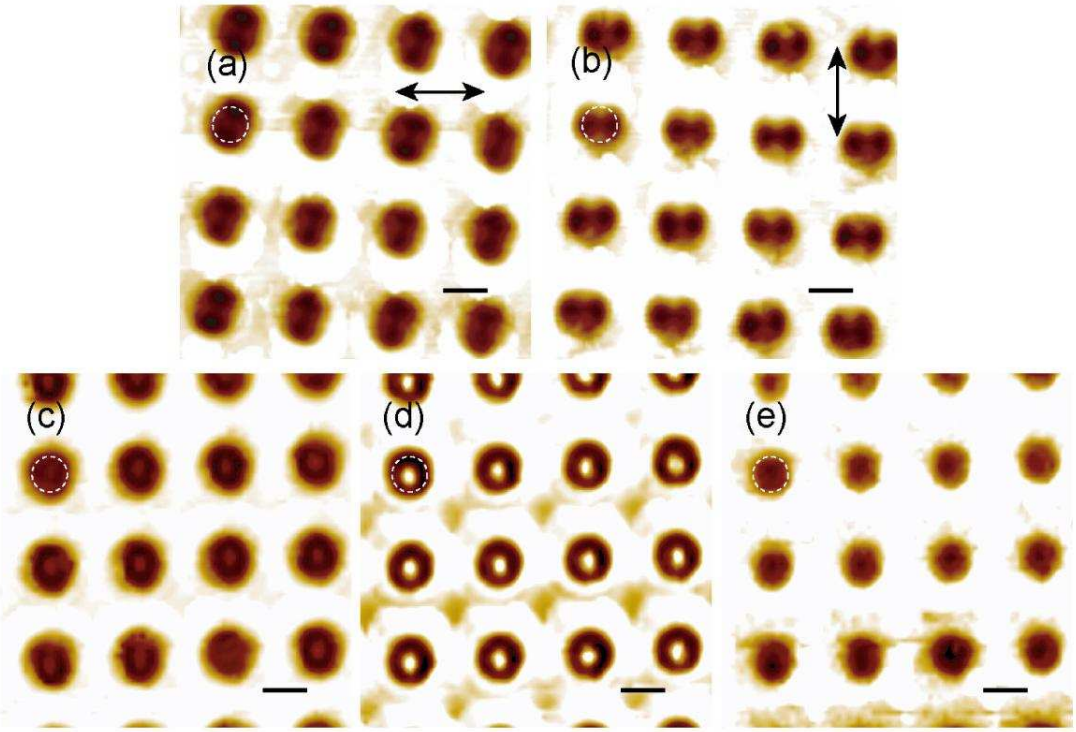

Figure 2.3: (a,b) Polarized near-field transmission images of gold nanodiscs (diameter 400 nm $\times$ height 35 nm) observed at 780 nm. Arrows indicate the direction of the incident polarization. (c-e) Unpolarized near-field transmission images for the gold nanodiscs. Observed wavelength: $\sim$ 780 nm for (c), $\sim$ 640 nm for (d), and $\sim$ 520 nm for (e). Dashed circles indicate the approximate shape of the disc. Image size: 4 μm $\times$ 4 μm. Scale bar: 500 nm.

which is nearly identical to the topographic image (giving the geometrical shape) of the disc. The doughnut-like spatial feature with unpolarized light appears at wavelengths longer than $\sim$ 580 nm. For discs with diameters less than 150 nm, the doughnut-like spatial feature was not observed at 800 nm. These observations show qualitative agreement with the electron energy loss spectroscopy (EELS) maps visualized by a high-resolution transmission electron microscope [144], while the polarization-dependent information is available only with the near-field measurements.

As mentioned, the spatial features of the images depend strongly on the size of the disc. In Figs (2.4a-b), we show near-field transmission images of a larger gold disc (diameter 800 nm, thickness 35 nm) observed at 710 and 790 nm, respectively. The polarization direction of the detected light was vertically aligned in the images. From these images, we observe fine spatial structures of excitation probability, which vary depending on the wavelength of observation. For instance, the image observed at 710 nm exhibits a double-doughnut-like feature, whereas the image at 790 nm shows an extinction spot at the centre combined with a single doughnut feature. For the 400 nm diameter disc, the doughnut-like feature was observed only with unpolarized light detection, while for the 800 nm disc, the doughnut-like feature was observed with the polarized detection. Line profiles, along the dotted lines through the centres of the discs in Figs. (2.4a-b), are shown in Fig. (2.4c) and Fig. (2.4d), respectively. The transmission intensities oscillate along these lines and the period of the oscillation depends on the observed wavelength: the period increases with wavelength.

This finding qualitatively agrees with observations on the spatial properties of the longitudinal plasmon modes of gold nanorods. In gold nanorods, the wave number of the longitudinal plasmon mode gets larger when its frequency increases, following the dispersion relation of the plasmon. Since the spatial features observed in the near-field image of the disc are two-dimensional, it is not straightforward to interpret these features based on the dispersion relation, in contrast with the (quasi-)one-dimensional case. However, for the disc there is also a qualitative tendency for the spatial frequency of the image to increase with

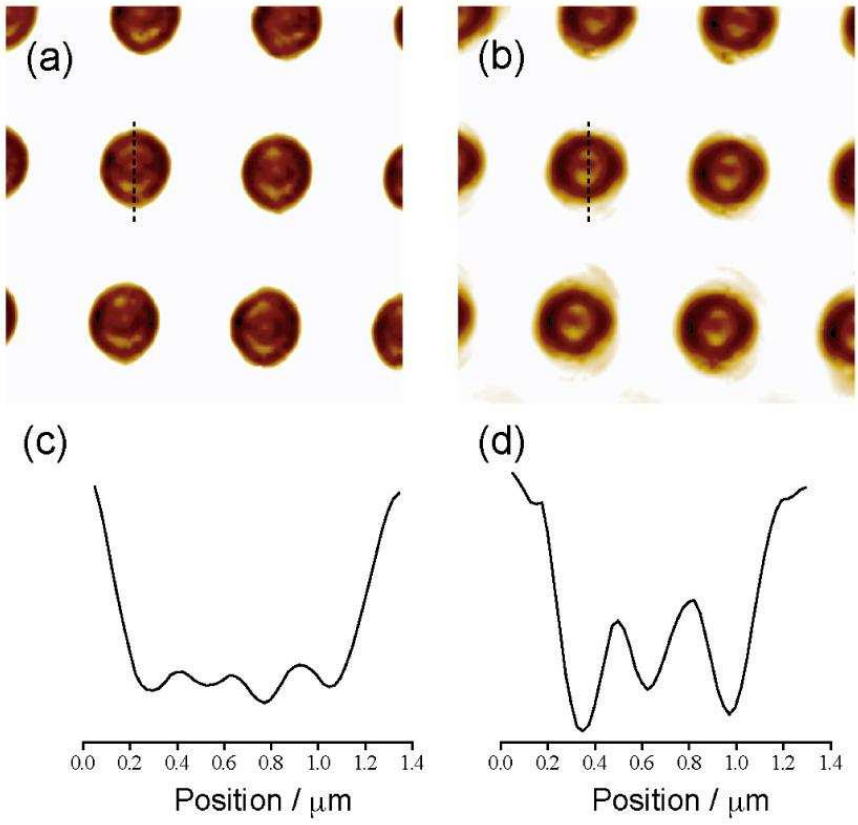

Figure 2.4: (a,b) Near-field transmission images of gold nanodiscs (diameter 800 nm × height 35 nm). Observed wavelength: 710 nm for (a), 790 nm for (b). (c,d) Line profiles taken along the dotted lines in (a,b), respectively.

the frequency of the light detected, suggesting that the two-dimensional waves of the disc plasmons follow a kind of dispersion relation between temporal and spatial frequencies.

As we mentioned above, the near-field imaging provides valuable information on spatial features of plasmons, and is useful for assignments of the spectroscopic features of the metal nanoparticles to fundamental plasmonic modes. On the other hand, the spatial features of two- dimensional systems, such as the discs, are much more complex than those of one- dimensional rods, because of the higher degree of spatial freedom. The mode assignments for the discs are thus much more difficult than for rods. Consequently, to assign the plasmon resonances in the two-dimensional systems, a combination of imaging experiments and theoretical approaches is useful and in some cases essential.

2.2.3 Principal mode analysis

The plasmon modes of these types of particles cannot be treated with any analytical approach. With numerical electromagnetic simulation approaches, for example, such as the finite difference time domain (FDTD) method [145] and the discrete dipole approximation (DDA) methods [146], the concept of modes cannot be introduced, although they can treat nanostructures of arbitrary shapes. The theory of principal modes is the ideal framework to provide assignments of the observed images via a modal decomposition of the optical response, and the unique capacity to describe resonances for arbitrarily shaped (smooth) particles [23, 67, 80, 147, 76]. This approach enables us to give clear physical pictures of the spatial features of plasmon modes of metal nanoparticles observed in the experiments, as we shall see in the following.

We apply the theory of principal modes as described in Chap. 1, where we use distributed regular and radiating multipole sources [148] to build orthonormal sets of internal and scattering modes on the surface of the particles, respectively. As we have discussed, these modes are spatially correlated pairwise on the surface allowing us to define "principal angles" and principal sine functions, $\sin\xi$, in order to identify both geometrical and material resonances of the particles [23].

We are able to qualitatively reproduce the spatial structures of experimental near-field transmission images and by analysing these resonances, we can identify the physical mechanisms that determine the way in which these patterns evolve with the frequency of incident light and, correspondingly, the information that the experimental images provide.

By applying this theory and using an approximate model of the experimental conditions, we reproduce all three kinds of images observed with polarized light (Fig. (2.3) and Fig. (2.4)), as shown in Fig. (2.5), and explain the spatial structures and their transformation as the wavelength changes in terms of a relatively low number of optical modes. This approach allows us to analyse the spatial feature of the collective oscillation of conduction electrons that yields the near-field transmission image observed.

Briefly, the four fundamental components of the physical experiment that are included in the model are the SNOM aperture tip, the nanoparticle, the detector and the scattering medium (substrate). As in the experiments we consider the following two configurations. When the field sent through the SNOM tip is linearly polarized, the total intensity of the light is detected in the far field. When the field is unpolarized, the detector in the far field has a polarizer in front of it and collects only linearly polarized light. In the first case, the field radiated by the SNOM tip is represented by a coherent combination of electric and magnetic radiating point dipoles, both located at the centre of the planar aperture of the probe [135]. In the second case, the radiated field is represented by the incoherent superposition of two sets of these dipoles, oriented at right angles to each other in the aperture plane. As we are only able to model the experimental conditions qualitatively we simply set $|\boldsymbol{p}| = 1$ and, from Eq. (2.6), $|\boldsymbol{m}| = 2$.

We use a dispersion relation for the gold material that includes both the bulk contribution and the effect of surface collisions [149], see Sec. 3.2.3. The inclusion of collisions allows us to match accurately the pattern obtained at the experimental height of the tip above the surface of the particle ($\approx 10 - 20$ nm). Without the additional damping term that arises from the surface collisions, it is difficult to maintain the residual surface error, Eq. (1.21), below 10^{-2} at these

distances without greatly increasing the number of surface points required in the calculations.

Experiments have shown that the spatial structure of the observed near-field transmission image patterns are only weakly dependent on the environment, although this may shift the range of wavelengths at which any given pattern is observed. For this reason, and for simplicity, we assume that the gold nanodiscs are immersed in the material of which the substrate is made, in this case borosilicate crown glass (BK7) [150]. However, the experiments could be more accurately modelled by considering the particle in a stratified medium [151], a similar method is discussed in Sec. C.2.

We calculate the intensity in the far field using the asymptotic forms of the radiating functions [78], evaluated in the limit where the distance to the detection point $r \to \infty$, and integrate the time averaged Poynting vectors associated to the incident and scattered fields, and the interaction between the two, over the detection angles. In Fig. (2.5a) we show the match for the transmission image, at the experimental resonance wavelength, for the small disc of diameter 400 nm. An enlargement of the corresponding experimental image is shown in Fig. (2.5e) for comparison. Similarly, in Fig. (2.5b) we show the calculated image for the larger particle of diameter 800 nm at wavelength *ca.* 710 nm, and the corresponding experimental image in Fig. (2.5f). We observe the longer wavelength near-field transmission pattern for the larger particle at a wavelength blue-shifted with respect to the experiment by *ca.* 25 nm, Fig. (2.5c) corresponding to Fig. (2.5f). We simulate a detector with an effective numerical aperture of 0.85 (corresponding to a 60° cone in the far field). We have also simulated data for a variety of collection angles between 40 and 80 degrees. No significant change is found in the spatial structure of the resulting images, although the contrast between the bright and dark regions reduces slightly as the angle increases.

The near-field transmission patterns can be understood in terms of groups of radiating modes which, due to the cylindrical symmetry of the discs, have an angular phase dependence $\exp(im\phi)$, where ϕ is the azimuthal angle around the disc and m is the index of the component of the optical angular momentum along

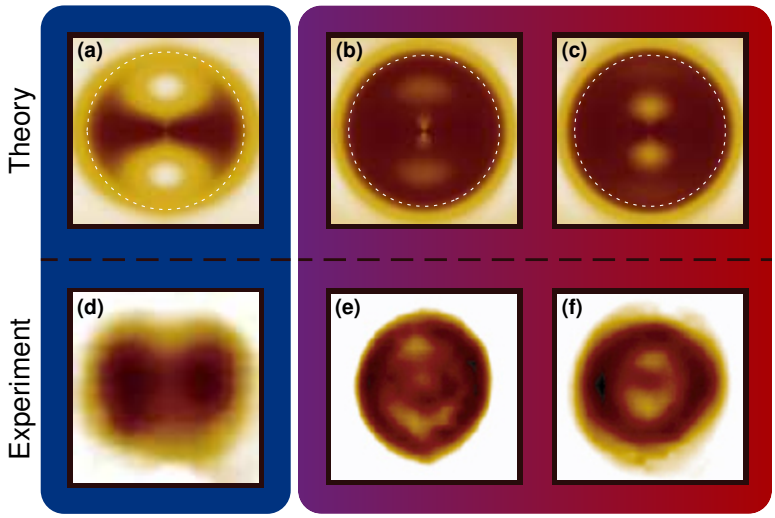

Figure 2.5: Top row: Theoretical near-field transmission images. Bottom row: Corresponding experimental near-field transmission images. the colour scale corresponds to the signal collected by the detector in the far field, I, normalized by the intensity of the incident field, I_0. (a) The near-field transmission image for the 400 nm diameter disc at an incident wavelength of 780 nm, corresponding to (e), which is an enlargement of Fig. (2.3b), calculated using an incident field linearly polarized along the vertical direction of the Figure, and unpolarized light collected at the detector. The corresponding images for the 800 nm diameter disc at (b) 705 nm and (c) 765 nm where the incident field is unpolarized and instead the signal collected by the detector is linearly polarized along the vertical direction of the Figures. (e-f) Enlargements of the measurements shown in Figs. (2.4a,b) for the 800 nm disc, respectively.

the symmetry axis. Therefore, we can group the modes according to their m index into separate scattering channels. Although there are an infinite number of possible optical angular momentum channels which may contribute to the surface field, only the channels with $m = 0, \pm 1, \pm 2$, and ± 3 contribute significantly to the observed transmission patterns, with the higher index channels having significantly less ability to transport energy into the far field. This is because the higher index m channels oscillate more rapidly around the disc and, due to the limited radial dimensions of these particles, the variations become much shorter than the wavelength of the incident light in the scattering medium, making it difficult for these channels to transport energy effectively. We in fact find that the $m = 0$ and ± 1 channels scatter the majority of the light for both discs and provide the basis of the near-field image patterns, with the higher index channels only adding fine structure. Within each channel, the incident field may excite many modes to an appreciable amplitude, which then combine to give the surface field. However, only a selection of these modes are capable of carrying energy [23], or information, into the far field and these are the modes that have the largest effect on the near-field transmission images. For the discs considered here, the light scattered by each channel can therefore be attributed to, at most, a handful of modes.

For the figures, the direction of polarization is chosen to be along the vertical direction of the page. The images are normalized by the intensity of the incident field, I/I_0 , where I is the intensity with the particle present and I_0 the intensity at the bare substrate[6] without the particle. Near-field transmission images show the amount of light received at the detector due to the response of the particle to the near-field source. The effects of the particle on the amount of light transmitted towards the detector fall into 4 categories. Firstly, the disc can scatter light preferentially towards the detector, increasing the amount of light received. Alternatively, light may be scattered away from the detector, reducing the light received. The disc can also absorb light (again reducing the signal). Finally, for reasonably coherent sources of light, interference between the incident light and

[6]In our case, in the homogeneous medium comprised of BK7.

the light scattered by the disc may either increase or reduce the intensity in the far-field detecting aperture.

For the smaller particle (diameter 400 nm), the only significant contributions are from the $m = 0$ and ± 1 channels to the far field pattern, of which the $m = 0$ channel dominates the scattered light. To understand the properties of a scattering mode we consider the spatial correlation between this mode and the internal modes on the surface of the particle. Each principal scattering mode is spatially correlated with at most one principal internal mode, and this correlation is expressed as $\cos\xi$, which is the overlap integral of the tangent components of the pair of internal and scattering principal modes. The mode "sensitivity", $\left(\sin^2\xi\right)^{-1}$, represents the efficiency of this pair of modes to couple to an incident field with tangent components on the particle surface that are spatially correlated to the tangent components of the modes (even at resonance, when the efficiency is maximal, the mode pairs do not couple to incident fields with tangent components uncorrelated to those of the modes).

Figure (2.6a) shows the increase in efficiency of the dominant $m = 0$ mode as it approaches its resonance at $\sim$ 725 nm. This broadness of this feature is the reason why the observed near-field transmission image does not change for the small disc, for these wavelengths. Figure (2.6d) shows the amount of energy scattered towards the detector for two positions of the fibre tip marked in Fig. (2.6e) as a function of the wavelength. The ratio between the energy scattered for these two positions of the tip has a 20% variation for the range of wavelengths shown in Fig. (2.6d). This is due to a change in the overlap between the mode and the input field caused by the dependence of the input field, and of the mode, on the wavelength. We note that for the disc considered here, contrary to what happens with spheres and infinite cylinders, the Maxwell's equations do not separate into a tangent and normal part, therefore there may be small variations in the tangent components of the modes at the surface of the disc as the wavelength is changed.

The surface electric field intensity, and the real part of the polarization, for the dominant mode of the $m = 0$ channel is shown in Fig. (2.6e), which is symmetrical

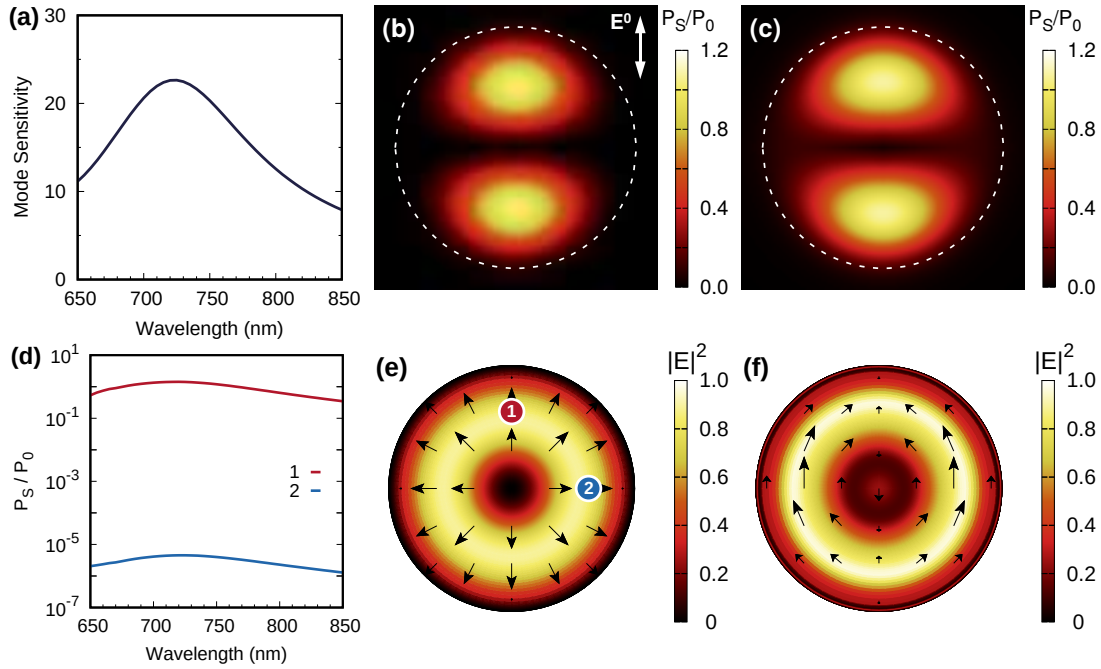

Figure 2.6: (a) Plot of the mode sensitivity, $\left(\sin^2\xi\right)^{-1}$, as a function of wavelength for the dominant $m = 0$ mode of the 400 nm diameter disc, where the $\cos\xi$ is the spatial correlation of internal and scattered surface fields of the mode. The plot shows the increase in excitability of the mode as it approaches its resonance at $\sim$ 725 nm. (b) Excitation map showing the contribution of the linearly polarized component of the dominant mode for the same channel. The scattered intensity, depicted by the color bar, is normalized to be in units of the incident field. (c) Excitation map, as in (b), but for all modes of the $m = 0$ channel. (d) The amount of energy scattered towards the detector (P_S) for the two positions of the fibre tip marked in (e), normalized by the power of the incident field (P_0), as functions of wavelength. The feature at *ca.* 675 nm is due to two pairs of modes becoming almost degenerate and mixing properties. (e) The surface electric field intensity and polarization of the real part of the electric field for the dominant $m = 0$ mode. (f) As in (e) but for the superposition of the dominant modes of the $m = \pm 1$ channels. The arrow in (b) indicates the incident field polarization for (b), (c) and (d).

about the axis of the particle. We show the top face of the disc, closest to the tip, but note that the intensity pattern and polarization distribution is the same on the bottom face. Due to the shallow depth of the particle, the rim of the disc does not support any sort of structure for this excitation. We expect that linearly polarized incident light will excite this mode in regions where the polarization of its surface electric field is closely aligned with the polarization of the incident field. This explains the two bright lobes shown in Fig. (2.6b), where the electric fields are anti-parallel. This mode accounts for over 85% of the light scattered by all of the modes in the $m = 0$ channel at 780 nm resulting in Fig. (2.6b) almost exactly matching the scattered intensity pattern of the entire $m = 0$ channel, shown in Fig. (2.6c). This corresponds to the bright parts in the transmission pattern of Fig. (2.5a), where I is nearly equal to I_0, *i.e.* the amount of scattered light received by the detector matches that without the disc present. The faint extra lobes evident, horizontally, in the outer parts of the transmission image of the $m = 0$ channel shown in Fig. (2.6c) are due to a weakly excited secondary mode.

We can conclude that the bright parts of the image depicted in Fig. (2.5a) are primarily due to a single mode of the disc. While the two dark lobes in this image, aligned horizontally along the direction perpendicular to the polarization of excitation, can be attributed mainly to the destructive interference of the two dominant modes of the $m = \pm 1$ channels with the incident field. We find that the electric fields in these two dark lobes, towards the edges of the disc, are parallel as shown in Fig. (2.6f). The surface projections (in the plane of the flat surface of the discs) of the polarization vectors for the two modes in the superposition depicted in Fig. (2.6f) are related by a reflection operation. The polarization projections of both modes predominantly point in the same direction along the vertical (wrt. the Figure) axis, and in the opposite directions along the horizontal axis. The resulting superposition shows that the maximum net intensity for these modes can be excited only for incident fields with a polarization component along this vertical axis. We also examined the origin of the negative peak around 650 nm observed in Fig. (2.2c), by calculating the correlation between spatial modes

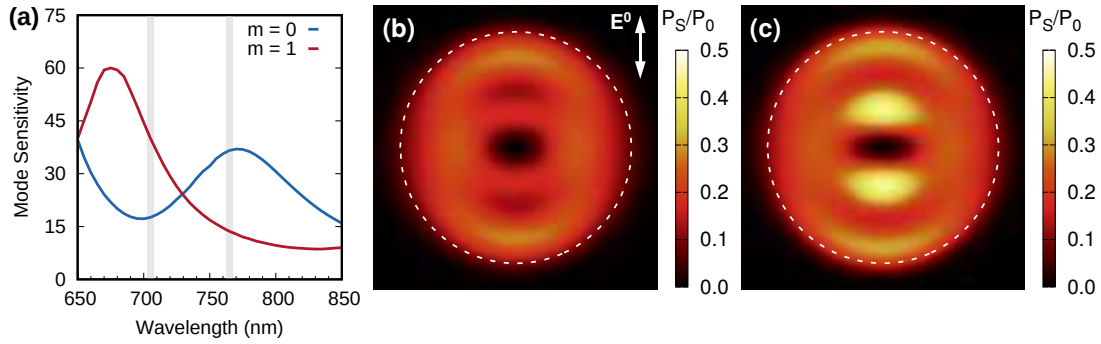

Figure 2.7: (a) Plots of the sensitivity, $\left(\sin^2\xi\right)^{-1}$, as functions of wavelength for the dominant modes of the $m = 0$ and $m = 1$ channels for the 800 nm diameter disc are shown where the axes are the same as Fig. (2.6a). (b,c) The normalized scattered intensity for the $m = 0$ channel far from resonance at 705 nm, (b), and close to it at 765 nm, (c), as indicated in (a).

excited in the near-field and the scattering channels transporting the radiation energy to the far-field. We found from the simulations that two modes of the $m = \pm 1$ channels are responsible for scattered light at ~ 650 nm, and one of the modes predominantly yields forward scattering, making a major contribution to the negative peak.

The near-field transmission images of the larger, 800 nm diameter, disc contain significant contributions from more than one m channel, each consisting of a greater number of modes than the smaller disc. The observed change of pattern with incident wavelength for the large disc, and indeed the relative contributions of the individual channels, can be explained in terms of modes moving on or off from resonance as the wavelength changes. When a radiating mode is close to resonance, it is excited with a greater amplitude and typically produces the majority of the observed far field intensity associated with that particular channel. Furthermore when a mode approaches the peak of its resonance it eclipses the contributions from the other modes, with up to 60% of the total energy radiated by that channel passing through the dominant mode in such cases. For the 800 nm diameter disc at 705 nm, Fig. (2.5b), we observe modes in both the $m = \pm 1$, shown in Fig. (2.7a), and $m = \pm 3$ channels approaching resonance (not shown). As such these channels strongly influence the observed pattern at shorter wavelengths. For the pattern at 765 nm, Fig. (2.5c), the $m = \pm 1$ and ± 3

modes have moved away from resonance and on the contrary, the modes of the $m = 0$ and ± 2 channels have moved towards resonance, and therefore have more influence upon the observed accumulated pattern, as highlighted in Fig. (2.7a).

Taking the $m = 0$ channel as an example, the dominant mode is near the peak of a resonance for the transmission image at 765 nm, Fig. (2.7c), while its scattered intensity is four times weaker at 705 nm, Fig. (2.7b), as it moves far from resonance. Scattering, combined with interference between some modes within both the $m = 0$ and $m = \pm 1$ channels determines the major features of the patterns, however there is also absorption present, particularly at the shorter wavelengths (primarily due to the $m = \pm 1$ resonant modes). These effects are also present for the 400 nm diameter disc, but are small compared to scattering by the dominant $m = 0$ mode.

We remark that in our calculation we have assumed a perfect axial symmetry; as a consequence, only the $m = \pm 1$ and (assuming some small polarization in the axial direction) the $m = 0$ channels can be excited by the incident field when the tip is on the symmetry axis. This is the origin of the dark spots at the very centre of Figs. (2.5a-c); breaking the axial symmetry would modify the centre of these images. As a result we would expect this region of the pattern to show the largest discrepancy between experiment and theory.

2.3 Summary

In this Chapter, we have discussed the operation of an aperture SNOM and identified a good model for the localised field. The localized plasmons in single gold nanodiscs have been studied by near-field spectroscopic imaging measurements, and we have found theoretically the plasmon modes that give rise to the spatial features of the experimental near-field transmission images. The observed near-field transmission images of the discs have characteristic spatial features that depend on the dimensions of the discs and the wavelength of observation, and can be quite complex.

In contrast to one-dimensional systems like nanorods, it is not straightfor-

ward to assign fundamental plasmonic modes to the near-field images of two-dimensional discs. Using the theory of principal modes, plasmonic modes were assigned to the near-field images of two-dimensional discs. We found that the simulated results reproduced the observed spatial features, and successfully assigned the observed images to fundamental modes of the systems. The advantages of this approach are obvious, as it gives a clear physical explanation of the experimental transmission images of non-spherical metal nanoparticles. By defining resonances of the plasmon modes, we are able to provide an intuitive description of the evolution of these patterns with frequency - as modes alternately move close to, and far from resonance.

The agreement of this analysis with the experiments demonstrates the advantage of the theoretical framework we describe over numerical methods such as FDTD or DDA in identifying the plasmon modes responsible for near-field transmission images. The small discrepancies between theory and experiment can be attributed to the simplified model of the true experimental conditions and geometry. Either including the substrate, or modelling the tip as a particle to account for coupling with the sample, would serve to improve the agreement. However, for the purposes of understanding the transmission images this effort is unnecessary.

Chapter 3

Coherent control

This Chapter presents the theoretical foundations for optical control schemes, designed to either maximize or suppress the modes of a nanostructure (as defined in Sec. 1.1) via the modulation of the amplitudes and phases of coherent light sources. Additionally, we present numerical results obtained for different models and processes which have been published in [152, 153, 154]. We consider particles with both a local and nonlocal optical response, as well as elastic and inelastic scattering processes. Particles with spatially nonlocal responses behave very differently from particles with a local response as they support irrotational charge density waves, such as plasmons, that do not radiate and can reach the central region of the particle over a large range of frequencies; on the contrary, particles with local responses support longitudinal modes only when the real part of the electric permittivity ϵ is null [155]. In our analysis, we will primarily focus on individual spherical particles in a homogeneous medium, similar to a colloidal suspension, as in this case the theory is fully analytical. However, the approach we develop is based on the interference of fields at the surface of the particle and can be applied whenever longitudinal and transverse waves are allowed, independent of the shape of the particle or the origin of the longitudinal waves.

3.1 Principles of coherent control

3.1.1 General theory for principal modes

In Ref. [51], a general analytical theory was developed for the control of the modes of scattered and internal fields in nano-structures of any shape, and at any frequency, which allows us to either enhance or suppress internal and/or scattered fields and determine their spatial distribution or angular momentum. Most importantly, we can design the lineshape of the particle and introduce very narrow features in its spectral response. This method requires varying the relative amplitudes and phases of $N + 1$ incident fields in order to control N channels. Each pair of principal modes provides an interaction channel for the incident light [23]: some of the scattering modes efficiently transport energy into the far field, while others are mostly limited to the near field region around their nano-structure [53]. Depending on the channels involved, it is possible to determine the flow of energy outside the particle by controlling the scattered field in the far and/or in the near field regions, or the absorption of energy by the particle through controlling the amplitude of the internal field.

We consider here incident fields that are commonly available in experiments and can be monochromatic or broad band. A practical implementation requires simply the control of the relative phases of incident fields and can be achieved using only one source of light together with beam splitters and phase modulators, or a mixture of sources, which may also be impurities embedded in the nano-particle, such as atoms, molecules or quantum dots. Some simple sketches of experimental set-ups suitable to implement this theory are provided in Fig. (3.1). The coherence length of such sources has to be of the order of the size of the particle, so even conventional lamps may be used in some applications, as long as the difference between the optical paths from the sources to the particle is within the coherence length. The internal sources may emit radiation at the frequency under control not only through elastic scattering, but also through inelastic scattering and nonlinear processes such as harmonic generation and amplification of light at the nano-scale. Therefore our approach can be used to also optically control

non-linear processes. In the following we use principal modes to derive the control conditions for fields at the surface of a particle, consider the types of light sources able to implement those conditions and show some numerical illustrations of these ideas. It has been previously demonstrated [51] that a simple parameter scan is sufficient to find optimal control conditions even without a detailed knowledge of the modes of the particles, as would be the case in most practical applications.

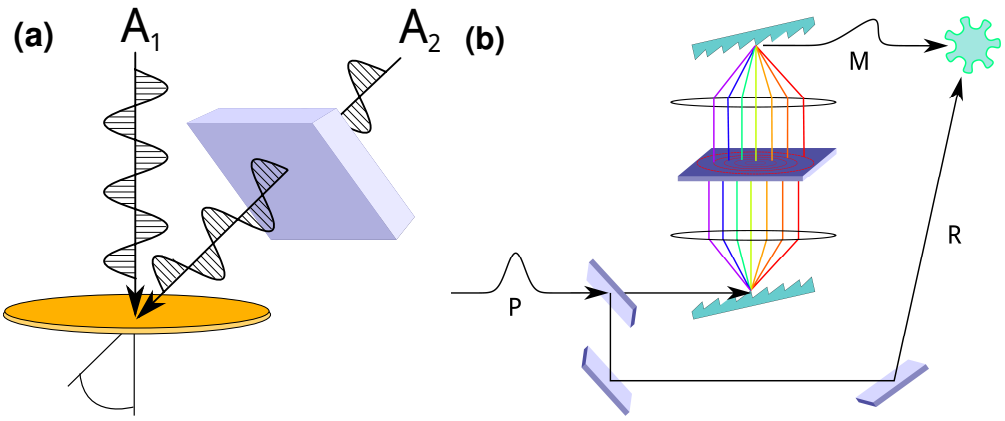

Figure 3.1: Suggested experimental geometries for control of optical channels. a) Monochromatic incident light fields approaching a disc shaped nano-structure to change the amplitudes of a specified principal mode, two independent light sources with amplitudes A_1 and A_2 and a specified relative phase $\Delta\Phi$ are used. b) A more general spatial-light modulator approach for changing phase and/or amplitude over a range of wavelengths for a broad-band source or an applied pulse of light. Here the incident light pulse (P) is split into two paths, with one being dispersed and its complex amplitude modified as a function of wavelength (M), before being re-combined and applied to the nano-structure together with the light which followed the second reference path (R).

3.1.2 Maximization and suppression of principal modes

The relative orientation of the n^{th} set of principal modes and their related biorthogonal modes, $\boldsymbol{i}'_n$ and $\boldsymbol{s}'_n$, allows the amplitudes a^i_n, a^s_n for any incident field [51] to be found, as is shown schematically in Fig. (1.1). The spatial correlations between internal and scattered mode pairs enables, using the geometry of a non-orthogonal basis of vectors [79], the determination of the surface fields which will excite $\boldsymbol{s}_n$ but not $\boldsymbol{i}_n$ (or $\boldsymbol{i}_n$ and not $\boldsymbol{s}_n$), or that produces the largest amplitude for modes

$\boldsymbol{s}_n$ or $\boldsymbol{i}_n$, see Fig. (1.1). Any incident field can be decomposed as $\boldsymbol{f} = \boldsymbol{f}_n + \boldsymbol{f}_n^{\vee}$, with $\boldsymbol{f}_n$ the part of the incident field that couples only with the n^{th} modes and $\boldsymbol{f}_n^{\vee}$ being the part that does not. This leads to the results,

$$\boldsymbol{f}_n = \boldsymbol{s}_n \rightarrow a_n^s = 1,\ a_n^i = 0, \tag{3.1}$$

$$\boldsymbol{f}_n = \boldsymbol{s}_n' \rightarrow a_n^s = \frac{1}{\sin(\xi_n)},\ a_n^i = -\frac{\cos(\xi_n)}{\sin(\xi_n)}. \tag{3.2}$$

Eq. (3.1) gives the requirement for incident fields that, irrespectively of $\boldsymbol{f}_n^{\vee}$, produce excitation of only the scattering mode, *i.e.* a null amplitude for the corresponding internal mode. Alternatively the amplitude of the scattering mode with the largest conversion factor $|a_n^s/\boldsymbol{f}_n|$ is obtained for fields of the form of Eq. (3.2). The analogous conditions for $\boldsymbol{i}_n$ are found by exchanging s with i in Eqs. (3.1, 3.2).

Two points are worth noting. First, these are exact conditions for the surface fields that are valid at any frequency and have two possible applications: control of a mode (or modes) over a range of frequencies and the introduction of narrow band features in the spectral response of the particle. Second, the largest excitation factor for a mode is not achieved through single mode excitation, but by an optimal excitation that produces amplitudes in the two principal modes of the channel. For physical applications it is necessary to generate incident fields which have tangent components that fulfil Eqs. (3.1), or (3.2). The case $\boldsymbol{f} = \boldsymbol{s}_n$ can be in principle realised through time reversal of the lasing mode of an amplifier with the same shape as the particle and gain opposite to the loss [40] at the resonant frequency of the mode. To experimentally realise this is quite challenging, as radiation would need to converge towards the particle from all directions. We are instead interested in deriving general conditions for optimal excitation of modes at any frequency with easily accessible sources of radiation. In general, an incident field $\boldsymbol{F}(\mathbf{r})$ with tangent components $\boldsymbol{f} = \boldsymbol{i}_n$ or $\boldsymbol{f} = \boldsymbol{s}_n$ cannot be realised using common sources of radiation external to the particle, such as laser beams or SNOM tips, or even internal sources such as fluorescent or active hosts. This is because these sources emit waves that are neither outgoing radiating waves in the external medium, as is the scattering mode, $\boldsymbol{s}_n$, nor standing waves in the

internal medium, such as the internal mode, $\boldsymbol{i}_n$. However, by combining two or more of these sources with appropriate phases and amplitudes, it is possible to control in a simple and effective way the few dominant interaction channels of any nano-particle. To construct fields to realise the conditions of Eqs. (3.1) or (3.2) requires two linearly independent incident fields, $A_1\boldsymbol{f}^1$, and $A_2\boldsymbol{f}^2$, both coupled to the channel n, such that

$$\frac{\boldsymbol{s}_n \cdot \boldsymbol{f}^1}{\boldsymbol{s}_n \cdot \boldsymbol{f}^2} \neq \frac{\boldsymbol{i}_n \cdot \boldsymbol{f}^1}{\boldsymbol{i}_n \cdot \boldsymbol{f}^2}. \tag{3.3}$$

The condition for the suppression of $\boldsymbol{i}_n$ is

$$A_2 = -A_1 \frac{\boldsymbol{i}'_n \cdot \boldsymbol{f}^1}{\boldsymbol{i}'_n \cdot \boldsymbol{f}^2}, \tag{3.4}$$

while the condition for the maximal conversion factor for $\boldsymbol{s}_n$ becomes

$$A_2 = -A_1 \frac{\boldsymbol{i}_n \cdot \boldsymbol{f}^1}{\boldsymbol{i}_n \cdot \boldsymbol{f}^2}, \tag{3.5}$$

with A_1, A_2 being complex amplitudes that can be experimentally adjusted through phase plates and dichroic elements, Figure (3.1a) suggests a geometry for constructing these fields, while a numerical example of scanning the relative complex amplitude to produce specific scattered light is shown later. Analogous conditions for optimisation of $\boldsymbol{i}_n$ and suppression of $\boldsymbol{s}_n$ can be found by swapping $\boldsymbol{i}_n, \boldsymbol{i}'_n$ with $\boldsymbol{s}_n, \boldsymbol{s}'_n$ in Eqs. (3.5, 3.4): the generalisation of Eq. (3.5) to a larger number of modes can be found in Ref. [51].

The conservation of energy applies to the incident scattered and internal fields, but not necessarily to each interaction channel separately. However, if incident fields with $\boldsymbol{f}_n \neq 0, \boldsymbol{f}_n^{\vee} = 0$ exist, the conservation of energy applies to the n channel. From the Stratton-Chu representations [85] it can be shown [51] that for particles where the dependence of the electric (and magnetic) parts of $\boldsymbol{i}_n, \boldsymbol{s}_n, \boldsymbol{f}_n$ on the surface coordinates is the same, such as for spheres and infinite cylinders, the ratios in Eq. (3.3) depends on the flux of energy of the incident field into the particle, and Eq. (3.3) is *always* violated when the sources are both either outside or inside the particle. For instance, in the case of a sphere any external source can be expanded by the set of regular multipoles with angular indexes l, m, while

any internal source is expanded by the set of radiating spherical multipoles [51]. In this case the amplitudes of internal and scattering modes cannot be controlled by independent external – or internal – sources: Eqs. (3.5, 3.4) become equivalent and lead to the simultaneous suppression of both $\boldsymbol{i}_n$ and $\boldsymbol{s}_n$, while the maximisation of the amplitudes of both scattering and internal modes is provided by ensuring that the contributions of the incident fields to the amplitudes add in phase. However, the condition for maximal excitation, Eq. (3.5), or suppression of a mode, Eq. (3.4), can be fulfilled also for spheres at any frequency provided one incident field is generated by an external source and the other by an internal source, or that one incident field is a regular wave with a power flow of $W_n = 0$ and the other an incoming wave with $W_n \neq 0$. Important examples of internal sources are bulk and surface nonlinear processes, which we consider in the following sub-section. Incoming waves are more difficult to realise, but could be in principle obtained through time reversal techniques [41].

3.1.3 Controlling lineshapes via principal modes

Using the spectral region around the resonance of a gold disc as an example, Figure (3.2) shows an approach to produce sharper line widths with a chosen line shape and peak position. Here, three incident fields have been selected which cancel the main optical resonance of the disc in both $m = \pm 1$ channels, effectively removing interaction of the incident light with the particle. The fields consist of an axially incident plane wave light, light incident equatorially and light incident at 45 degrees to the particle axis, chosen such that the equatorial light source amplitude was 1. Then, on scanning the wavelength of the light over the range, the phase (but not the amplitude) of the axial and 45 degree incident light was modulated according to a Gaussian profile, shifting their phase from being at the cancelling combination to π out of phase with this over a narrow range of wavelengths. Figure (3.2) shows the results of choosing to remove the cancellation of the amplitudes at three different wavelengths. Equivalently different Gaussian widths, or a different line profile could be chosen. Here, modulation of phase is being transferred into modulation of amplitude. This leads to a change between

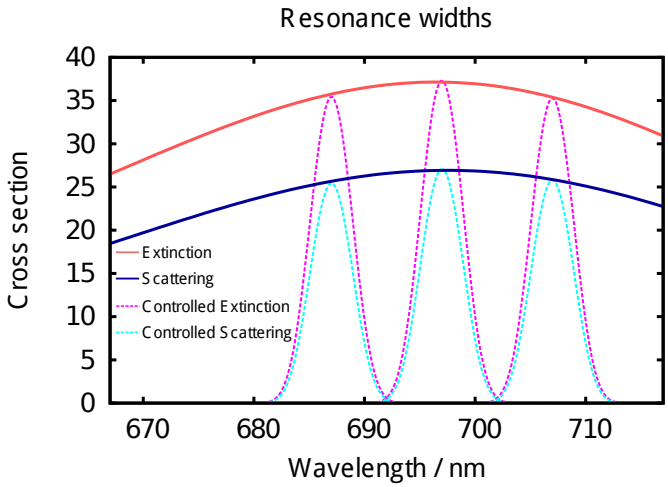

Figure 3.2: Cross sections of a rounded gold disc (20 nm thickness and 60 nm radius) with standard axial incidence, leading to a broad feature in the extinction (red) and scattering (blue). These are compared against its response to illumination of light from three directions (axial, 45° and 90° incident) with their relative phases (but not amplitudes) modulated to cause constructive interference only at a selected wavelength, then rotating the phase to cause destructive interference according to a Gaussian envelope, producing a specified location and line width feature within the envelope of the original broad peak.

a situation where cancellation occurs, and a strong surface field and radiated light when the cancellation is disrupted. Experimentally, an approach similar to Figure (3.1b) may be able to produce the required change in phase of light over a narrow frequency range.

3.2 Including nonlocality in Maxwell's equations

3.2.1 The hydrodynamical model

In this Section, we extend the general theory outlined in Sec. 3.1 to include particles, or structures, with a nonlocal response to electromagnetic fields. When one of the characteristic dimensions of the particle (or structure) is of the order of the electron mean free path, the free current is governed by a nonlocal equation that admits longitudinal waves. In the hydrodynamical model [156, 157, 158, 159, 160, 161], the nonlocal response is modelled semi-classically by considering

the free charges in the metal as a fluid governed by the linearized Navier-Stokes equation, with a pressure term that has a quantum origin and is proportional to the Fermi velocity. The interaction of the particle with light is then given by Maxwell's equations combined with the linearized Navier-Stokes equations [162],

$$\nabla \times \boldsymbol{E} = -\mu \partial_t \boldsymbol{H}, \tag{3.6}$$

$$\nabla \times \boldsymbol{H} = \partial_t [\epsilon_b \boldsymbol{E} + \boldsymbol{P}_f], \tag{3.7}$$

$$(\partial_{tt} + \gamma_f \partial_t - \beta^2 \nabla\nabla\cdot)\boldsymbol{P}_f = \epsilon_0 \omega_p^2 \boldsymbol{E}, \tag{3.8}$$

where $\boldsymbol{E}$, $\boldsymbol{H}$ are the electric and magnetic fields, $\boldsymbol{P}_f$ is the polarization due to the free current density $\boldsymbol{J}_f$ ($\partial_t \boldsymbol{P}_f = \boldsymbol{J}_f$), ϵ_b is the electric permittivity due to the bound charges, γ_f is the damping factor due to collisions of the free charges, ω_p is the plasma frequency of the material and $\beta^2 = (3/5)v_F^2$, with v_F the Fermi velocity. The nonlocal term, $\nabla\nabla \cdot \boldsymbol{P}_f$, in Eq. (3.8) affects the interaction of the particle with light in two ways. First, the electric field contains both a transversal part $\boldsymbol{E}_T$ ($\nabla \cdot \boldsymbol{E}_T = 0$) and a longitudinal part $\boldsymbol{E}_L$ ($\nabla \times \boldsymbol{E}_L = 0$), each with it's own dispersion relation, see Appendix B.2. The longitudinal waves are expanded in terms of the longitudinal solutions of the Helmholtz equation and are associated with charge density waves, such as plasmons, but not to radiation as $\boldsymbol{E}_L$ is decoupled from time-dependent magnetic fields. Secondly, Eq. (3.8) also modifies the interaction with light through an additional boundary condition that is necessary to determine $\boldsymbol{P}_f$. This boundary condition is considered together with the usual continuity of the tangent components of $\boldsymbol{E}$ and $\boldsymbol{H}$ [66].

In media that do not support a surface density of free charges, the component of the free current density normal to the boundary of the particle is continuous [160, 161]. At a dielectric-metal interface, this condition implies that the normal component of $\boldsymbol{P}_f$ in the metal has to vanish at the boundary, as dielectrics do not support free currents. Using the integral form of the divergence theorem and an infinitesimal pillbox on the right-hand side of Eq. (3.7) shows that the normal component of $\epsilon_b \boldsymbol{E} + \boldsymbol{P}_f$ is also continuous at the boundary. Therefore the continuity of the normal component of $\boldsymbol{P}_f$ is equivalent to the continuity of the

normal component of $\epsilon_b \boldsymbol{E}$, which provides the additional boundary condition,

$$\hat{\boldsymbol{n}} \cdot \epsilon_b^i \boldsymbol{E}^i = \hat{\boldsymbol{n}} \cdot \epsilon_b^e (\boldsymbol{E}^s + \boldsymbol{E}^0), \tag{3.9}$$

where ϵ_b^e, ϵ_b^i are the permittivity due to bound charges of the external and internal media respectively, and $\boldsymbol{E}^i$, $\boldsymbol{E}^s$, $\boldsymbol{E}^0$ are the internal, scattering and incident fields.

By taking the divergence of Eq. (3.7) we find $\nabla \cdot \boldsymbol{P}_f = -\nabla \cdot \epsilon_b \boldsymbol{E}$, which can be used to find the dispersion relation of the longitudinal waves and to recast the Maxwell equations in terms of the longitudinal and transverse electric fields; we can then use the boundary conditions to determine the amplitudes of the longitudinal and transverse waves. The additional boundary condition in Eq. (3.9), and the presence of $\boldsymbol{E}_L$, leads to modified Mie coefficients [163] for the sphere. We note that in [156], the authors claim that it is not physically possible to distinguish between free and bound charges and, therefore, that it should be the normal component of the total current which is continuous at the surface. Using a similar approach as the one above, this assumption is equivalent to the continuity of the normal component of the electric field [157]. There is very limited difference in the numerical results given by these two additional boundary conditions and no experimental evidence to support one over the other.

3.2.2 Mode structure

At the heart of our theory is the Stratton-Chu representation theorem that allows one to express any internal and scattered fields of any smooth (possibly inhomogeneous) particle in terms of integral operators acting on the electromagnetic fields at the surface of the particles [164]. In practice this means that the response of a particle to light generated by impressed driving sources (which are either internal or external) can be determined by expanding the internal and the scattered fields in terms solutions of Maxwell's equations for the internal and the external media that can approximate any field incident to the surface of the particle, from the inside or the outside, with arbitrary precision [23]. By defining surface fields with the electric and magnetic component parallel to the surface of the particle as,

$$\boldsymbol{f} \equiv [-\hat{\boldsymbol{n}} \times (\hat{\boldsymbol{n}} \times \boldsymbol{E}), -\hat{\boldsymbol{n}} \times (\hat{\boldsymbol{n}} \times \boldsymbol{H})]^{\mathrm{T}}, \tag{3.10}$$

where T means transpose, $\hat{\boldsymbol{n}}$ is the unit vector normal to the surface, and the scalar product of two surface fields is the overlap integral,

$$\boldsymbol{f}_1 \cdot \boldsymbol{f}_2 = \sum_{i=1}^{3} \int_S \boldsymbol{f}_{1i} \boldsymbol{f}_{2\,i}^* \mathrm{d}s, \tag{3.11}$$

where the index i labels the components of an arbitrary system of coordinates, the coefficients of the Mie modes of a sphere with local response are determined by projecting the incident fields on these modes using analytical formulae based on the scalar product defined on the surface [51]. These formulae apply also to particles whose modes can be found only numerically [23] and are very useful to determine the phase and amplitude of coherent light sources in order to modify the linear [51] and nonlinear [152, 153] response of nanoparticles, as we shall see in the following Sections.

For particles with nonlocal response, one has also to include a complete set of longitudinal modes of the electric field corresponding to the plasmons; the coefficients for transverse and longitudinal modes can be calculated by fulfilling the continuity of the transverse component of the electric and magnetic fields as well as the boundary condition in Eq. (3.9) on the normal component of the electric field. To take into account Eq. (3.9), we need to also include the normal part of the electric field in the definition of the surface fields so that they now have five components,

$$\boldsymbol{f} \equiv [\hat{\boldsymbol{n}} \cdot \epsilon_b^{i/e} \boldsymbol{E}, -\hat{\boldsymbol{n}} \times (\hat{\boldsymbol{n}} \times \boldsymbol{E}), -\hat{\boldsymbol{n}} \times (\hat{\boldsymbol{n}} \times \boldsymbol{H})]^{\mathrm{T}}, \tag{3.12}$$

where ϵ_b^e is used for scattered and external fields, and ϵ_b^i is used for the internal field[1]. The scalar product between surface fields is modified accordingly, and is given by the sum of the overlap integrals of these five components.

3.2.3 Size dependent effects

When we consider particles with dimension(s) smaller than or comparable to the mean free path of conduction electrons in the bulk material, size dependent effects

[1]Using the additional boundary condition described in [156, 157], the first component of Eq. (3.12) should be replaced by $\hat{\boldsymbol{n}} \cdot \boldsymbol{E}$.

become important when we try to determine the optical properties. A useful list of the mean free paths of 20 of the most common conductive metals, including the noble metals typically used in nanophotonic experiments, is provided in Ref. [165] along with other material properties. For particles governed by a local response, where the electrons are free to move, these effects arise from an increase in the collisions of the electrons along these dimensions. In this case, it is sufficient to account for these collisions by defining an *effective* mean free path along these dimensions such that the damping term in the dielectric function, $\epsilon \equiv \epsilon(\omega)$, is increased by a factor which is dependent upon the size of the particle [149]. For a Drude type dielectric function this leads to an expression of the form,

$$\epsilon(\omega) = 1 - \frac{\omega_p^2}{\omega^2 + i\omega\left(\gamma_0 + A\dfrac{v_F}{l_{\mathit{eff}}}\right)} + \epsilon_b(\omega), \tag{3.13}$$

where the free electron (intraband) contribution has been corrected with respect to the expression for a bulk material. where the last term acts as a correction of the bound electron contribution, $\epsilon_b(\omega)$. Here ω is the frequency of excitation, $\epsilon_b(\omega)$ is the bound electron (interband) contribution, A is an empirical amplitude[2] which moderates the damping, v_F is the Fermi velocity, and the effective mean free path $l_{\mathit{eff}} = 4V/S$, where V is the volume of the particle and S is the surface area. The second term on the right hand side of equation (3.13) is the standard Drude expression for free electrons, where ω_p is the plasma frequency of the bulk material and γ_0 is the damping constant.

For a nonlocal response, we should consider quantum effects as a consequence of modelling the free electrons as a fluid. A complete quantum treatment is impractical for nanoparticles, consisting of hundreds of atoms, and also unnecessary in most cases. These quantum effects can instead be modelled by considering electron diffusion acting in concert with convection. The recently developed generalized nonlocal optical response theory (GNOR) [166] models damping in this way, and provides an effective analytical method for including these effects by defining a nonlocal parameter. Free carrier diffusion is incorporated via the diffusion constant $D \simeq v_F^2\tau_s$, where, for metals, the relaxation time associated to

[2]The amplitude A is typically assumed to be close to unity.

scattering processes can be approximated for spherical particles as $\tau_s \sim 4/\omega_p$. We remark that, as $D \to 0$ the damping model effectively reduces to the familiar Kreibig size dependent model for spheres[17], similar to Eq. (3.13).

In the Sec. 3.3.2, we wish to directly compare the effects of control for both a local and nonlocal response, and so we employ the local size-dependent damping model as it can be applied to both cases. To support this decision, in Fig. (3.5b) we show that the specific choice of damping model has little effect on the control for the nonlocal response.

3.3 Elastic scattering: Local *vs.* nonlocal response

3.3.1 Application to spheres

In this Section, we apply the boundary conditions derived in the previous Section to metallic nanospheres in order to investigate the effect of the coherent control method for both a local and nonlocal response (Sec. 3.3.2). Particles with nonlocal responses exhibit a shift of the main resonance with respect to particles with local response for the same geometry and, in some metals, also have extra resonances at short wavelengths [156, 157, 158, 159, 160, 161]. From the point of view of control, the main difference is that in media with a nonlocal response we can use light to control not only the internal and scattered fields, but also currents (or plasmons). In the following Section (Sec. 3.4), we shall provide a more rigorous description for the coherent control of second-harmonic generation in nanospheres with diameters of at least 50 nm, for which nonlocal effects may be important only in a very thin layer at the boundary of the particles where nonlinear processes take place. For gold (spherical) particles with radii $\lesssim 50$ nm, it has been shown that the second harmonic response can be very well approximated using only a single surface term from the nonlinear susceptibility [167], hence for particles of this size the longitudinal (nonlocal) contribution from bulk nonlinearities can be neglected. Here, we shall first investigate smaller nanoparticles, with radii ≤ 5 nm, in which the nonlinearity is due to an impurity, or colour centres, inside the particle and for which nonlocal effects are important not only at the surface.

In order to control the response of the nanosphere, we have to change the relative amplitudes of the modes that most affect the overall response of the particle. As a consequence of the spherical symmetry, only modes with the same value of l (orbital angular momentum) and m (angular momentum along z) can couple. For each value of l and m, using the angular dependence, one can group the modes into two sets: the set of transverse electric (TE) modes–as in a sphere with local response–and a set of two internal modes (the transverse magnetic (TM) and the longitudinal mode) and the transverse magnetic scattering mode. For very small nanospheres the dominant modes are the second set, the transverse magnetic modes, with $l = 1$. To describe effects that are most easily observed experimentally, we concentrate here on the control of two out of the three dominant modes using two coherent light sources with surface fields ($\boldsymbol{f}_1$ and $\boldsymbol{f}_2$) that are functions of the position on the surface. The real amplitudes and phases of these fields are encoded in their complex amplitudes A_1, A_2. As the third mode with the same l and m is not *directly* controlled, the choice of which pair of modes to control depends on whether we want to affect the light or the current. The amplitude of the scattering mode, $\boldsymbol{s}$, and of an internal mode $\boldsymbol{i}$, are given by,

$$\begin{bmatrix} a_i \\ -a_s \end{bmatrix} = \begin{bmatrix} \boldsymbol{i}' \cdot \boldsymbol{f}_1 & \boldsymbol{i}' \cdot \boldsymbol{f}_2 \\ \boldsymbol{s}' \cdot \boldsymbol{f}_1 & \boldsymbol{s}' \cdot \boldsymbol{f}_2 \end{bmatrix} \begin{bmatrix} A_1 \\ A_2 \end{bmatrix} \tag{3.14}$$

where $\boldsymbol{i}'$ ($\boldsymbol{s}'$) is the biorthogonal mode [168] that is orthogonal to all modes other than $\boldsymbol{i}$ ($\boldsymbol{s}$), see Appendix B.3 for the explicit formulae. Similarly, one could use the second internal mode, $\boldsymbol{j}$, instead of the scattering mode, replacing $\boldsymbol{s}'$ with $\boldsymbol{j}'$ and $-a_s$ with a_j, where the minus sign originates from the boundary condition and is due to the fact that internal and scattering modes are defined on opposite sides of the surface.

For a sphere [51, 152], the matrix in Eq. (3.14) is invertible only if the functional dependence of $\boldsymbol{f}_1$ on the position on the surface is different from that of $\boldsymbol{f}_2$; as mentioned in Sec. 3.1.2. Physically, this means that we can use a laser and either a converging or diverging spherical wave, but not two lasers or two converging or diverging waves. Note that using a standard external source and both a converging and a diverging wave with a given l and m, it is possible to

control the amplitude of three modes with the same l and m. For instance, one could suppress both internal modes, eliminating absorption for that l and m channel. Due to the considerable challenges involved in realising converging spherical waves at the nanoscale, we will concentrate instead on diverging, or outgoing, waves. Dipole radiation can be excited by an impurity or colour centre of size <1 nm (an order of magnitude smaller than the size of the sphere such that it does not affect significantly the bulk properties of the sphere) located anywhere inside the sphere through any nonlinear up- or down-conversion process of a field at a different frequency [169]. The outgoing dipole radiation has total angular momentum $J = 1$ with respect to the centre of the impurity, and can be decomposed in terms of spherical waves with $l = 0, 1, 2$ and $m = 0, \pm 1$ [170], where the value of m to consider depends on the specific nonlinear process used. Using the translation theorem for spherical waves [66], we see that these waves radiated from the dipole can be recast as a superposition of spherical waves emerging from the centre of the sphere, but with angular momentum with respect to the centre of the sphere that can be larger than 2. However, for spheres of the dimensions considered here, the response to waves with $l > 1$ is extremely weak and can be safely neglected.

Here we shall use modes with indexes $l = 1, m = 0$, which corresponds to assuming that one of the two waves is generated through a second harmonic process by an impurity at the centre of the sphere [171], but the principles of control are independent of m. Modes with $l = 1$ would still dominate the response of the particle with an off-centre impurity, but one may have to consider also modes with $m = \pm 1$, including as many external control beams as m-values one wishes to control. From a theoretical point of view, the matrix in Eq. (3.14) will then include two extra modes for each additional m-value [51]. In principle an off-centre position would be detectable by measuring the relative amplitudes of the $m = -1, 0, 1$ channels, which would have to be controlled separately. An estimate of the relative amplitudes with respect to the centred impurity is provided by the translation theorem for vector spherical wave functions and is at most of the order of the ratio between the distance of the impurity from the centre of the particle

and the wavelength, and so for our purposes would be extremely small.

3.3.2 Control of light and currents with light

We consider in the following aluminium spheres primarily of 5 nm radius producing resonances in the ultraviolet region, as these particle should be easily available in experiments. These particles exhibit a blue-shift of the main resonance with respect to particles with local response for the same geometry but do not show extra resonances at short wavelengths. At the end of the Section we include results for smaller particles to demonstrate that the control methods work in principle even for a smaller particle, $r = 1.5$ nm, which does exhibit these additional resonances, as well as for an intermediate particle, $r = 3$ nm. Particles of this scale have been previously studied theoretically [161] as they are above the length scale where core plasmons are significant. However, it is difficult to realize smooth spheres with these dimensions which contain very small impurities or colour centres; for this reason we focus more on the 5 nm radius case.

In Fig. (3.3a) we compare the extinction power spectra for an aluminium particle of this size, both with and without nonlocal effects, and show in Fig. (3.3b) that the particle response is dominated by absorption. The dielectric function (and material properties) for aluminium are taken from Ref. [172], and we include an additional size dependent damping term as described in Sec. 3.2.3. In the following, when investigating the effects of control in both the local and nonlocal regimes we consider excitation photon energies which are greater than the minimum photon energy corresponding to the first ionization enthalpy of the material (577.54 kJ/mol $\rightarrow \hbar\omega = 5.98$ eV). We do so to highlight the effect of the control upon the nonlocal (longitudinal) modes, which have resonances above the plasma frequency ($\hbar\omega = 14.94$ eV). However, the method described works independently of the specific excitation frequency and so ionization of the sample can be avoided by working at frequencies below this limit.

In view of experimental realization, it is important to consider that the effects we show in the following can be qualitatively observed even when knowing the effective parameters of the particles with an uncertainty of $10 - 20\%$, as is often

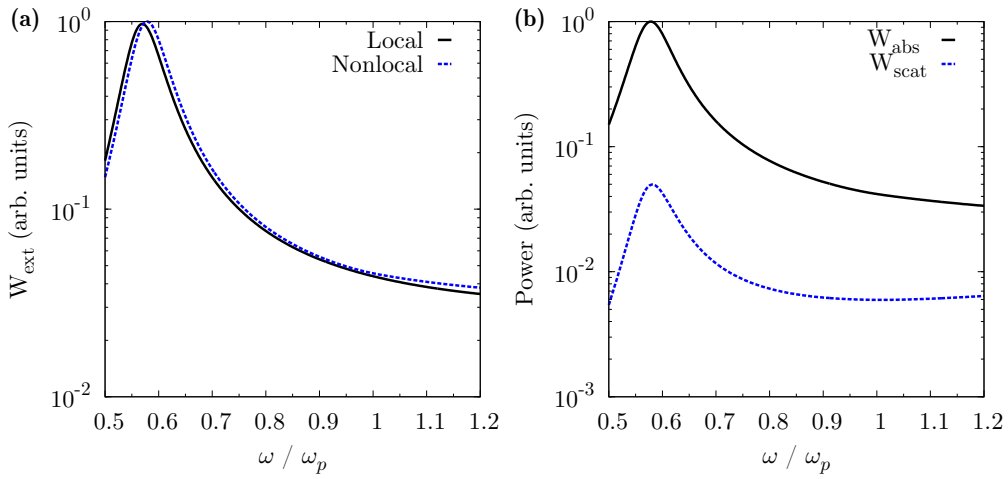

Figure 3.3: An aluminium sphere of radius 5 nm in vacuum is excited by a plane wave with unit amplitude. The plasma frequency $\hbar\omega_p = 14.94$ eV and the Fermi velocity $v_F = 1.95 \times 10^6$ m/s [172]. (a) Extinction power over 4π sterad. as a function of normalised frequency for a local and nonlocal response. (b) Total scattered and absorbed power for the nonlocal response. We observe that absorption dominates the response of the particle.

the case [101]. For instance, as long as $|A_1 \boldsymbol{s}' \cdot \boldsymbol{f}_1|$ and $|A_2 \boldsymbol{s}' \cdot \boldsymbol{f}_2|$ are of the same order, we can control the total scattered energy and introduce sharp spectral features in the scattering spectrum [152] simply by scanning the relative phase between $\boldsymbol{f}_1$ and $\boldsymbol{f}_2$.

In this example, the control field $\boldsymbol{f}_1$ is a linearly polarized plane wave incident at $\pi/2$ with respect to the z axis (defined by the propagation direction of the pump) and $\boldsymbol{f}_2$ is an outgoing spherical wave with $l = 1$, $m = 0$; which represents the dominant term resulting from the selection rules for second harmonic generation by an impurity, excited by a pump at half the harmonic frequency. For simplicity, the amplitude A_2 is normalized to unity while the amplitude A_1 is found by expanding the external control wave in terms of spherical harmonics [66].

In practical applications the efficiency of the nonlinear process generating $\boldsymbol{f}_2$ would always be less than unity and consequently the amplitude of the control wave would always be significantly smaller than that of the pump. We note that the size of the particles considered is smaller than the skin depth, so that a large fraction of the pump can reach the impurity. For sake of simplicity, we also assume the impurity is at the centre of the sphere, but we point out that moving

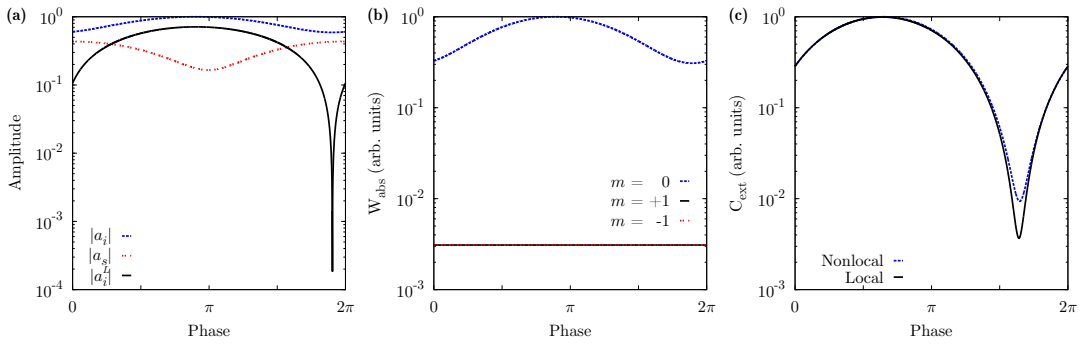

Figure 3.4: Same particle as in figure 3.3. Control on the $l = 1, m = 0$ internal longitudinal mode at $\hbar\omega = 16.96$ eV where the spherical wave, $\boldsymbol{f}_2$, has an amplitude $|A_2| = 1$ and the external control wave, $\boldsymbol{f}_1$, has an amplitude $|A_1| = 3.448 \times 10^2$. (a) Minimization of the amplitude of the longitudinal mode via relative phase of radiation sources; the point where $|a_i^L| = 0$, to within numerical resolution, has been removed to avoid compressing the plot. (b) Reduction in the total power absorbed by the internal fields decomposed into separate m channels for $l = 1$, where we observe that only the $m = 0$ channel is affected by the control. (c) Variation in the extinction cross section C_{ext} for a small detector having an acceptance half angle of 10 degrees. As the extinction is dependent upon both scattering and absorption, the observed minimum is shifted with respect to the minimum of $|a_i^L|$ in (a) as the internal and scattered modes are out of phase. The solid black trace shows the extinction calculated when the control parameters designed for the nonlocal model are applied to the local model.

the impurity off centre would produce terms with different values of l which do not change significantly the response of spheres of the dimensions considered here.

We can control the relative amplitudes of the internal Mie modes and, as a consequence, the distribution of currents and the absorption of energy due to the two internal modes for a given l, m channel. Using Eq. (3.4) with $A_2 = 1$, and Eq. (3.14), we can solve for the complex amplitude of the plane wave control field A_1, and hence the real amplitude and phase, required to minimize the amplitude of the longitudinal mode $\boldsymbol{i}_{10}^L$. In Fig. (3.4) we switch off this mode, at a frequency far from the resonance ($\omega/\omega_p = 1.136$) in Fig. (3.3), and show the effect of the control upon the power absorbed by the particle as a function of the relative phase between $\boldsymbol{f}_1$ and $\boldsymbol{f}_2$. We observe that only the intended channel, $m = 0$, is affected by the control.

This effect could be best observed experimentally by looking at the extinction

cross section, as demonstrated in Fig. (3.4c). To better represent the type of signal that would be detected in an experiment, we integrate over a small solid angle the Poynting vector associated to the interaction between the external control field and the far field asymptotic form of the scattered field ($\boldsymbol{E}^s_\infty$), which can be expressed as [66],

$$\mathrm{C}_{\mathrm{ext}} = \int_\Omega \mathrm{Re}\big[C^s \left(\boldsymbol{E}^{0*} \cdot \boldsymbol{E}^s_\infty\right) \exp^{-i\boldsymbol{k}_0 \cdot \hat{\boldsymbol{r}}}\big] \mathrm{d}\Omega, \tag{3.15}$$

where $C^s = \sqrt{\epsilon^e/\mu^e}$ is related to the electromagnetic properties of the external medium, and $\boldsymbol{k}_0$ is the wave vector for the external control wave[3]. As the local model has no analogue to the longitudinal mode, we simply apply the parameters used to control this mode for the nonlocal system in order to investigate the effect of the presence of nonlocality upon the extinction. Far from the main resonance, Fig. (3.3a) shows us that we should expect the two models to produce similar results. This is indeed what we observe, however there is a slightly greater reduction in the extinction calculated with the local model, indicating that it is the effect of the control upon the TM modes present in both models, rather than the longitudinal mode, which dominates the observed response for this particle.

Similarly, by minimizing the amplitude of the dominant scattering mode, $\boldsymbol{s}_{10}$, we can introduce extremely sharp features in the scattering cross section in the direction orthogonal to both the pump and control. In Fig. (3.5), we utilize the same method of control on this mode at the peak of the main resonance in Fig. (3.3a) ($\omega/\omega_p = 0.578$) where we observe that the amplitudes of all three modes are reduced by several orders of magnitude, as their spatial coherence on the surface is very high near the resonance, shown in Fig. (3.5a). However, this high degree of spatial coherence results in a much sharper feature. By integrating the scattered energy over a cone in the far field, corresponding to the signal that would be detected by a wide angle detector with a numerical aperture NA ≈ 0.8, we observe a reduction of over six orders of magnitude in the light scattered, shown in Fig. (3.5b). Again we compare results for both the local and nonlocal models, where the control parameters employed were designed to minimize the

[3]Here, the vector operation is the standard inner product.

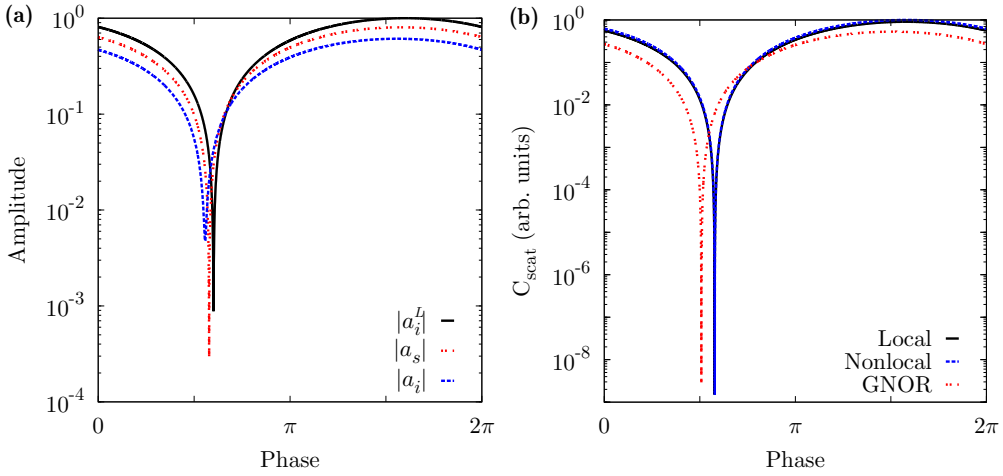

Figure 3.5: Same particle as in Fig. (3.3). Control on the $l = 1, m = 0$ transverse magnetic scattering mode at $\hbar\omega = 8.64$ eV where the spherical wave, $\boldsymbol{f}_2$, has an amplitude $|A_2| = 1$ and the external control wave, $\boldsymbol{f}_1$, has an amplitude $|A_1| = 1.04 \times 10^2$. (a) Minimization of the amplitude of the scattering mode via relative phase of radiation sources; the point where $|a_s| = 0$, to within numerical resolution, has been removed to avoid compressing the plot. As we are close to the main resonance in Fig. (3.3), we observe that the modes are well aligned. (b) We observe a sharp feature in the field scattered at $\pi/2$ with respect to both the pump and control beam, for a wide angle detector, with a half angle of 60 degrees. We include also the scattering due to control of the analogous mode for the local model with $|A_1| = 1.03 \times 10^2$. In this example the local and nonlocal traces are effectively indistinguishable. We include also results obtained using the generalized nonlocal optical response theory (GNOR) [166], which accounts for damping via nonlocal decay channels (see Sec. 3.2.3).

relevant scattering mode for each model. For scattering, the signals observed at the detector would be too similar to distinguish between the two models for this size of particle.

To further demonstrate the general applicability of the proposed coherent control method, we include in Fig. (3.5b) results obtained by applying the GNOR theory, see Sec. 3.2.3, which explains the damping and broadening of plasmon resonances via electron diffusion. This produces qualitatively similar results, as the control scheme works independently of the specific damping model employed. We remark that if the diffusion constant which appears in this model is instead treated as a free parameter, we observe that the amplitudes of the modes vary exponentially with τ_s (the relaxation time associated to scattering processes) while their phases barely shift and the suppression achieved through the control method remains unaffected.

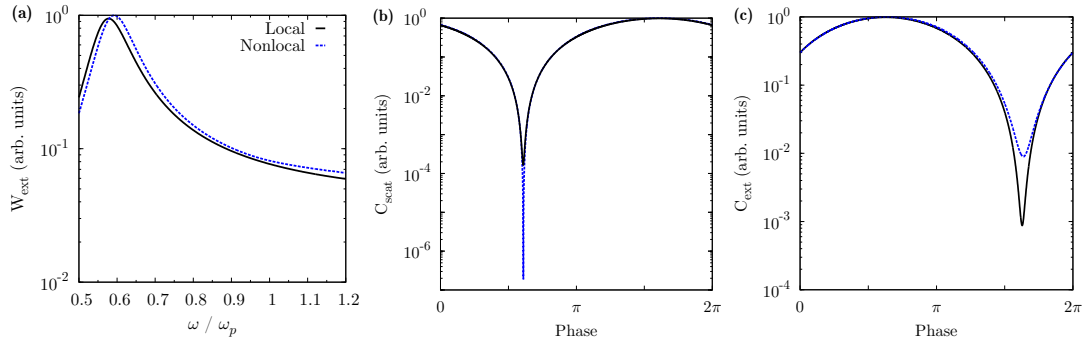

Figure 3.6: An aluminium sphere of radius 3 nm in vacuum. (a) Extinction power over 4π sterad. as a function of normalised frequency for a local and nonlocal response. (b) Control on the $l = 1, m = 0$ scattering mode for both the local and nonlocal model at $\hbar\omega = 8.64$ eV with $|A_1| = 4.98 \times 10^2$. We observe the field scattered at $\pi/2$ with respect to both the pump and control beam, for a wide angle detector, with a half angle of 60 degrees. (c) Control on the $l = 1, m = 0$ internal longitudinal mode at $\hbar\omega = 16.96$ eV, with $|A_1| = 1.42 \times 10^3$. The local trace shows the extinction calculated when the control parameters designed for the nonlocal model are applied to the local model.

To further investigate the differences between a local and nonlocal response to control, in Fig. (3.6) we consider a sphere of radius 3 nm for which the effects of nonlocality should be more pronounced. We employ the same method of control, for the same sets of modes as in the previous Figures. Figure (3.6b) shows that

the scattering for the local mode is not minimized as sharply as it is for the nonlocal mode for this particle. Although there are many orders of magnitude of difference between the minima of the two curves, it would be very challenging to utilize this result experimentally to detect nonlocal behaviour. Firstly, the signals would be very weak and may be difficult to detect and secondly, similar results could be expected to be observed if the amplitude of the control wave was reduced by *approx.* $10-20\%$, see Fig. (3.13). We note also that strong suppression of the modes can still be achieved for variations of the frequency of up to *approx.* 10%. However, the extinction signals differ by an order of magnitude at their minima, Fig. (3.6c), and would be easier to detect experimentally.

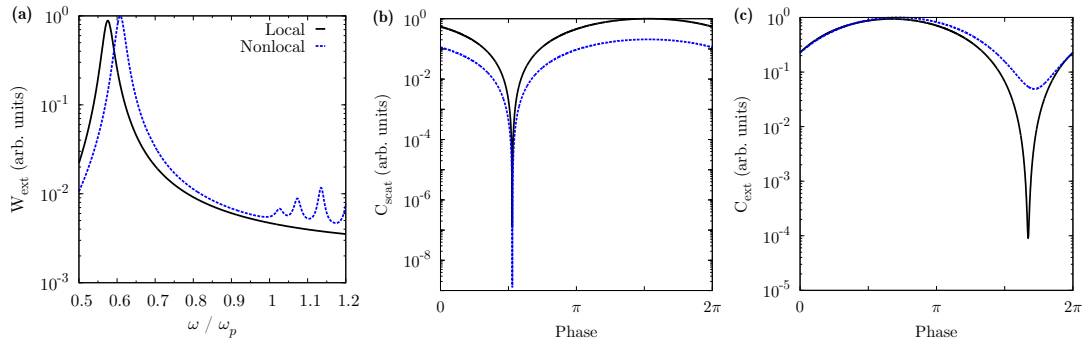

Figure 3.7: An aluminium sphere of radius 1.5 nm in vacuum. (a) Extinction power over 4π sterad. as a function of normalised frequency for a local and nonlocal response, showing additional resonances above the plasma frequency. (b) Control on the $l=1, m=0$ scattering mode for both the local and nonlocal model at $\hbar\omega = 8.64$ eV with $|A_1| = 4.03\times10^3$. We observe the field scattered at $\pi/2$ with respect to both the pump and control beam, for a wide angle detector, with a half angle of 60 degrees. (c) Control on the $l=1, m=0$ internal longitudinal mode at $\hbar\omega = 16.96$ eV, with $|A_1| = 1.24\times10^4$. The local trace shows the extinction calculated when the control parameters designed for the nonlocal model are applied to the local model.

Finally, in Fig. (3.7a) we compare the extinction power for an aluminium sphere of radius 1.5 nm exhibiting local and nonlocal response to excitation by plane wave. This Figure is analogous to Fig. 7(b1) in Ref. [161], where they show that additional resonances appear in the nonlocal spectrum above the plasma frequency, for particles of these dimensions. For illustrative purposes, we do not account for surface collisions (*cf* Eq. (3.13)) as the resulting broadening of the resonance hides these features. Again, we show that we are able to suppress

the scattering by minimizing the amplitude of the $\boldsymbol{s}_{10}$ mode near the main resonance, Fig. (3.7b). By controlling the longitudinal mode associated to the largest additional resonance above the plasma frequency ($\omega/\omega_p = 1.136$) we observe a much sharper feature in the extinction for this size of particle, Fig. (3.7c), where there is a clear difference between the local and nonlocal responses. Therefore, in principle we could use control techniques to identify the effect of nonlocality.

3.4 Inelastic scattering: Multiphoton processes

3.4.1 Control of nonlinear multiphoton processes

Coherent control of second-harmonic generation using an extra pump beam has been recently demonstrated numerically in particles with cylindrical symmetry [42]. For spheres, it was shown in Ref. [173] that the directionality of the emission obtained from combining two pump beams results from selection rules that depend on the order of the specific process and on the size of the particles. In this Section, we instead suggest, a scheme for the coherent control of internal and external multipolar waves in nanospheres which applies independently of the specific multiphoton processes at the origin of the multipolar waves. We make the assumption that losses in the pump field due to the conversion of photons at the harmonic frequency are negligible compared to all other linear processes which occur at the fundamental frequency, hence the nonlinear response is weak and may be treated using a linear theory. This means that we do not strictly maintain energy conservation, however for very small numbers of photon conversions the effect is negligible, and does not reduce the validity of the calculations. If we instead wish to consider a regime in which a large number of photons are converted then a full system of nonlinear equations would have to be solved to properly describe the response. We derive analytically the principles of operation and show that they do not depend on the origin of the response of the particles, and are based only on experimentally measurable quantities.

The basic idea is to use the same pump to drive two similar nonlinear processes, using the output of one of them to control the other, as shown schemati-

cally in Fig. (3.8).

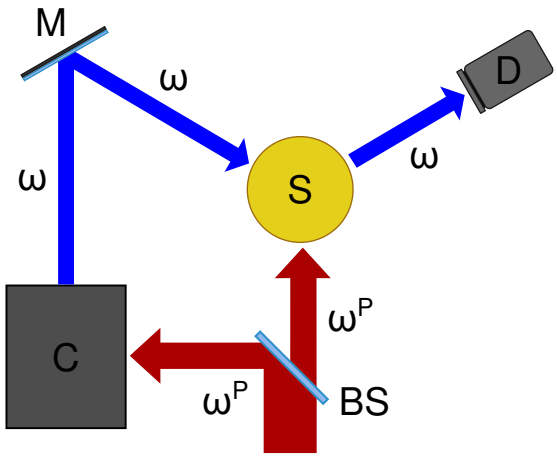

Figure 3.8: Schematic set-up (not to scale) for the implementation of the control scheme proposed for the control of nonlinear processes. The pump beam at frequency ω^P is divided by a beam splitter (BS) into two beams that drive equivalent nonlinear processes. Light at frequency ω is collected from the control generator (C) and directed to the nanosphere (S) along a direction where the controlled multipole has a maximum. The process is monitored by a detector (D) that collects light from a solid angle centred on a direction of maximal multipolar emission with no direct illumination from the control beam. The three parameters to be changed to control the output from the sphere are direction of incidence, power and relative phase of the control beam.

As we will see in the following, the identity of the two processes makes the scheme independent of the specific processes themselves. Furthermore, this scheme has the advantage of allowing separate control of internal losses and scattering, enabling the particle to interact with light as a perfect scatterer or as a perfect absorber. As we discussed previously, for spherical particles this can be done using combinations of electromagnetic waves generated inside and outside the particle, but is impossible using combinations of waves generated only outside the sphere [51]. The control is extremely sensitive to phase variations and produces a reduction of the absorption and changes in the scattered energy of several orders of magnitude. These features enable applications such as detection of changes in the position of the particle far smaller than the particle itself, suppression of radiative losses, sensing of variations in the electric permittivity, ϵ, and magnetic permeability, μ, and optical switching [153].

We analyse nonlinear processes in which combinations of appropriate order of the pump field and the polarization at the frequency ω^P causes bulk and/or surface polarization at frequency ω. Physically, the nonlinear polarization at frequency ω acts as a source of waves at that same frequency. This, in turn, excites internal and scattering modes of the particle at frequency ω in order to satisfy the boundary conditions. The nonlinear polarization can be modelled using the hydrodynamical model, as described in Sec. (3.2.1), or alternatively by introducing bulk and surface tensors [174, 167].

The particular solution of Maxwell's equations in the internal medium corresponding to a nonlinear bulk polarization, $\boldsymbol{P}^B$, is

$$\boldsymbol{E}^B(x) = \int_V G^E(\omega; x, x') \cdot \boldsymbol{P}^B(x')\mathrm{d}x', \tag{3.16}$$

where G^E is the electric dyadic Green's function at frequency ω for the internal medium that, for the hydrodynamical model, includes also longitudinal terms [175]. For the particles most commonly used in experiments, however, nonlocality is important only at the surface [176] and we can approximate $\boldsymbol{E}^B(x)$ using the Green's function without longitudinal terms. We use this Green's function also when $\boldsymbol{P}^B$ is modelled by the products of tensors with the electric field and its derivatives and the linear response is local [177].

Surface nonlinearities, $\boldsymbol{P}^S$, are instead confined to very thin layers at the surface of the particle and in both models are represented by infinitesimal polarization sheets outside the bulk when the external medium allows interface charge, as in vacuum or air. The surface [171, 178] and volume nonlinearities then appear in the boundary conditions

$$\epsilon^i \boldsymbol{E}^i_\perp - \epsilon^e \boldsymbol{E}^s_\perp = -\epsilon^i \boldsymbol{E}^B_\perp + \epsilon^e \boldsymbol{E}^c_\perp - \nabla_\parallel \cdot \boldsymbol{P}^S, \tag{3.17}$$

$$\boldsymbol{E}^i_\parallel - \boldsymbol{E}^s_\parallel = -\boldsymbol{E}^B_\parallel + \boldsymbol{E}^c_\parallel - (\epsilon^e)^{-1}\nabla_\parallel \boldsymbol{P}^S_\perp, \tag{3.18}$$

$$\boldsymbol{H}^i_\parallel - \boldsymbol{H}^s_\parallel = -\boldsymbol{H}^B_\parallel + \boldsymbol{H}^c_\parallel + i\omega(\hat{\boldsymbol{n}} \times \boldsymbol{P}^S), \tag{3.19}$$

where the indices i, s, c stand for internal, scattered and external control fields, and $\boldsymbol{E}_\perp = \hat{\boldsymbol{n}}(\hat{\boldsymbol{n}} \cdot \boldsymbol{E})$ is the component of the electric field normal to the particle surface, $\boldsymbol{E}_\parallel = -\hat{\boldsymbol{n}} \times (\hat{\boldsymbol{n}} \times \boldsymbol{E})$ is the component of the electric field tangential to

the particle surface, and analogously for the other fields. We note that the use of the boundary condition on $\boldsymbol{E}_\perp$ is necessary due to the presence of longitudinal electric waves. The fields $\boldsymbol{E}^i$ and $\boldsymbol{E}^s$ are the combination of the particles modes (solutions of the homogeneous equations without nonlinear polarizations) that fulfil the boundary conditions. The modes' amplitudes depend upon the left-hand sides of Eqs. (3.17-3.19) which, for any $\boldsymbol{E}^B, \boldsymbol{H}^B$ and $\boldsymbol{P}^S$, enable us to find the form of $\boldsymbol{E}^c$, $\boldsymbol{H}^c$ necessary to control the interaction of light with the particle through the amplitudes of the internal and scattering modes, regardless of the nature of the underlining nonlinear processes.

Using the formalism of Eq. (3.12), we can write the surface vector functions for the external control field and the nonlinear sources that appear in the boundary conditions, Eqs. (3.17-3.19) as

$$\boldsymbol{f}^c = \quad [\epsilon^e \boldsymbol{E}^c_\perp, \boldsymbol{E}^c_\parallel, \boldsymbol{H}^c_\parallel]^{\mathrm{T}}, \tag{3.20}$$

$$\boldsymbol{f}^{NL} = -\,[\epsilon^i \boldsymbol{E}^B_\perp + \nabla_\parallel \cdot \boldsymbol{P}^S, \boldsymbol{E}^B_\parallel + (\epsilon^e)^{-1}\nabla_\parallel \boldsymbol{P}^S{}_\perp, \boldsymbol{H}^B_\parallel - i\omega\hat{\boldsymbol{n}} \times \boldsymbol{P}^S]^{\mathrm{T}}. \tag{3.21}$$

Here we include the component $\epsilon\boldsymbol{E}_\perp$ in the surface vector functions in order to take into account all the boundary conditions. As before, the real amplitude and phase of $\boldsymbol{f}^c$ are encoded in the complex amplitude a^c. For any pair of internal and scattering modes, $\boldsymbol{i}_{lm}$, $\boldsymbol{s}_{lm}$, for which we adopt the same notation as for $\boldsymbol{f}^c$, the amplitudes a^i_{lm}, a^s_{lm} are given by

$$\begin{bmatrix} a^i_{lm} \\ -a^s_{lm} \end{bmatrix} = \begin{bmatrix} \boldsymbol{i}'_{lm} \cdot \boldsymbol{f}^c & \boldsymbol{i}'_{lm} \cdot \boldsymbol{f}^{NL} \\ \boldsymbol{s}'_{lm} \cdot \boldsymbol{f}^c & \boldsymbol{s}'_{lm} \cdot \boldsymbol{f}^{NL} \end{bmatrix} \begin{bmatrix} A^c \\ A^{NL} \end{bmatrix}, \tag{3.22}$$

where the amplitude of the nonlinear wave is related to the amplitude of the pump as $A^{NL} = (A^P)^N$, with N the order of the nonlinear process. To clarify, we note that for $\boldsymbol{f}^{NL} = 0$, *i.e.* in the absence of nonlinear processes, and $\boldsymbol{f}^c \neq 0$, Eq. (3.22) is a mathematically compact and efficient formulation of the Mie theory, in which the source of internal and scattering modes is the incident field at the surface of the sphere, $\boldsymbol{f}^c$. The amplitudes of the modes are determined by the boundary conditions and the material properties at frequency ω are fully included in the structure of the modes. The nonlinear polarizations $\boldsymbol{P}^B$ and $\boldsymbol{P}^S$ act as external sources that excite internal and scattering modes: When $\boldsymbol{f}^c = 0$

and $\boldsymbol{f}^{NL} \neq 0$, the nonlinear polarizations $\boldsymbol{P}^B$ and $\boldsymbol{P}^S$ act as external sources and excite internal and scattering modes: Eq. (3.22) gives us the amplitudes of these modes from the boundary conditions at frequency ω, generalizing an approach pioneered in Ref. [169] for Raman and fluorescence processes due to molecules embedded in dielectric particles. When $\boldsymbol{f}^c$ and $\boldsymbol{f}^{NL}$ are both non-null and coherent, Eq. (3.22) gives the amplitudes of the modes, which in this case are originated by the interference of $\boldsymbol{f}^c$ and $\boldsymbol{f}^{NL}$ at the surface of the particle.

We point out that the theory we described explains the principles of the coherent control that we propose, but no *a priori* theoretical knowledge is necessary to implement such control. From an operational point of view, it is only necessary to determine experimentally the multipolar fields excited by the nonlinear sources; once these are known, the control field $\boldsymbol{E}^c, \boldsymbol{H}^c$ is chosen considering the multipolar terms one wants to control and the desired mode amplitudes are found by adjusting the amplitude and phase of the control field via Eq. (3.22).

3.4.2 Second harmonic generation in gold nanospheres

Within the electric dipole approximation, second order nonlinear processes are forbidden in centrosymmetric materials [179], such as gold. However, nonlinear surface polarizations arise when the inversion symmetry is broken at the particle boundary [180, 177]. Higher order multipole interactions give rise to nonlinear polarizations also inside the bulk [174]. In second harmonic generation [181], two photons at the fundamental frequency ω^P are converted to a single photon at the harmonic frequency $\omega = 2\omega^P$, which is also the frequency of the external control beam $\boldsymbol{f}^c$.

To demonstrate the effect of this nonlinear control technique, we consider a gold nanosphere of 50 nm radius, using plane waves for the pump and the control beam: we keep the pump constant, and vary the amplitude and phase of the control. We again use a Lorentz-Drude model for the dielectric function [182] and neglect the effects of surface collisions, which are negligible for particles these dimensions. Second harmonic signals from individual spherical gold particles of similar dimension have been studied experimentally [183], where their polariza-

tion dependence was obtained.

For particles of this size, bulk nonlinearities are also negligible [177, 174] and the nonlinear polarization sheet is dominated by the radial component which excites an electric dipole with $l = 1$,$m = 0$ and electric quadrupoles with $l = 2$,$m = 0$ and $l = 2$,$m = \pm 2$. We employ a simplified analysis of the surface nonlinear response, where the second order susceptibility tensor is reduced to a single component corresponding to fields normal to the surface of the particle. Hence, for the following calculations we assume a local response with nonlinear polarization,

$$\boldsymbol{P}_{\perp}^{S} = \epsilon_0 \chi_{\perp\perp\perp}^{(2)} \boldsymbol{E}_{\perp}^{i} \boldsymbol{E}_{\perp}^{i}, \tag{3.23}$$

where ϵ_0 is the vacuum permittivity and the second-order susceptibility tensor component $\chi_{\perp\perp\perp}^{(2)} = 47.6$ in units of 3.27×10^{-17} m/V [174]. This value was measured from thin films, and does not account for the size or curvature of the particle. Experiments have shown that both the measured nonlinear signal [184], and susceptibilities [185], show a strong size dependence for noble metal nanoparticles. The Rudnick and Stern model provides a method for defining the susceptibility tensor via a set of adimensional parameters [186], which model the nonlinearity best when these parameters are fitted phenomenologically [177]. However, this fitting depends strongly on the specific experimental configuration and so we use the thin film value here simply to provide a qualitative description of the nonlinear response, such that the effects of the coherent control scheme may be demonstrated. The amplitudes of the multipoles generated by the nonlinear polarization and of the control beams are of the same order and scale linearly with $\chi_{\perp\perp\perp}^{(2)}$. Both the hydrodynamical and surface tensor models for nonlinear polarizations have been tested and give qualitatively similar results but with some quantitative differences. We have verified our control theory on all models.

We use a perturbative approach, assuming that losses due to photon conversion are negligible. Here, the amplitude of the pump is set to unity, $A^P = 1$, and, consequently, so too is the amplitude of the nonlinear control wave A^{NL} which appears in Eq. (3.22).

To describe effects that are most easily observed experimentally, we concen-

trate here on the control of two modes, where suppression of their amplitudes leads to perfect absorption and perfect scattering (for the particular l,m channel). We remark that while the sphere can behave as a perfect scatterer or a perfect absorber, the mechanism described here is significantly different from coherent perfect absorption [40]. This is a resonant process which can be understood as the time reversal of lasing and happens for particular values of the dissipation, when there are interference patterns inside the system able to trap a specific incoming mode indefinitely. We show instead that any spherical multipolar wave can be either trapped inside or expelled from the particle by the interference pattern formed by the appropriate combination of an incident wave with the surface polarization and the internal wave induced by the nonlinear process. This happens for any value of the dissipation, but for particular values of the amplitude of the control wave. Narrow resonant features can be observed in the response of the controlled particle when the material parameters or the frequency are changed while the control amplitudes are kept constant, as a result of the dependence of the modes upon the parameters that are changed. The values of frequency, or material parameters, at which these narrow features reach minima or maxima can be changed by changing the control amplitudes. This allows us to engineer particle responses with high sensitivity to changes in the external parameters.

In Fig. (3.9) we control the ratio of the internal and scattering modes $\boldsymbol{i}_{10}$ and $\boldsymbol{s}_{10}$ of the electric dipole. In Fig. (3.9a) the amplitude of the control beam is chosen so that the amplitude of $\boldsymbol{s}_{10}$, a^s_{10}, can vanish at the appropriate phase. The control results in an extremely sharp variation of the field scattered in a direction orthogonal to both the pump and control beams, which depends upon the relative phase between the external control beam and the nonlinear wave. No other multipoles emit along this direction and so the intensity has the same dependence on a^s_{10}, hence the sharpness of the feature. The light scattered in a solid angle centred on this direction can be monitored in an experiment to optimise the control beam; note that the phase sensitivity shown in Fig. (3.9a) allows us to map the position of the particle with a resolution $\Delta\lambda/\lambda = \Delta\Phi/\ 2\pi$, where λ is the wavelength of the control beam, and Φ is the relative phase between

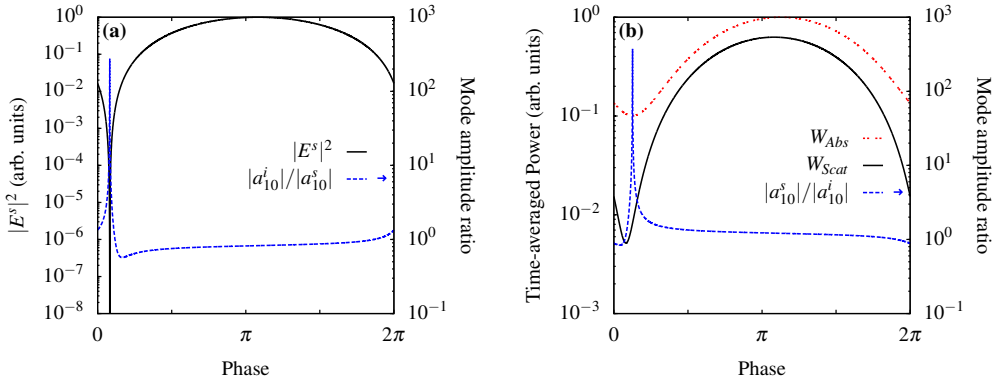

Figure 3.9: Nonlinear control of gold spheres of radius 50 nm. Scattered field intensity along a direction orthogonal to both pump and control beams and mode amplitudes against relative phase of control beam. In this Figure and in the following ones, we used a pump amplitude $A^P = 1$ in arbitrary units with $\omega^P = 281.76$ THz. In all plots, arrows in the key indicate when values should be read from the secondary axis. (a) Control at $\pi/2$ with respect to the pump, on $l = 1$, $m = 0$ internal and scattering modes, at frequency $\omega = 563.52$ THz with control beam amplitude $|A^c| = 1.47 \times 10^{-12}$ in arbitrary units to find perfect absorption on the controlled modes. (b) Time-averaged power calculated over 4π sterad. $|A^c| = 1.28 \times 10^{-12}$ to find perfect scattering on the controlled modes.

the external and nonlinear control waves. This provides a deeply sub-wavelength spatial resolution when no other multipole radiates in the solid angle of detection and the sensitivity of the detector allows one to monitor the logarithm of the signal. The optimal solid angle can be found by considering the known radiation patterns of the multipoles [78].

Fig. (3.10) shows the radiation patterns in the equatorial plane, $\theta = 90°$, of the sphere with and without control, where the electric field of the (linearly polarized) control beam is orthogonal to this plane. With the control set to suppress the dominant dipolar mode $\boldsymbol{s}_{10}$, only the $\boldsymbol{s}_{2\pm2}$ quadrupole modes radiate in this plane. Interference between these two higher order modes produces the quadrupolar pattern observed (solid-red curve), and also accounts for the slight quadrupole nature of the radiation pattern without the control beam (dashed-blue curve).

We can also vary the ratio between scattered intensity and absorbed energy for the electric dipole, Fig. (3.9b). By removing the dominant internal mode, we can minimize the total absorption, which is very useful to reduce heating and, as

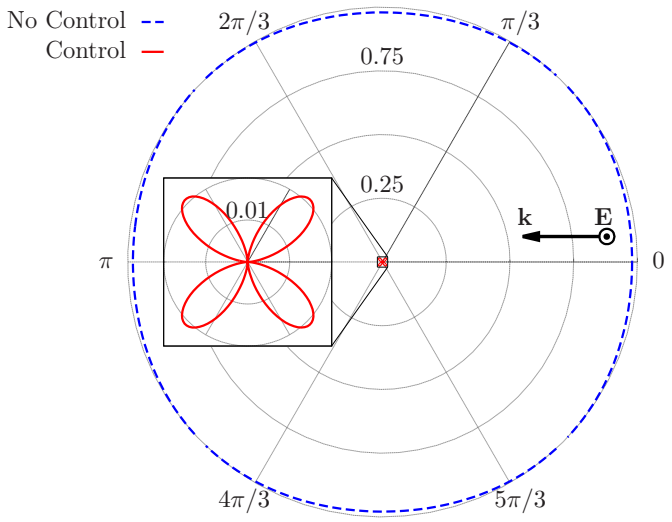

Figure 3.10: Same particle and frequency as Fig. (3.9). Control on $\boldsymbol{s}_{10}$, same as Fig. (3.9a). Radiation pattern along the equatorial plane of the sphere, at $\theta = 90°$, with and without control. Inset shows an enlargement of the $\boldsymbol{s}_{2\pm2}$ quadrupoles. The arrows indicate the direction of the wave vector $\boldsymbol{k}$, and linearly polarized electric field $\boldsymbol{E}$, of the external control beam.

a consequence, increase stability in experiments.

In Fig. (3.11a), we control the intensity of the field scattered in a direction at $\pi/2$ with respect to the control beam, and at $\pi/4$ with respect to the pump, by changing the amplitudes of the modes of the electric quadrupole with $l = 2, m = \pm 2$, as shown in Fig. (3.11b), where the plane wave couples to both of the $l = 2$ modes. Even in this case, we can observe a subwavelength variation of the intensity. By using an incoming (converging) multipolar wave with $l = 2$, $m = 2$ as the control, we can reduce the scattering in the same direction, Fig. (3.12a). Note that in this case the variation of the intensity is less than in Fig. (3.11a) because the multipolar control wave affects only the $l = 2$, $m = 2$ mode, as can be seen from Fig. (3.12b). We need two control beams to control independently the modes $l = 2$,$m = 2$ and $l = 2$,$m = -2$ in order to improve on the result shown in Fig. (3.11a), but Fig. (3.12a) shows that using incoming multipolar waves is not necessarily more effective than using plane waves.

Finally, in Fig. (3.13) we show how the sensitivity to phase variation can be applied to monitor small variations in the dielectric permittivity of the host medium; similar results could be achieved with variations of the magnetic perme-

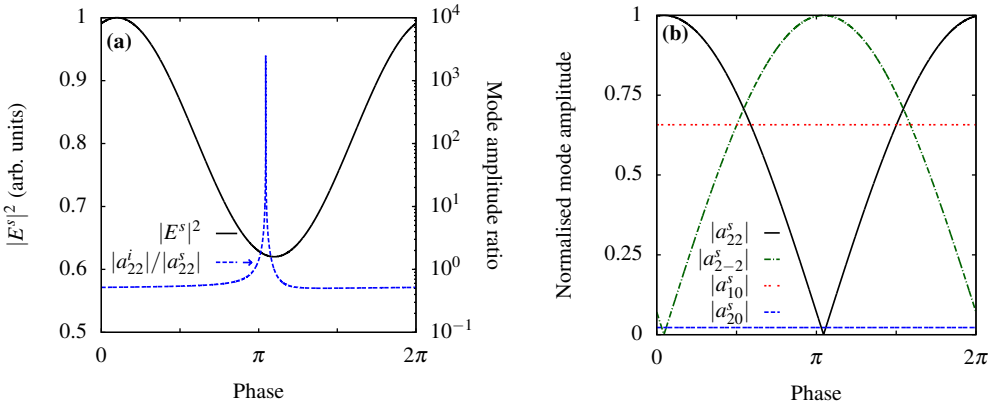

Figure 3.11: Same particle and frequency as Fig. 3.9. (a) Control at $\pi/4$ with respect to the pump, on the $l = 2$, $m = \pm 2$ quadrupole scattering modes, with $|A^c| = 1.32 \times 10^{-11}$ to find perfect absorption on the $l = 2$, $m = 2$ channel. (b) Amplitudes of the modes excited, showing that the control beam affects only the $l = 2$,$m = \pm 2$ modes.

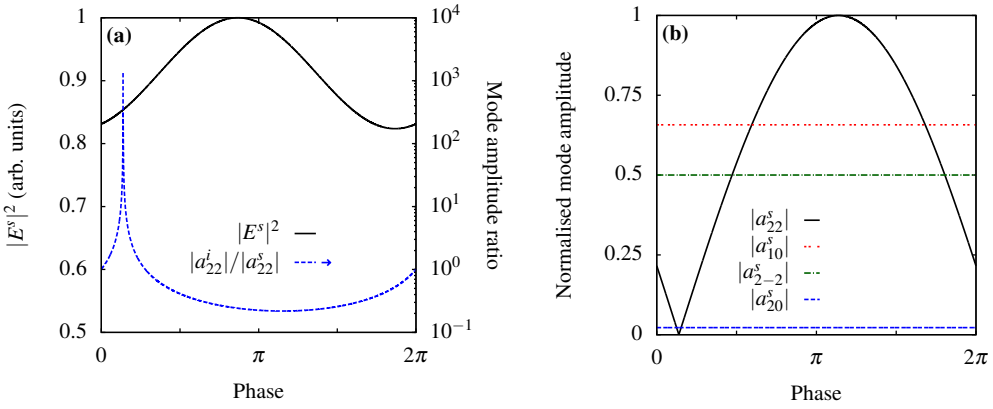

Figure 3.12: Same particle and frequency as Fig. 3.9. (a) Same scattering direction as in Fig. 3.11a, but with an incoming multipolar $l = 2$,$m = 2$ wave as the control. (b) Only the amplitude of the $l = 2$,$m = 2$ scattering mode is affected. The smaller variation in the scattered intensity is due to the fact that this control beam has no effect on the $l = 2$,$m = -2$ mode.

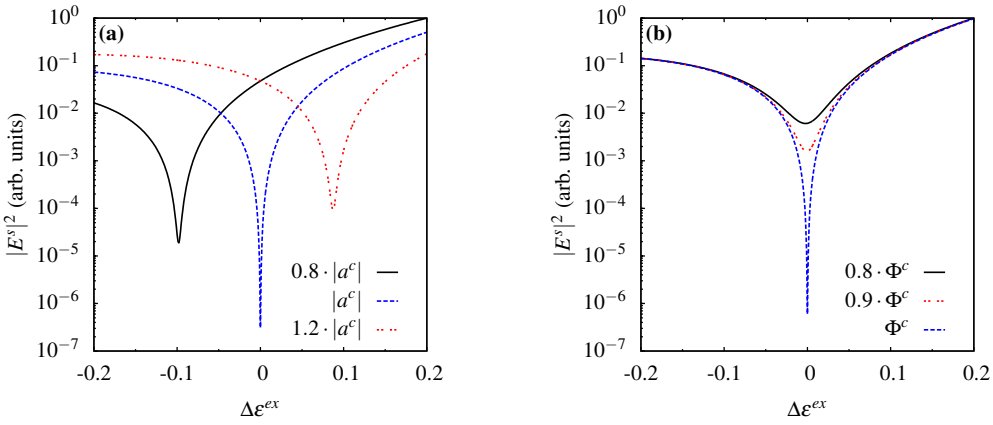

Figure 3.13: Same particle and frequency as Fig. (3.9). The intensity and phase of the pump and control beam are optimized to suppress the $\boldsymbol{s}_{10}$ mode at $\Delta\epsilon^e = 0$, as in Fig. (3.9a). The directional scattered intensity is extremely sensitive to small changes in the external dielectric permittivity (blue-dashed curve). This effect enables the measurement of the local environment. (a) When $|A^c|$ is changed by $\pm 20\%$, as the control is no longer optimized at $\Delta\epsilon^e = 0$, the curve of the scattered intensity drifts (black-solid/red-dotted curves) but we still observe sharp features. (b) The sharpness of the feature in the scattering intensity reduces significantly when the relative phase of the control beam, Φ^c, is changed from the optimized value by 10% (red-dotted curve) or 20% (black-solid curve).

ability. With the intensity and phase of the pump and control beams optimized to suppress the $\boldsymbol{s}_{10}$ mode for a particular environment, $\epsilon^e(\Delta\epsilon^e = 0), \mu^e$, we observe a strong sensitivity to small changes in ϵ^e in the scattered intensity. As the modes of the system depend upon the local environment, the relative phase and amplitude of the control beam required to maintain suppression of the modes change with it. When we vary the optimized amplitude of the control field by $\pm 20\%$ we observe that the curve of the scattered intensity drifts, so that the minima no longer occurs at $\Delta\epsilon^e = 0$, and the sensitivity decreases slightly. The conditions for suppression are much more sensitive to changes in the relative phase, with the control amplitude kept constant, we see a significant change in the sharpness of the scattering feature as the phase is varied.

3.5 Summary

In this Chapter, we have presented schemes for the coherent control of light and currents in metallic nanospheres, identifying extreme sensitivity to variations of the relative phase of two coherent incident waves that can lead to novel applications. These include the suppression of radiative losses, sensing of variations in the electromagnetic properties of the host medium, optical routing and detection of changes in the position of the particle far smaller than the particle itself. We note that when using light to control currents, the variation in absorption can be used to reduce dissipation, enhance the detection of nonlinear processes and lower amplification thresholds.

The theory we have presented can be easily generalized to particles with other shapes: in most cases the Mie approach based on separation of variables does not apply, but the principal mode theory can be utilized and leads to the same type of equations used to design control schemes. The control of a larger number N of modes is in principle straightforward and requires to adjust the amplitudes of the pump and of $N - 1$ control beams. From a practical point of view, spatial light modulators and configurable array mirrors could provide an effective way to implement control schemes for several modes, providing an efficient and adaptable

coupling to a high number of modes with a low number of beams, each with a complex profile made up by the superposition of several plane waves.

Chapter 4

Classical Green's functions and quantum phenomena

In a quantum theory of emitter and light, the variables of the classical Maxwell's equations that describe the coupling between electromagnetic fields and matter become operators, but the structure of the equations remains unchanged. As a result, classical dyadic Green's functions—which provide the electric and magnetic fields emitted by classic dipoles—also play an essential role in quantum optics. In this context, the Green's functions connect quantum fluctuations in polarization and magnetization to the electromagnetic field [187, 188, 189, 190].

The ability to calculate Green's functions is therefore essential to predict and design nanostructures and metamaterials with the properties we desire. Obtaining Green's functions via numerical solutions of volume integral equations or finite-difference time-domain calculations [145] is computationally very intensive and provides only limited insight into the properties of photonic systems, as only the resulting field is obtained without a clear indication of the nature of the main contributions underlying the response. Instead, decompositions of the Green's functions into modes of the electromagnetic fields gives efficient approximation schemes that combine good calculation speed with the ability to provide greater physical insight, but have been limited so far to single particles with a few simple geometries [191], non-dissipating systems [192], very small particles in the quasi-static approximation [193] and simple open systems described by a small set of

quasi-modes [194].

In this Chapter, we present a completely different approach, deriving analytical formulae for the Green's functions of a collection of disjoint particles in a host medium, with both particles and host medium being possibly inhomogeneous. These formulae rely on surface operators that include multiple scattering to all orders, even in the presence of strong absorption. For particles without sharp edges, these operators can be decomposed in terms of multi-particle electromagnetic surface modes and do not need an ad-hoc definition of mode volumes, or volume integration [194, 195].

4.1 Optical interactions

Nanostructures can induce large variations in many fundamental quantum phenomena such as the rate of spontaneous emission [196, 197], the photonic Lamb shift of resonance frequencies and Casimir-Polder forces [198]. This approach allows us to find the dependence of these quantities on the geometry and the material composition of the nanostructures, and in Sec. 4.2 we will show that their main features are determined by the interference of very few modes. Calculating Green's functions by solving a surface problem is numerically very efficient and the multi-particle surface modes give an insight into the behaviour of the whole system as a function of frequency. Our approach can be applied to linear media in which responses to perturbations appear only after the perturbations themselves [199], *i.e.* in all physical linear media.

4.1.1 Green's functions for an inhomogeneous multi-particle system

We consider a system containing a collection of particles, which can be made of different materials, embedded inside a non-absorbing dielectric host medium and monochromatic light sources with frequency ω. In order to describe a system containing N disjoint particles we first need to define all of the relevant subspaces, and so we introduce the following notation: V_j, ∂V_j and $\overline{V}_j$ represent the internal

region, the surface, and the combined internal region and surface of the j^{th} particle respectively, where $j = 1, \ldots, N$. Additionally, we define the unbounded region external to every particle as V_0, and the boundary between the external region and all N particles, which is the union of all the particles' surfaces, as $\partial V_0 = \bigcup_{j=1}^{N} \partial V_j$. Finally, the entire space excluding the boundaries ∂V_0 is then defined as $V = \bigcup_{q=0}^{N} V_q$. A simple schematic is provided in Fig. (4.1) for clarification.

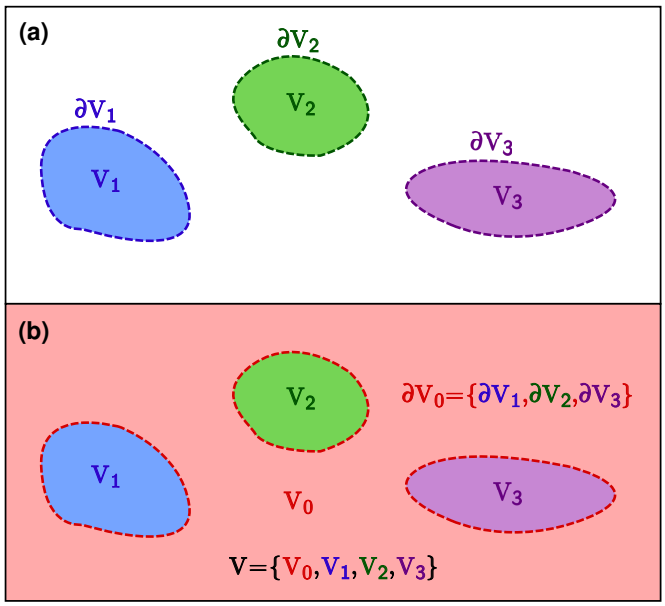

Figure 4.1: Simple schematic showing a system with $N = 3$ disjoint particles embedded in a host medium. (a) For each particle, j, with either/both ϵ^j, μ^j different from that of the host medium, we define the subspaces: V_j being the internal region of the particle; ∂V_j is the surface boundary of the particle; and $\overline{V}_j$ is the combined internal region and surface of the particle (the bounded volume). (b) The host medium V_0 is the region external to all particles, with boundaries defined as the set that contains all the particles' surfaces, $\partial V_0 = \bigcup_{j=1}^{N} \partial V_j$.

For an unbounded inhomogeneous medium, the electric and magnetic fields generated by a combination of a polarization $\boldsymbol{P}(\boldsymbol{r'})$ and a magnetization $\boldsymbol{M}(\boldsymbol{r'})$, are given by [164],

$$\begin{pmatrix} \boldsymbol{E}(\boldsymbol{r}) \\ \boldsymbol{H}(\boldsymbol{r}) \end{pmatrix} = \begin{pmatrix} G^{EP}(\omega; \boldsymbol{r}, \boldsymbol{r'}) & G^{EM}(\omega; \boldsymbol{r}, \boldsymbol{r'}) \\ G^{HP}(\omega; \boldsymbol{r}, \boldsymbol{r'}) & G^{HM}(\omega; \boldsymbol{r}, \boldsymbol{r'}) \end{pmatrix} \circ_V \begin{pmatrix} \boldsymbol{P}(\boldsymbol{r'}) \\ \mu_0 \mu_r \boldsymbol{M}(\boldsymbol{r'}) \end{pmatrix}. \tag{4.1}$$

Here, the notation $\circ_V$ indicates the scalar product integrated over the region V. $G(\omega; \boldsymbol{r}, \boldsymbol{r'})$ are the classical Green's functions, as defined in Appendix C, where

the first index, E (H), denotes the propagation of an electric (magnetic) field and the second index, P (M), indicates that this field was generated by an electric (magnetic) dipole source. Hence, $G^{HP} = \nabla \times G^{EP}$ and $G^{EM} = \nabla \times G^{HM}$. From Eq. (4.1), we can express the l^{th} component of the electric and magnetic fields generated by a single electric dipole, for an arbitrary orthonormal system of reference where $x = \{1, 2, 3\}$, as

$$\boldsymbol{E}_x^P(\boldsymbol{r}) = \sum_{x'=1}^{3} \int_V G_{xx'}^{EP}(\boldsymbol{r}, \boldsymbol{r'}) \cdot \boldsymbol{P}_{x'}(\boldsymbol{r'}) dV(\boldsymbol{r'}), \tag{4.2}$$

$$\boldsymbol{H}_x^P(\boldsymbol{r}) = \sum_{x'=1}^{3} \int_V G_{xx'}^{HP}(\boldsymbol{r}, \boldsymbol{r'}) \cdot \boldsymbol{P}_{x'}(\boldsymbol{r'}) dV(\boldsymbol{r'}). \tag{4.3}$$

Fields propagated by the magnetic Green's functions can be similarly defined for magnetic sources.

When both $\boldsymbol{r}$ and $\boldsymbol{r'}$ are located outside the nanoparticle(s) and above the substrate, the Green's function is given by the sum of two terms, $G = G_0 + G^S$. The first term, G_0, gives the sum of the field emitted by the dipole, which is known analytically, and the field reflected by the substrate, which is given by G^R (Eq. (C.25)). The main difficulties in evaluating the response comes from the second term, G^S, the scattering Green's function. In classical electromagnetism, this term is due to the secondary field of the dipole, emitted at an earlier time and scattered back to the position of the dipole from the environment. It therefore propagates the fields from the emitter to the environment, and then back to the position of the emitter via scattering surfaces (particles, cavity walls, waveguides *etc.*), taking into account multiple scattering between these surfaces and the substrate.

We introduce a more compact notation by defining six component (column) vectors for the electromagnetic fields, and also for the combination of electric and magnetic dipole sources respectively,

$$\boldsymbol{F}(\boldsymbol{r}) = \left[\boldsymbol{E}(\boldsymbol{r}), \boldsymbol{H}(\boldsymbol{r})\right]^{\mathrm{T}}, \tag{4.4}$$

$$\boldsymbol{D}(\boldsymbol{r'}) = \left[\boldsymbol{P}(\boldsymbol{r'}), \mu_0 \mu_r \boldsymbol{M}(\boldsymbol{r'})\right]^{\mathrm{T}}, \tag{4.5}$$

where T indicates transposition. In order to find the Green's function for a system of N particles, we need to add the fields directly radiated by sources and the fields

scattered by the surfaces. For any j, the fields emitted by the monochromatic sources, $\boldsymbol{D}$, located in the region V_j are given by,

$$\boldsymbol{F}^j(\boldsymbol{r}) = \mathcal{G}_j(\boldsymbol{r}, \boldsymbol{r'}) \circ_{V_j} \boldsymbol{D}(\boldsymbol{r'}). \tag{4.6}$$

In Eq. (4.6), $\mathcal{G}_j$ is equivalent to the tensor Green's function given in Eq. (4.1) for the medium in the j^{th} region when $\boldsymbol{r} \in \overline{V}_j$ and $\boldsymbol{r'} \in V_j$, and it is null otherwise. In other words, the fields radiated from sources inside the j^{th} region are defined everywhere, but are different from zero only inside this region and on its boundary. For any orthonormal system of coordinates, we can express the right-hand side of Eq. (4.6) as,

$$\mathcal{G}_j(\boldsymbol{r}, \boldsymbol{r'}) \circ_{V_j} \boldsymbol{D}(\boldsymbol{r'}) = \sum_{x'=1}^{6} \int_{V_j} \mathcal{G}_{j;xx'}(\boldsymbol{r}, \boldsymbol{r'}) \boldsymbol{D}_{x'}(\boldsymbol{r'}) dV(\boldsymbol{r'}). \tag{4.7}$$

As a result of discontinuities of the permittivity and permeability at the particles' surfaces and of multiple scattering, the incident field, $\boldsymbol{F}^j$, produces radiating waves outside all of the particles (the scattering field) and standing waves inside them (the internal field). The tangent components of these standing and radiating fields on the boundaries are found by solving the boundary conditions of Maxwell's equations. As the incident fields are defined everywhere, the boundary conditions for incident fields emitted from sources in any region are solved on the surfaces of all particles, ∂V_0, in the same way as boundary conditions are solved for single particle scattering [23]. We do this by building projectors that, given a field $\boldsymbol{F}^j$ at the boundary, project it into the internal and scattered fields that fulfil the boundary conditions.

As we described in Sec. 1.3, when each particle has a set of solutions of Maxwell's equations for the internal and external media, which are independent and complete on the surface of the particles, we can generalize the methods for a single particle and use principal modes to build these projectors for the multi-particle system. We consider the space $\mathcal{H}$ of the square integrable surface fields on ∂V_0. Fields generated by sources placed in V_0 and scattered fields are defined on $\mathcal{H}$, while fields internal to the j^{th} particle are defined only on ∂V_j. We extend the definition of these internal fields to ∂V_0 by setting their values on the

surfaces of the other particles equal to zero. In this way we can define a Hilbert space for all N particles that is the direct orthogonal sum of the Hilbert spaces of every particle, $\mathcal{H} = \mathcal{H}_1 \oplus \mathcal{H}_2 \oplus \ldots \oplus \mathcal{H}_N$. The scalar product between any pair of fields is defined in $\mathcal{H}$ by the same overlap integrals used for the scalar product in each single particle, but with the surface integration carried over all particles' surfaces, ∂V_0. Using the principal modes of each particle, we can define multi-particle principal modes and resonances as we have done before because the structure of the Gram operator remains unchanged.

We start from single particle principal internal and scattering modes, which are spatially correlated pairwise on the surface of the particle on which they are defined, as the Mie modes of a sphere. We then hybridize the single particle scattering modes forming multi-particle scattering modes, such that the overlap integral over all the particles' surfaces of any mode with the complex conjugate of another mode vanishes. In this way, multiple scattering effects are taken self-consistently into account at all orders. Finally, we rearrange these multi-particle modes forming internal and scattering multi-particle principal modes that are correlated pairwise on ∂V_0. We can then use these modes to create the multi-particle projectors $\bar{\Pi}^I$ and $\bar{\Pi}^S$.

The single particle projection operators are defined as,

$$\Pi^I(\boldsymbol{\sigma}, \boldsymbol{\sigma'}) = \sum_n \frac{\boldsymbol{i}_n(\boldsymbol{\sigma}) \bigotimes \boldsymbol{i}_n'^{\dagger}(\boldsymbol{\sigma'})}{\boldsymbol{i}_n' \cdot \boldsymbol{i}_n}, \qquad \Pi^S(\boldsymbol{\sigma}, \boldsymbol{\sigma'}) = -\sum_n \frac{\boldsymbol{s}_n(\boldsymbol{\sigma}) \bigotimes \boldsymbol{s}_n'^{\dagger}(\boldsymbol{\sigma'})}{\boldsymbol{s}_n' \cdot \boldsymbol{s}_n}. \tag{4.8}$$

The multiple particle projection operators are similarly defined by replacing the single particle modes with the multi-particle modes. For a single particle near a substrate the procedure is the same as for a single particle in a homogeneous host medium, but the surface fields also contain terms due to the substrate that are calculated through the substrate Green's functions [200]. In this way the multiple scattering between the particle and the substrate is calculated to all orders.

These projectors solve the boundary conditions providing the internal and scattered surface fields,

$$\boldsymbol{f}^{I/S}(\boldsymbol{\sigma}) = \bar{\Pi}^{I/S}(\boldsymbol{\sigma}, \boldsymbol{\sigma'}) \circ_{\partial V_0} c_j \boldsymbol{F}^j(\boldsymbol{\sigma'}) \tag{4.9}$$

where $c_q = 1$ for $q = 0$ and $c_q = -1$ for $q \neq 0$ (the sign is dependent upon whether a field is evaluated inside or outside the particles). Once the boundary conditions are solved, the Stratton-Chu representation theorem allows us to determine everywhere the value of the internal and scattering fields in terms of the values of their tangent components at the boundaries. This theorem is very general and applies to inhomogeneous media [164]: in the following we use it to give an explicit formula for the Green's functions of the N particle system.

By introducing the operator X that acts on the functions defined on the particles' surfaces, such that,

$$X\boldsymbol{F}(\boldsymbol{\sigma}) = \frac{i}{\omega}\left[-\hat{\boldsymbol{n}}(\boldsymbol{\sigma}) \times \boldsymbol{H}(\boldsymbol{\sigma}), \hat{\boldsymbol{n}}(\boldsymbol{\sigma}) \times \boldsymbol{E}(\boldsymbol{\sigma})\right]^{\mathrm{T}} \tag{4.10}$$

where $\boldsymbol{\sigma}$ is a point on the surface and $\hat{\boldsymbol{n}}(\boldsymbol{\sigma})$ is the outward unit vector normal to ∂V_0, the Stratton-Chu identities can be cast as,

$$\Theta_q(\boldsymbol{r})\boldsymbol{F}(\boldsymbol{r}) = -c_q \mathcal{G}_q(\boldsymbol{r}, \boldsymbol{\sigma}) \circ_{\partial V_0} X\boldsymbol{F}(\boldsymbol{\sigma}), \tag{4.11}$$

where $q = 1, \ldots, N$, the scalar function $\Theta_q(\boldsymbol{r}) = 1$ when $\boldsymbol{r} \in V_q$ and is zero otherwise, and $\boldsymbol{F}$ has no singularities in V_q. As before, we can express the term in the right-hand side of Eq. (4.11) as

$$\mathcal{G}_q(\boldsymbol{r}, \boldsymbol{\sigma}) \circ_{\partial V_0} X\boldsymbol{F}(\boldsymbol{\sigma}) = \sum_{x'=1}^{6} \int_{\partial V_0} \mathcal{G}_{q;xx'}(\boldsymbol{r}, \boldsymbol{\sigma}) \left[X\boldsymbol{F}(\boldsymbol{\sigma})\right]_{x'} d\boldsymbol{\sigma}. \tag{4.12}$$

From the definitions of X, one can see that $\hat{\boldsymbol{n}} \times \boldsymbol{E}$ acts as a magnetic surface current and $-\hat{\boldsymbol{n}} \times \boldsymbol{H}$ as an electric surface current in Eq. (4.11). In this way the boundary conditions for the tangent components of the fields on ∂V_0 can be written as $\boldsymbol{f}^I - \boldsymbol{f}^S = c_j \boldsymbol{f}^j$, with $\boldsymbol{f}^j = -\omega^2 X^2 \boldsymbol{F}^j(\boldsymbol{\sigma})$ the projection of the incident field $\boldsymbol{F}^j(\boldsymbol{\sigma})$, originated by a source in V_j, onto its components tangential to the surface. The internal and scattered field projections $\boldsymbol{f}^S$, $\boldsymbol{f}^I$, are defined analogously. These boundary conditions are formally the same as for a single particle [23].

Without loss of generality, in the following we consider the field point $\boldsymbol{r} \in \overline{V}_q$, where q can take any value between 0 and N. The scattering Green's function is found by applying the Stratton-Chu theorem, Eq. (4.11), to the tangent components of the standing or radiating fields, Eq. (4.9), generated by the sources in

every region, Eq. (4.6), and is given by,

$$\begin{aligned}\mathcal{G}_q^S(\boldsymbol{r},\boldsymbol{r'}) = -c_q\mathcal{G}_q(\boldsymbol{r},\boldsymbol{\sigma}) \quad &\circ_{\partial V_0} \quad X[(1-\delta_{0q})\bar{\Pi}^I(\boldsymbol{\sigma},\boldsymbol{\sigma'}) + \delta_{0q}\bar{\Pi}^S(\boldsymbol{\sigma},\boldsymbol{\sigma'})] \\ &\circ_{\partial V_0} \quad \sum_{j=0}^{N} c_j\mathcal{G}_j(\boldsymbol{\sigma'},\boldsymbol{r'}),\end{aligned} \tag{4.13}$$

where $\delta_{0q} = 1$ for $q = 0$, and $\delta_{0q} = 0$ for $q \neq 0$. Physically, $\mathcal{G}_j$ in the right-hand side of Eq. (4.13) propagates the fields from the sources in the j^{th} region to the boundary of this region, the projectors in the square brackets solve the boundary conditions providing internal and scattered fields on the boundaries, X transforms the surface fields into effective surface currents, and $\mathcal{G}_q$ propagates the fields from the boundary to the observation point in the q^{th} region.

Alternatively, and perhaps more instructively, for a single electric dipole radiating in the host medium, the scattering Green's function in Eq. (4.13) can be decomposed in terms of the principal scattering modes and their relative amplitudes[1],

$$G_0^{EP;S}(\boldsymbol{r},\boldsymbol{r'}) = \sum_n a_n^s(\mathbf{p}(\boldsymbol{r'}))\boldsymbol{s}_n^E(\boldsymbol{r'}) \tag{4.14}$$

where $\boldsymbol{s}_n^E(\boldsymbol{r})$ is the electric field of the n^{th} principal mode at the point $\boldsymbol{r}$, and $a_n^s(\mathbf{P}(\boldsymbol{r'}))$ is the amplitude of $\boldsymbol{s}_n^E$ due to the field generated by the dipole $\mathbf{p}$ in $\boldsymbol{r'}$. The amplitudes, $a_n^s(\mathbf{P}(\boldsymbol{r'}))$, are the product of two terms: one is the "sensitivity" of the mode, which is an intrinsic property of the particle that depends only on the spatial correlation between the scattering mode and its corresponding internal mode, at the surface of the particle; the other is proportional to the spatial correlation, at the surface of the particle, between the field generated by the dipole and the scattering and internal modes.

We find the total field in $\boldsymbol{r} \in V_q$ combining Eq. (4.6) with Eq. (4.13),

$$\boldsymbol{F}(\boldsymbol{r}) = [\mathcal{G}_q(\boldsymbol{r},\boldsymbol{r'}) + \mathcal{G}_q^S(\boldsymbol{r},\boldsymbol{r'})] \circ_V \boldsymbol{D}(\boldsymbol{r'}). \tag{4.15}$$

Eqs. (4.13,4.15) are exact and are the main theoretical result of this Chapter. Numerically, these equations are approximated by truncating the number of principal modes used in both the single and multi-particle projectors.

[1]For either single or multiple particles, depending on the nanostructures considered.

4.1.2 Quantum interactions of light and matter

We limit the following analysis to the case of two-level emitters (such as an atom, a simple molecule, or a quantum dot). For an electrically polarizable (neutral) emitter, located at the position $\boldsymbol{r'}$, the electric dipole approximation gives the following relation between the polarization and the dipole moment [199],

$$\boldsymbol{P}(\boldsymbol{r}) \equiv \boldsymbol{P}_A = \boldsymbol{p}\delta(\boldsymbol{r} - \boldsymbol{r'}) \tag{4.16}$$

with $\boldsymbol{P}_A$ the polarization of the emitter, and $\boldsymbol{p}$ the transition dipole moment.

The time-dependent coefficients of the quantum states of a two-level emitter and of the field are in general integro-differential equations with kernels dependent on the Greens functions we derived [199]. In general, these equations need to be integrated numerically, but there are two cases in which the integration can be done quite simply: weak and strong coupling.

In the weak coupling regime losses dominate the response of the system, where the decay is exponential, and the emission spectrum consists of a single peak, with a Lorentzian distribution and width proportional to the the modified decay rate, centred at the frequency of the resonant dressed transition of the emitter. The strong coupling regime instead is typically defined when interactions due to the (coherent) coupling in the system dominate over the (incoherent) losses, and the system dynamics are governed by energy exchange cycles between the modes of the nanostructure (or cavity) and emitter. As the coupling strength increases, and this regime is approached, the observed resonance peak in the emission spectrum splits, in a process known as Rabi splitting[2], due to Rabi oscillations between the ground and excited states of the two level emitter.

We note that the dependence of the Green's functions over the frequency and the dipole moment of the emitter considered are sufficient to determine whether one of these two regimes applies, or the equations have to be resolved numerically without approximations [199]. This means that it is not necessary to define a mode volume for the open systems considered here.

[2]In spectroscopy, this is sometimes referred to as Autler-Townes splitting, or the AC Stark effect.

In the following, we concentrate on the response of the nanostructures, *i.e.* on the Green's functions, which do not depend on the emitter. In the more common situation of weak coupling, when *memory effects* are negligible, the response of the emitter is proportional to the response of the nanostructure. This is analogous to the Markov approximation, used when deriving a master equation for weakly coupled quantum optical systems. This approximation can be applied when the characteristic relaxation time for the system is much longer than the correlation time of any coupled reservoir (or continuum), where the *memory* of previous interactions in the system is short-lived and the dynamic response can be determined over a significantly reduced time interval, proportional to the correlation time.

For weak coupling the decay rate of an electric dipolar emitter in the external host medium is,

$$\Gamma(\omega;\boldsymbol{P},\boldsymbol{r}) = \frac{2\omega^2}{\hbar\epsilon_0 c^2}\boldsymbol{P}^{\mathrm{T}}(\boldsymbol{r})\cdot\mathrm{Im}[G_0^{EP}(\omega;\boldsymbol{r},\boldsymbol{r}) + G_0^{EP;S}(\omega;\boldsymbol{r},\boldsymbol{r})]\cdot\boldsymbol{P}(\boldsymbol{r}), \qquad (4.17)$$

where $\hbar$ is the reduced Planck constant, and the field point and the position of the emitter coincide ($\boldsymbol{r} = \boldsymbol{r'}$). As we can see from Eq. (4.17), the decay rate is dependent upon both the proximity of the nanostructure, and the relative orientation of the dipole moment with respect to the nanostructure making it anisotropic. For an emitter in free-space, the Green's function G_0^{EP} reduces to the analytical homogeneous Green's function (given in Eq. (C.15)), and the decay rate can be found from the imaginary part of the function when evaluated at its origin: $\mathrm{Im}[G_0^{EP}] = \omega/(6\pi c)\mathbb{I}$, (see Eq. (C.16)),

$$\Gamma_0(\omega;\boldsymbol{P},\boldsymbol{r}) = \frac{\omega^3|\boldsymbol{P}(\boldsymbol{r})|^2}{3\hbar\pi\epsilon_0 c^3}. \qquad (4.18)$$

By normalizing the inhomogeneous decay rate by the free-space expression, we can define the enhancement of the decay rate due the presence of the nanostructure, which is known as the Purcell factor [201],

$$\frac{\Gamma}{\Gamma_0} = 1 + \frac{6\pi c}{\omega|\boldsymbol{P}(\boldsymbol{r})|^2}\boldsymbol{P}^{\mathrm{T}}(\boldsymbol{r})\cdot\mathrm{Im}[G_0^{EP;S}(\omega;\boldsymbol{r},\boldsymbol{r})]\cdot\boldsymbol{P}(\boldsymbol{r}). \qquad (4.19)$$

The quality factors (Q-factors) for resonances of the Purcell factor can be calculated as ω_c/κ, with ω_c the central frequency of the resonance line and κ the spectral width, at full width half maximum (FWHM).

The far field radiative rates are found using the dyadic Green's function and the relation $\Gamma/\Gamma_0 = P/P_0$, where P is the total power emitted by the dipole in the presence of the nanostructure and P_0 is the total power emitted by the dipole in vacuum [202]. The conservation of energy gives $P = P_r + P_{abs}$, where P_{abs} is the energy absorbed by the metallic nanostructure and P_r is the energy radiated (in the upper half-space for an absorbing substrate), which is evaluated by integrating the far field asymptotic form of the modulus squared of the electric field, given by the Green's function.

Using the relation between Γ and P, and Eq. (4.14), we can see that Γ_r is due to the coupling of the emitter with the principal modes that efficiently transport energy in the far field, a property which can be easily identified from their asymptotic far field expressions [23]. We can then calculate the radiative enhancement as $\Gamma_r/\Gamma_0 = P_r/P_0$. The optimal conditions for enhancing far field detection of fluorescence are thus provided by structures in which one radiative mode is resonant and strongly coupled with the emitter, as we see in the following Section.

For an emitter in vacuum, the frequency observed is not the true transition frequency as vacuum fluctuations interact with the emitter causing a shift, called the Lamb shift [203, 204]. A similar effect is observed in the presence of nanostructures, where the resonant part of the frequency shift is,

$$\delta\omega_1(\boldsymbol{P}, \boldsymbol{r}) = -\frac{\omega^2}{\hbar\epsilon_0 c^2}\boldsymbol{P}^{\mathrm{T}}(x) \cdot \mathrm{Re}[G_0^{EP,R}(\omega; \boldsymbol{r}, \boldsymbol{r}) + G_0^{EP;S}(\omega; \boldsymbol{r}, \boldsymbol{r})] \cdot \boldsymbol{P}(\boldsymbol{r}), \quad (4.20)$$

where $G_0^{EP,R}$ is the part of G_0^{EP} due to discontinuities in V_0, if they are present, and is null when V_0 is continuous. Here $\omega = \omega_{21} + \delta\omega_1 + \delta\omega_2$, where ω_{21} is the frequency of the dipole transition and $\delta\omega_2$ is the non-resonant shift, with $\delta\omega_2 << \delta\omega_1$ in most cases.

At the origin of these effects are significant modifications of the local density of light states (LDOS) that can be experimentally measured either optically [91] or with electron energy loss spectroscopy [205, 206]. The projected local density of states for an electric dipole in vacuum is [207, 208],

$$\rho_j(\omega; \boldsymbol{r}) = \frac{\omega}{\pi c^2}\mathrm{Im}[G_{jj}^{EP}(\omega; \boldsymbol{r}, \boldsymbol{r})]. \quad (4.21)$$

A larger density of states therefore is associated to a higher decay rate, or a shorter lifetime for the excited states.

4.2 Enhancing fluorescence from the visible to ultraviolet

In this Section, we calculate photonic Lamb shifts, Q-factors and the Purcell factors—the ratios of the decay rates in the nanostructures to the corresponding decay rates in vacuum—around aluminium nanostructures from the visible to the deep ultra-violet, determining the detection rate and the enhancement of the signal due to the nanostructures. These effects have been extensively investigated with noble metal nanoparticles [59, 60] in the visible range. Observing these effects in the ultraviolet is not trivial because the electromagnetic response of most materials depends strongly on the frequency of light, so experimental setups effective in one part of the electromagnetic spectrum cannot be directly reproduced in another.

A metallic nanostructure can significantly enhance the detection of fluorescence by emitters in which the emission rate is much less than the internal non-radiative decay rate [209], if it enhances the far field radiation rate of the emitter. This happens when the emitter is strongly coupled to electromagnetic modes that efficiently transport energy in the far field, but not when the emitter is coupled mainly to surface modes that are confined close to the metallic nanostructure. Here we consider how metal nanoparticles and substrates can enhance, by orders of magnitude, the detection of many important molecules that have radiative decays in the ultraviolet much weaker than non-radiative decays. Examples of such molecules are alkanes [210], most amino acids [211] in proteins and peptides, and DNA bases. However, we do not explicitly include non-radiative decays, which depend on the nature of the specific emitter.

In the following we consider nanorods and nanospheres and planar substrates, with the particles held in place by a dielectric tip, with gaps between the components in the range of $5-20$ nm so nonlocal effects [212] and quantum spill-out

can be neglected [213]. We assume that the dipole emitter is held in place in the middle of the gap between the substrate and/or the nanoparticle(s) by a dielectric spacer – not shown – which inhibits charge transfer between the emitter and the substrate. A small patch of SiO_2 would be a suitable spacer for most wavelengths considered here, but other solutions have been used, for example: a layer of macrocyclic molecules, such as the cucurbiturils, which have a ring structure and can *host* individual emitters [60], or monolayers of CdSe nanoplatelets, where appropriate photoinduced transformations can form a protective CdO top layer which prevents further oxidation of the spacer [214].

All of the nanostructures we consider have rotational symmetry about the $\hat{z}$-axis (defined by the long axis of the nanorods, and the normal to the substrate), and so we can decompose the electromagnetic response according to channels in which the modes transform similarly for rotations about $\hat{z}$ (according to the angular index m). At the wavelengths we consider, only the modes with $m = 0$ display resonances and so dominate the response. From a practical point of view, note that tilts of the axis of the nanorod break the rotational symmetry and induce mixing among modes with different azimuthal index, *i.e.* modes that transform differently under rotation. However, these effects are weak and can be neglected for nanorods with the width we consider and for tilting angles of a few degrees. Modes with higher azimuthal index may affect also the response of particles that are not perfectly spherical; however, these modes do not have strong resonances in the range of wavelengths considered, and so these effects are also weak. As long as the dielectric tip does not interfere with the radiation patterns, its effect should be limited to a small shift of the resonant wavelengths. From the radiation patterns shown in the following, we see that this is the case for the brightest resonances, hence we neglect the presence of the tip throughout.

4.2.1 Designing nanostructures

To demonstrate the theory derived in Sec. 4.1, and to investigate the effect of different nanostructures upon the Purcell factor, photonic Lamb shift and radiative enhancement of an electric dipole emitter embedded in a dielectric medium (air),

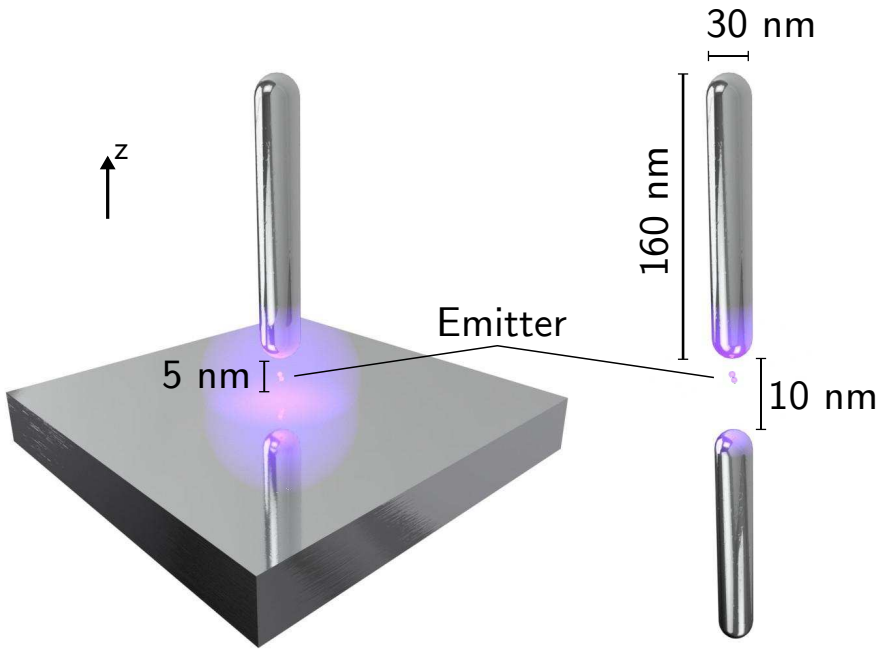

Figure 4.2: Schematic illustrations of the main nanostructure geometries considered. On the left-hand side an Al particle held above a substrate by a tip (not shown) as done in aperture-less Scanning Near field Microscopy. We consider Al and SiO_2 substrates with thickness such that reflection of light from the lower surface is negligible. On the right-hand side, we show two nanoparticles with the lower particle in the same position as the particle's image in the left-hand side.

in the following we consider four different nanostructure geometries and compositions. These are: (a) a nanorod above a metallic (planar, semi-infinite) substrate comprised of Al, with its long axis aligned with the normal to the substrate, and a 5 nm particle-substrate gap; (b) similarly, a nanorod above a dielectric substrate comprised of SiO_2; (c) a lone nanorod in a homogeneous medium; (d) and a pair of identical coaxial nanorods in a homogeneous medium, with a particle-particle gap of 10 nm*. In all cases, the nanorods are comprised of Al, with semi-spherical end caps, semi-axes of 80 nm and widths of 30 nm. These geometries allow us to identify the roles of both the particle and the substrate, and to verify the analogy between a particle near a metallic substrate and two identical particles. We define our coordinate system such that the $\hat{z}$-axis is aligned with the rods long axis,

*Such that for the particle pair, the bottom nanorod is in the position of the nanorods image in (a) and (b).

and set the origin at the substrate interface (a,b), at the centre of the particle-particle gap (d), and analogously for the lone particle (c) (where the particle is in the same position as the top particle in (d)). For each case, the dipole is located along $\hat{z}$ (*i.e.* $\boldsymbol{r'} = (0, 0, r'_z)$ with $r'_z = 2$ nm). Schematic illustrations of the main cases considered are shown in Fig. (4.2). We use a Lorentz-Drude model for the dielectric function of Al [182], and the Sellmeier equation given in Ref. [215] for SiO_2, which is valid from $0.21 - 3.71$ μm.

We consider axially symmetric set-ups, so that we can order the principal modes into channels with different values of m, the quantum number of the component of the orbital angular momentum along the axis of the nanorod. In all cases, Eq. (4.13) becomes,

$$\mathcal{G}_0^S(\boldsymbol{r}, \boldsymbol{r'}) = -\mathcal{G}_0(\boldsymbol{r}, \boldsymbol{\sigma}) \circ_{\partial V_0} X\Pi^S(\boldsymbol{\sigma}, \boldsymbol{\sigma'}) \circ_{\partial V_0} \mathcal{G}_0(\boldsymbol{\sigma'}, \boldsymbol{r'}). \tag{4.22}$$

$\mathcal{G}_0$ gives the propagation from the dipole to the particles and vice versa and is the well know electric Green's function for vacuum for the single particle and the pair of particles. When the two substrates are included, $\mathcal{G}_0$ is the vacuum Green's function plus $G_0^{EP;R}$ that depends on the material used for the substrate and continuous sets of plane waves. The projectors $\Pi^S(\boldsymbol{\sigma}, \boldsymbol{\sigma'})$ depend upon the principal modes of the particles; these modes depend on the external medium and include multiple scattering with substrates at all orders. Hence, we expect variations both in the position of the mode resonances and the way in which they couple and propagate light.

The principal modes and their radiative properties are used to determine the enhancement of the energy radiated in the upper-half space for each geometry and over a cone with a 60° semi-angle and axis aligned along $\hat{z}$, detected at least 10 wavelengths away from the dipoles[3]. In Fig. (4.3) we show the far field radiative enhancement over both the detection cone and the entire upper semi-space for dipoles with linear polarization along $\hat{z}$ for each of the nanostructure geometries. The far field intensity is normalized by the equivalent intensity[4] radiated by a dipole in vacuum. Dipoles with a polarization orthogonal to the nanorod axis

[3]This is sufficiently far that the asymptotic far field expressions are valid.

[4]Into the same solid angle.

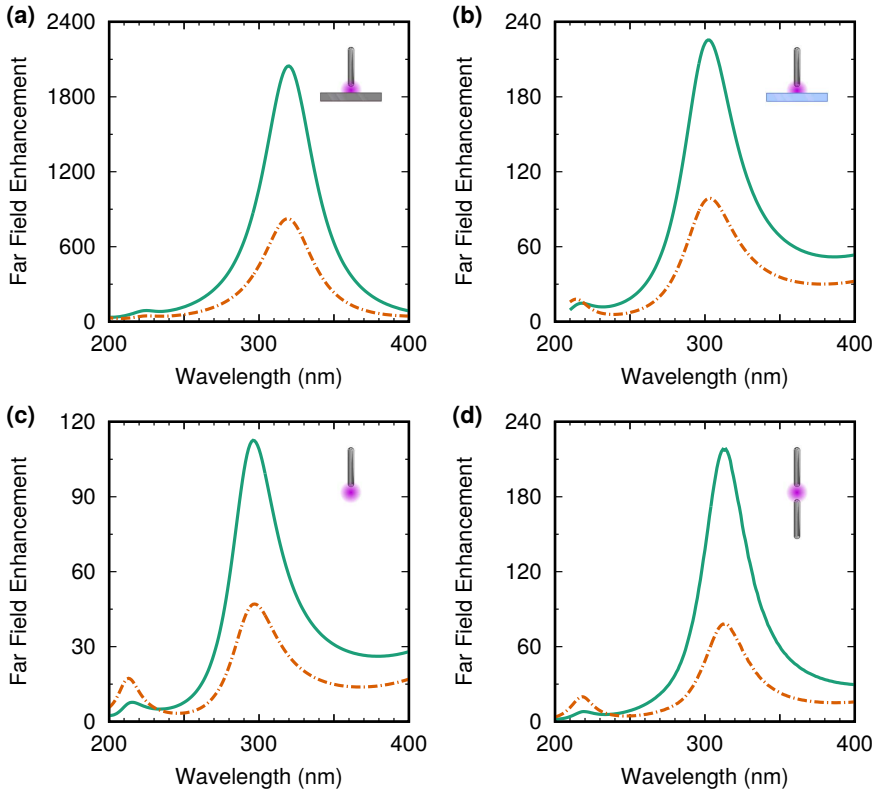

Figure 4.3: (a) Far field enhancement for dipole emitters with linear polarization perpendicular to the substrate at 3 nm from the nanorod shown in Fig. (4.2) and at 2 nm from an Al substrate. We plot the far field enhancement with respect to vacuum, I/I_0 over the detection cone with a 60° semi-angle (solid green line) and over the upper semi-space (dashed orange line), where I is the far field intensity collected in presence of the nanostructures and I_0 is the corresponding far field intensity collected in free space. The enhancement over the cone can be larger than that over the upper semi-space due to reshaping of the radiation patterns, and interference effects. (b) Far field enhancements as in (a), but with a fused silica (SiO_2) substrate. (c) Far field enhancement with respect to vacuum for dipole emitters at 3 nm from a single Al nanorod. (d) Far field enhancement with respect to vacuum for a pair of coaxial Al nanorods with dipole emitters at 3 nm from one particle and at 7 nm from the other. Insets show illustrated schematics of the nanostructures relevant to each figure.

couple very weakly, and only to modes with $m = \pm 1$. These modes are not resonant in this range of wavelengths for rods of these dimensions, and so their responses are not shown. For each geometry, we can identify a large peak around 300 nm and a much smaller one around 210 nm in the far field enhancement, however for the Al substrate the enhancement is an order of magnitude larger.

The enhancement observed around 300 nm over the cone is larger than that over the entire upper semi-space due to the reshaping of the radiation patterns due to the nanostructures and interference effects. The opposite is true around 210 nm for the structures in Fig. (4.3b-d) as they radiate mainly outside the detection cone. Common to all cases is the anisotropy of the backscattered energy, with emission from dipoles orthogonal to the nanorod axis only weakly backscattered. Surprisingly, the far field enhancement for the pair of particles is closer to that of the single particle or the SiO_2 substrate than the Al substrate.

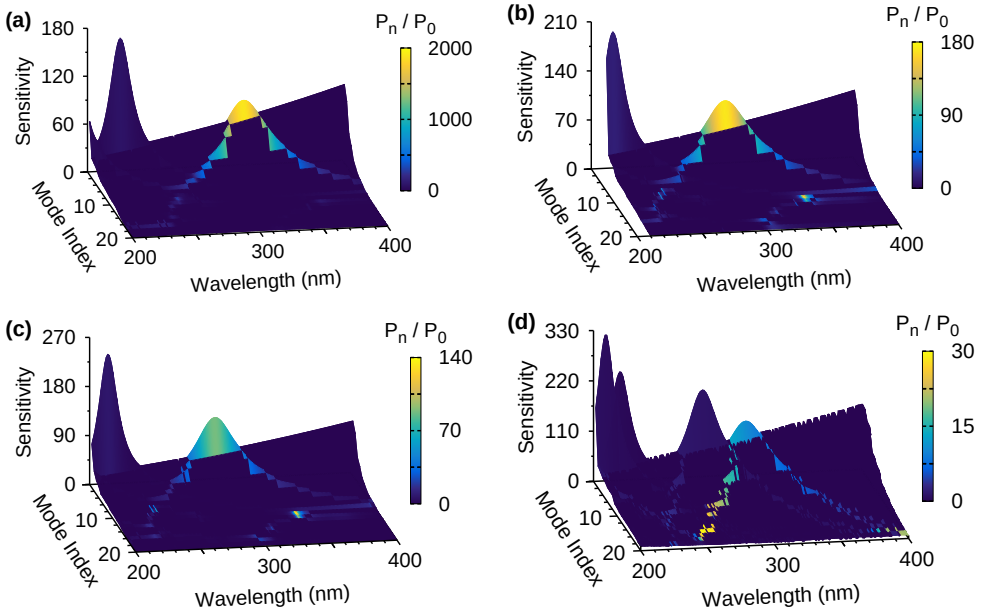

Figure 4.4: Mode landscapes for the same nanostructures. The sensitivity (vertical axis) of a trace is the reciprocal of the denominator of the projector into the mode corresponding to the trace. The higher the sensitivity, the larger the corresponding mode amplitude for a given value of the coupling between the dipole field and the mode. The two horizontal axes are the wavelength and the mode number, with mode pairs ordered according to the surface correlation between the internal and scattering modes of the pair. The traces are colour coded according to the relative amount of energy radiated by each mode into the detection cone, P_n, normalized by the corresponding energy radiated in free space, P_0. The modes in (a-b) include the effect of the substrates at all orders and are not the same as the modes of the single particle shown in (c). We can clearly identify the peaks in the far field enhancement shown in Fig. (4.3 with the resonant modes shown here. Note that at short wavelengths only the resonant mode for the rod in front of the Al substrate, (a), is able to transport energy into the detection cone.

In Figs. (4.4a-d) we analyse these results using the principal mode landscapes that show traces corresponding to the principal modes [23] and their ability to transport energy into the detection cone. By comparing these Figures, we can find that the antenna effect of the nanoparticle is mainly determined by two pairs of principal modes, with $m = 0$. For the longer wavelength peak, the colour traces indicate that the far field emission is mainly a single mode for the Al substrate, while for the other cases some non-resonant modes also contribute. For the shorter wavelength resonance the resonant modes have far field emissions comparable to that of other non-resonant modes. Note that the modes in Figs. (4.4a-b) include self-consistently the effect of the substrates at all orders and are not the same as the modes of the single particle shown in Fig. (4.4c), even if their resonances are close to those of the single particle. The presence of the substrates affects the modes in two ways: there is a shift in wavelength of the mode resonances, and the ability to carry energy can change dramatically. We also note that the principal modes for the pair of particles shown in Fig. (4.4d) have twice as many resonances as the other cases[5], but only two of these couple to the dipoles.

The difference between the resonance of the Al substrate at 224 nm and the other cases can be understood by considering the radiation patterns of the dominant modes of each system, shown in Fig. (4.5). The resonant mode of the single particle, (c), scatters energy mostly outside the detection cone; both substrates affect the radiation patterns, but only with the Al substrate, (a), is there significant radiation into the detection cone. These explain why the far field enhancement in the cone is so much larger at 224 nm for the Al substrate. The radiation pattern of the two particles' resonant mode is similar to that of the single particle, except that there are additional lobes and significantly more energy is scattered in the directions orthogonal to the $\hat{z}$ axis. Around 220 nm, the far field enhancement in the whole upper semi-space is limited by the fact that the resonant modes have, in general, less ability to transport energy into the far field than at longer wavelengths. On the contrary the dominant modes of the nanorod

[5]This is a consequence of the hybridized modes, and is not associated to the line splitting observed in strong coupling systems.

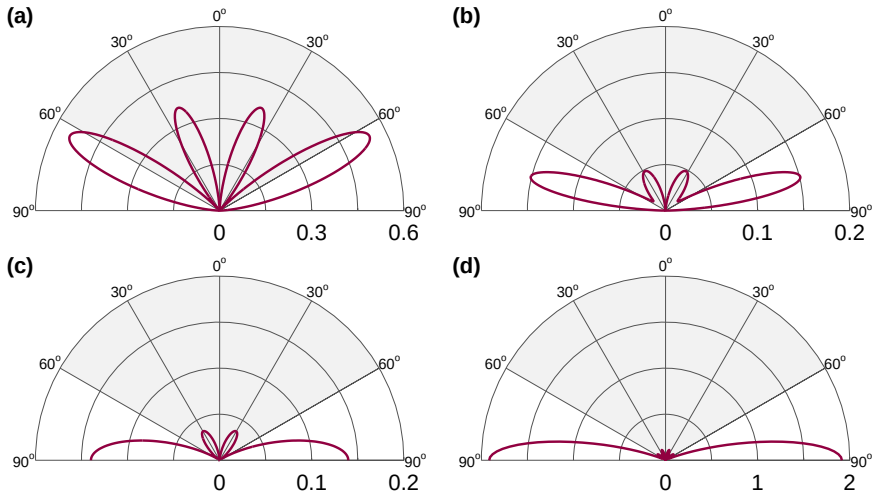

Figure 4.5: Radiation patterns of the resonant modes in the upper half-space for: (a) Al substrate at 223 nm; (b) SiO_2 substrate at 218 nm; (c) single nanorod at 213 nm; (d) two particles at 216 nm. The shaded area shows the acceptance angle of the detector. Note the strong effect of the substrate on the radiation pattern of the resonant mode: only for the Al substrate is there significant radiation within the detection cone.

at 300 nm scatter backward within the detection angle, as well as forward, such that the backward scattering is always enhanced in the corresponding modes with substrates.

In Figs. (4.6a-d) we show the Purcell factors, Γ/Γ_0, for these nanostructures. We plot also the contribution of the substrate, for (a) and (b), with $\Gamma \propto \mathrm{Im}[G^{EP;R}_{zz;0}]$. In all cases, strong peaks are observed in coincidence with the mode resonances. The largest Purcell factors (2.7×10^3) are observed at the mode resonances with the Al substrate, (a). The plateaux between the two peaks is due to the Al substrate. With SiO_2, (b), the Purcell factors are approximately a quarter of the values of those with Al and the peaks are slightly blue-shifted with respect to Al. The Purcell factors for the single nanorod, (c), are lower than those for either substrate, and again follow the mode resonances and the pair of nanorods, (d), show similar behaviour. The ratio between the energy stored in the nanostructure and the energy dissipated per cycle of the field is proportional to the Q-factor, which is a useful parameter in view of the possible application to nano-lasing. The Q-factors for the two resonances—the shorter wavelength

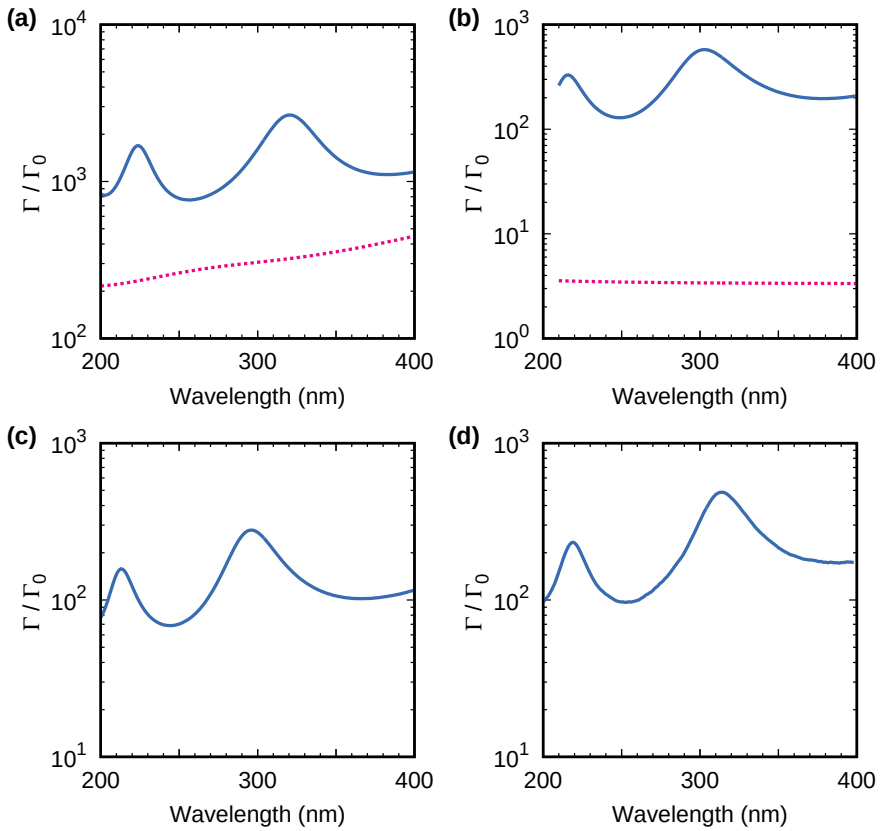

Figure 4.6: (a-d) Solid blue lines: Purcell factors for the same nanostructures. (a-b) Dashed red lines: Purcell factors for the substrates without the nanorod present. The resonant modes dominate the Purcell factors, but substrates and non-resonant modes determine the non-resonant background that can be seen at all wavelengths.

is given first—with the Al substrate are 11.45 and 7.44. For the SiO_2 substrate resonances, the Q-factors are 10.86 and 6.47. The single particle resonances have Q factors of 11.94 and 7.49, while for the two particle resonances the Q-factors are 11.6 and 7.4. We have estimated the effect of surface roughness [149], as described in Sec. 3.2.3 and found that the Q-factors are reduced by at most 10%. Therefore, experimental realization of these nanostructures can achieve Q-factors comparable to those measured in nanolasers [216, 217].

In Figs. (4.7a-d) we show the same mode landscape as in Figs. (4.3), but instead colour code the traces according to their contribution to the Purcell Factors, *i.e.* to the imaginary part of the scattering Green's function $G^{EP;S}$ at the position of the dipole. This value is not related to the ability to backscatter energy,

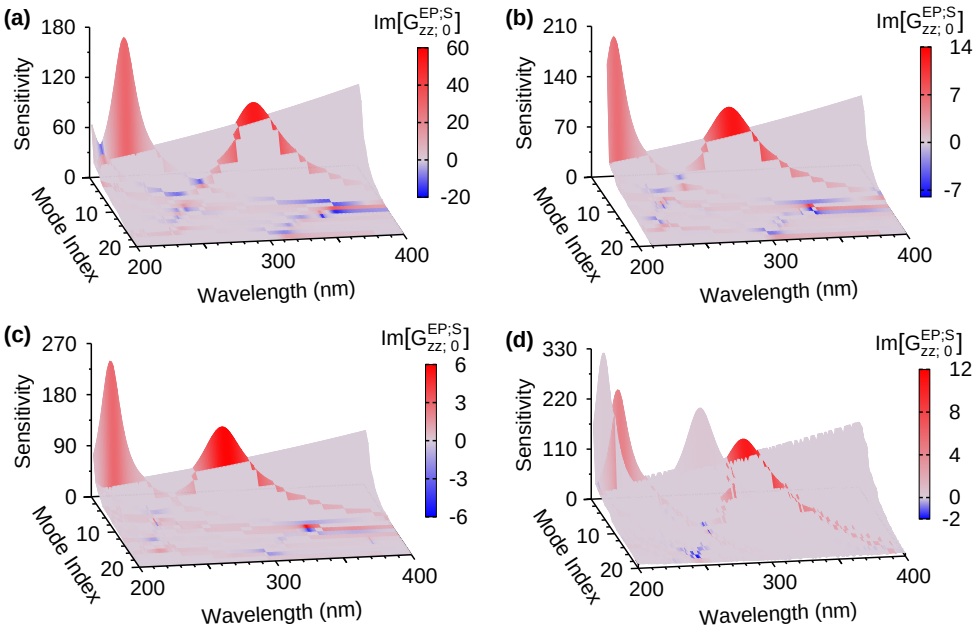

Figure 4.7: Mode landscapes colour coded according to the modal contributions to the Purcell factors, shown in Figs. (4.6a-d). The modal decompositions of the scattering Green's functions are found using the projectors. The axes of the plots are the same as those in Fig. (4.4).

hence why the two peaks appear in all cases. However, the large Purcell factors associated to the short wavelength peak will be very difficult to observe without an Al substrate. The analysis of the properties of the principal modes shown in the landscapes allows us to understand when a large Purcell factor is difficult to observe, primarily because the modes responsible for its magnitude are unable to transport energy to the detector.

Finally, the photonic Lamb shifts, normalized by the decay rate in vacuum for ease of comparison with the Purcell factors, are shown in Figs. (4.8a-d). The principal modes' contribution to the Lamb shift has rapid variations in coincidence with the maxima of the Purcell factor, showing a causal relation similar to the one between absorption and refractive index. In this range of wavelengths, there are no bulk resonances for Al, (a), or SiO_2, (b), and therefore the substrate contribution to the Lamb shift does not show rapid variation. However, the Lamb shift due to the Al substrate is very large and would need to be carefully considered when choosing specific emitters. The Lamb shifts for a single particle, (c), and a pair of particles, (d), again show similar behaviour.

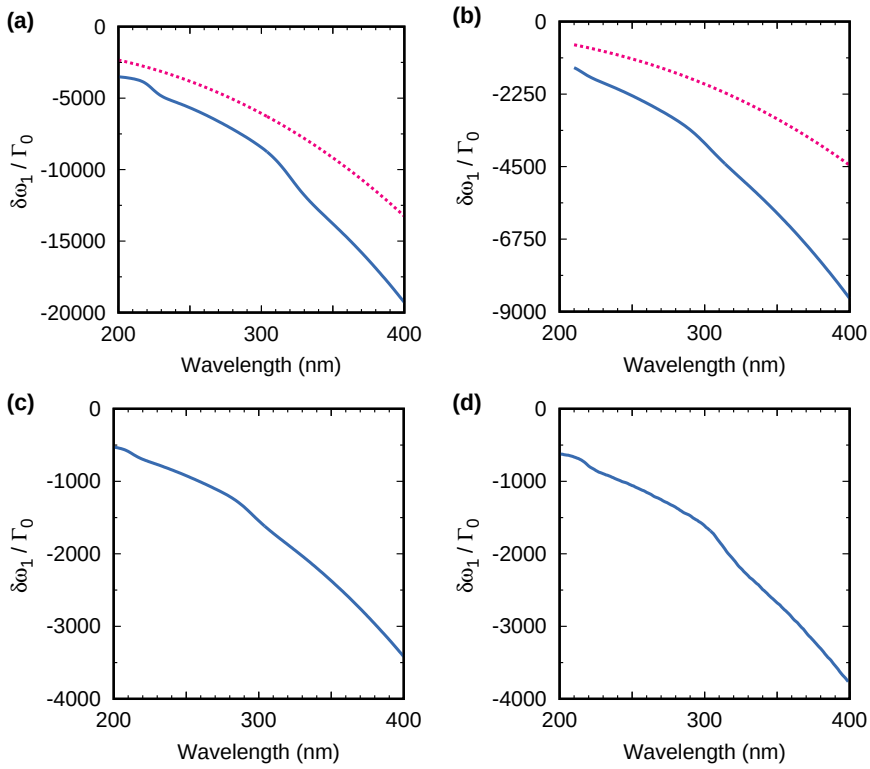

Figure 4.8: Solid blue lines (a-d): Photonic Lamb shifts of the emitter's resonance frequency normalized by the decay rate Γ_0. Dashed red lines (a-b): Photonic Lamb shifts for the substrates without the nanorod present. The contribution of the resonant modes to the Photonic Lamb shifts has a dispersive type behaviour that is a consequence of causality.

From analysing these geometries, we can conclude that particles in front of a metallic substrate have the best properties, and largest enhancements, for observing fluorescence signals in the ultraviolet.

4.2.2 Gap enhanced fluorescence

In Sec. 4.2.1, we found that metallic nanorods in front of a planar substrate made of the same material can strongly enhance both the rates of spontaneous emission, and far field radiation, for a dipole located in the particle-substrate gap. These nanostructures can exhibit very sharp spectral features, where the response is governed by very few principal modes. In this Section, we use the dielectric functions for gold, silver and aluminium [182] to examine which of these metals enables the largest enhancement of the far field radiative rate, particularly in the ultravio-

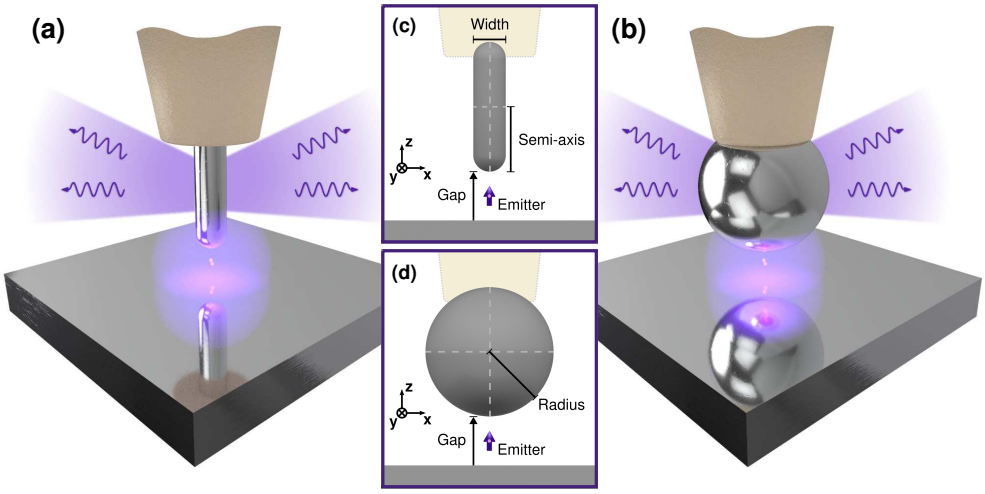

Figure 4.9: Simple schematic of a metallic nanorod (a) and a nanosphere (b) coupled to substrate made of the same metal. The nanoparticle is held into position by a dielectric cantilever. The range of angles with the strongest emission of the far field radiation is shown in light blue, and is symmetric about the vertical axis. Geometrical parameters for the rod, (c) and the sphere, (d), not to scale. The dipole is held in place by a dielectric spacer (not shown).

let. We are interested in finding nanostructures capable of strongly enhancing far field radiative rates, and we consider nanospheres and nanorods, with their axis orthogonal to the substrate, and gaps varying from 5 nm to 20 nm, see Fig. (4.9), typical of Scanning Near field Microscopy [101] and patch antennas [196].

We will then investigate how peaks in the enhancements can be tuned in order to find the optimal structure, over wavelengths ranging from 150 nm to 650 nm, and how the ratio between emission rate and far field radiative rate changes with the size of the gap. By examining properties of the modes, we will see how they explain the observed responses of the nanostructures considered. For the nanorods, we vary the length of the semi-axis but maintain a constant width of 30 nm in all instances, and again employ a geometry with semi- spherical end caps, *i.e.* where the radius of the cap is equivalent to half the width of the cylindrical body of the particle. For both types of particle, emission and radiative rates are enhanced only for dipoles polarized along the normal to the substrate, $\mathbf{p} = p_z \hat{z}$, and by modes symmetric under rotations about the normal.

In Fig. (4.10) we show the Purcell factors, the enhancement of the emission

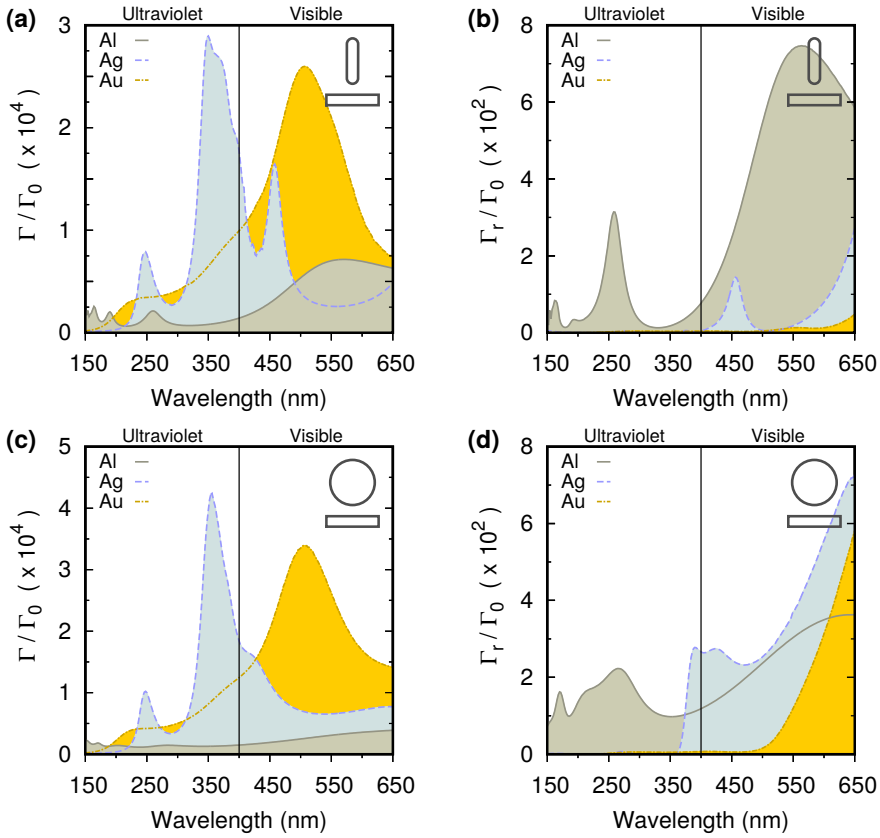

Figure 4.10: (a) Purcell factors (enhancement of the emission rate) Γ/Γ_0, for a dipole in the middle of a 5 nm gap and polarization orthogonal to the substrate, versus wavelength for nanorods with a semi-axis length of 60 nm and substrates both made of Al (grey solid), Ag (blue dashed), and Au (yellow dot- dashed). (b) Far field radiative enhancement Γ_r/Γ_0 for the same nanostructures. (c) and (d) as in (a) and (b), respectively, but for nanospheres with 60 nm radius and a 5 nm gap. Au and Ag can have larger Purcell factors than Al across the considered spectrum, but for both particles only Al has significant radiative resonances in the deep ultraviolet.

rate Γ/Γ_0, and the far field radiative enhancement, Γ_r/Γ_0, for a dipole in the middle of a 5 nm gap between a nanorod, or a nanosphere, and a substrate both made of Al, Au or Ag. Strong radiative resonances depend on the shape of the particle, and can be observed for wavelengths longer than the plasmon resonance's wavelength where the metal has a higher reflectivity. Au and Ag have plasmon resonances within the considered spectrum, while Al also has a strong plasmon resonance at shorter wavelength. As a consequence, Au and Ag can have larger Purcell factors than Al from 150 nm to 650 nm, but only Al has

significant radiative resonances below 370 nm. For this reason, we focus in the following on Al nanostructures.

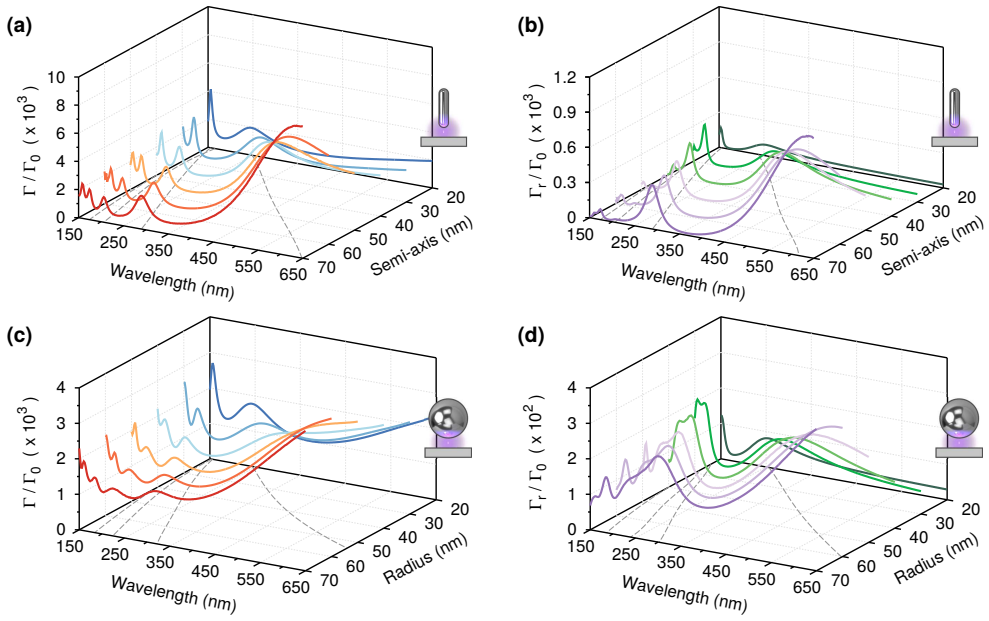

Figure 4.11: (a) Purcell factors in the middle of a 5 nm gap versus wavelength for nanorods with semi-axis varying between 20 nm and 70 nm in steps of 10 nm. The dashed lines are polynomial fits of the positions of the maxima. (b) Far field radiative enhancements Γ_r/Γ_0 for the same nanostructures as (a). The second broadest resonances have enhancements of the radiative decays of more than two orders of magnitude in the deep ultraviolet. Purcell factors (c) and far field radiative enhancements (d) of Al nanospheres with radii varying between 20 nm and 70 nm in steps of 10 nm, with a gap of 5 nm. The spectral features of the nanospheres are less sharp than those of the nanorods. All the resonances have far field radiative enhancements of more than two orders of magnitude in the deep ultraviolet.

We demonstrate the tunability of the resonances for Al nanostructures by varying the length of the semi-axis of the nanorods, and radius of the nanospheres, between $20 - 70$ nm in increments of 10 nm while maintaining a gap of 5 nm. In Fig. (4.11a) and (4.11c), we compare the Purcell factors for these sets of nanorods and nanospheres, respectively. Similarly, in Figure (4.11b) and (4.11d) we show the far field radiative enhancements for the same sets of structures. Both nanorods and nanospheres show peaks in which the Purcell factor at the dipole's position is strongly enhanced, and which are blue-shifted as the length of the semi-axis, or radius, is decreased. The positions of these peaks primarily

depend upon the length of the major axis for the nanorod, and the radius of the nanosphere, and are almost spectrally coincident for particles of equivalent length, but the peaks of the nanorods are narrower and more clearly resolved. By comparing the sets of results shown in Fig. (4.11), we can see that the two peaks at longer wavelengths in the Purcell factors correspond with large far field radiative enhancements for the nanorods. While for nanospheres, the peaks in the far field radiative enhancements are generally weaker and broader than the corresponding peaks for nanorods, with the second largest broad feature in the far field radiative enhancements being associated to two consecutive peaks in the Purcell factors.

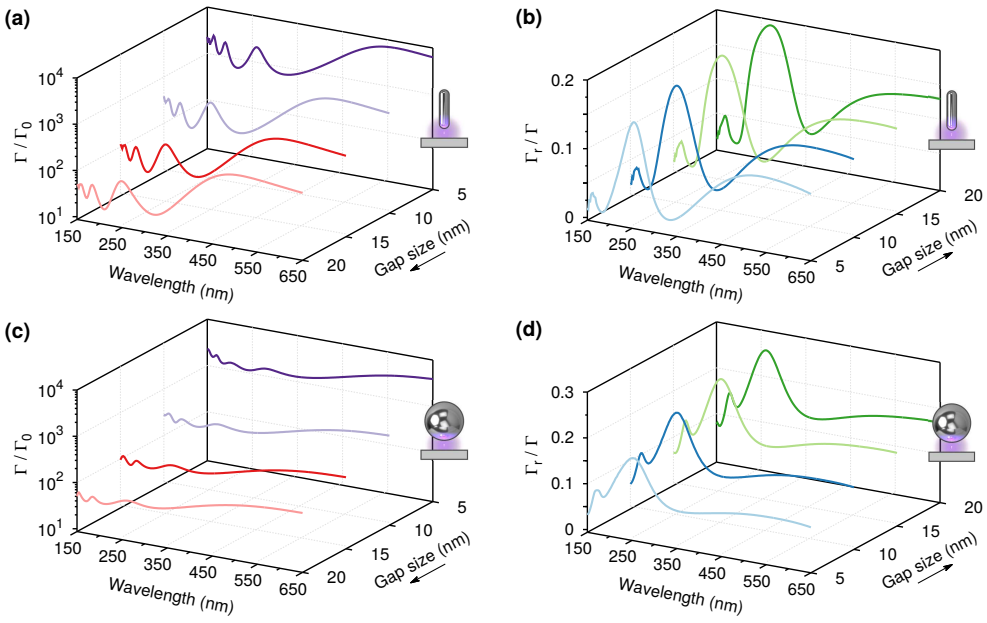

Figure 4.12: (a) Purcell factors for a nanorod with semi- axis of 60 nm and gaps of 5 nm, 10 nm, 15 nm and 20 nm. The increase in Purcell factor as the gap is reduced is of two orders of magnitude and it is larger for weakly radiative modes than for radiative modes. (b) The ratios Γ_r/Γ for these nanostructures show only rises of a few percent as the gap is increased. (c) Purcell factors for a nanosphere with radius of 60 nm and gaps of 5 nm, 10 nm, 15 nm and 20 nm. The increase in Purcell factor as the gap is reduced is over an order of magnitude, but the relative peaks are smaller than for the nanorod. (d) As a consequence, the ratios Γ_r/Γ for these nanostructures are slightly larger than for the nanorods. For both nanoparticles, smaller gaps are better for enhancing the far field detection of fluorescence, because the increase in the ratio Γ_r/Γ as the gap is increased does not compensate for the large decrease in Γ_r.

In applications to sensing, the greatest efficiency would be achieved by maximizing the number of photons radiated in the far field while minimizing the number of photons coupled to dark modes and absorbed, *i.e.* maximizing simultaneously Γ_r and Γ_r/Γ. In most cases, as the dipole gets closer to the nanoparticle, Γ_r increases while Γ_r/Γ decreases and so one has to find the optimal compromise between maximizing these two quantities by examining how they vary as a function of the size of the gap. Purcell factors evaluated at the middle of the gap decrease by up to two orders of magnitude as the gap increases, as shown in Fig. (4.12a) for gaps of 5 nm, 10 nm, 15 nm and 20 nm, and a nanorod with semi-axis of 60 nm. The corresponding variations in the ratios of Γ_r/Γ are shown in Fig. (4.12b) and indicate that for this type of nanostructure Γ_r/Γ increases only by a few percent as the gap becomes wider. For a sphere with 60 nm radius, the increase in Purcell factor as the gap is reduced is comparable to that of the nanorod, see Fig. (4.12c), but the variation of Γ_r/Γ is slightly larger, Fig. (4.12d). As the increase in the ratio Γ_r/Γ does not compensate for the large decrease in the absolute values of Γ_r as the gap becomes larger, we conclude that smaller gaps are better for enhancing the far field detection of fluorescence for both types of nanoparticle. This is very different from what happens with small metallic nanospheres [202] without a substrate, where Γ_r/Γ is negligible for small gaps. From the point of view of applications, near bright resonances the limiting factor for the gap size may be due more to loading the emitters in the gap and limiting charge transfer than coupling to dark modes and absorption.

The features observed in Fig. (4.11) and Fig. (4.12) can be attributed to resonances of the principal modes, and the ability of those modes to radiate in the far field. Resonances correspond to maxima of the sensitivities of the modes and depend on the properties of the internal and external media, the geometry of the particles, and the size of the gap. Higher sensitivities correspond to larger mode amplitudes when an incident field couples to the modes, see methods. In Fig. (4.13) we show the mode landscapes, *i.e.* the traces of the mode sensitivities versus wavelength and mode number, for two of the nanostructures; the nanorod and nanosphere, with 60 nm semi-axis and radius, with a 5 nm gap. The shape of

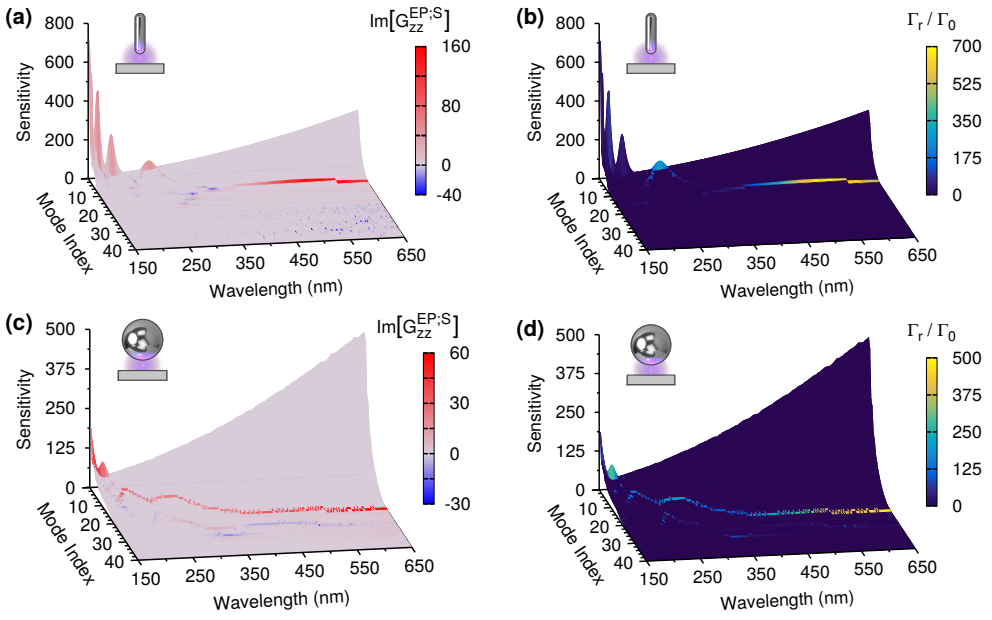

Figure 4.13: (a) Mode landscape for the nanorod with 60 nm semi- axis and 5 nm gap. The mode traces in these three dimensional plots are an intrinsic characteristic of the nanostructures and do not depend on the incident field. The vertical axis gives the sensitivity, whose maxima corresponds to mode resonances. The higher is the trace's sensitivity, the higher is the corresponding mode amplitude for a given value of the coupling between the dipole field and the mode. The two horizontal axes are the wavelength and the mode number, which indicates the order of mode pairs according to the surface correlation between the internal and scattering modes of the pair. The mode traces are colour coded according to the contributions to the Purcell factors shown. Note that the Purcell factors are dominated by a small number of modes and that for the peak at the longest wavelength the vertical variations of the mode trace are much smaller than for the other resonances. (b) Same mode landscape as in (a), but with mode traces colour coded according to the far field radiative enhancement Γ_r/Γ_0. Only the two resonant modes at longer wavelengths contribute significantly to the radiative decay. Also for a nanosphere with 60 nm radius, only a small number of modes contribute significantly to the Purcell factor, as shown in (c), or the far field enhancement, (d). The jitters of the bright modes in some landscapes are due to changes in mode indexes when several mode pairs have similar surface correlations.

the mode landscapes are independent of the incident field, and the mode indexes are arbitrarily assigned according to the surface correlation between mode pairs at each wavelength. With this format, significant resonances only appear towards the back of the landscapes, for modes with lower indexes, while modes with higher

indexes are important only very close to the particle surface, and so we can limit the number of modes required in the following analysis.

In Fig. (4.13a) we show the mode landscape for the nanorod, which is colour coded according to the contribution of each mode to the Purcell factors via the expansion of the scattering Green's function, Eq. (4.14), which appears in Eq. (4.17). Comparing the mode landscape with the Purcell factors shown in Fig. (4.12a), we find that each peak is associated to one dominant mode. The mode traces shown in Fig. (4.13b) are instead colour coded according to the far field radiative enhancement, Γ_r/Γ_0, induced by each mode. These mode landscapes show that the radiative decay is also determined by a very low number of modes, but that only the two broader resonances at longer wavelengths correspond to strongly radiative bright modes, while the other resonances are due to dark modes which radiate more weakly in the far field.

Figure (4.13c) and Fig. (4.13d) show the mode landscape for the nanosphere colour coded according to the contributions to the Purcell factors and the far field radiative enhancement, respectively. These landscapes show that, compared with the nanorod, the nanosphere has broader resonances with smaller peak values of the sensitivity; moreover, there are modes radiating in the far field for a wider interval of wavelengths, although less effectively than the nanorod's bright modes. From the colour coding of the traces, we also see that there are more modes coupled to the incident field, so that interference effects among these modes are more important than for the nanorod. The mode landscapes for the other particles – not included – show that as the semi-axis of the nanorod, or the radius of the nanosphere, is reduced, the resonances are blue shifted. However, the brightest modes are always the two modes with resonances at longer wavelengths for the nanorods, with the nanospheres having further weakly radiating modes resonant at shorter wavelengths.

Finally, by comparing the landscapes colour coded with the Purcell factors, Fig. (4.13a) and Fig. (4.13c), with those color coded with Γ_r/Γ_0, we see that the contribution of non resonant dark modes to the radiative resonances is negligible. This explains why the ratio Γ_r/Γ shown in Fig. (4.12) does not change much as

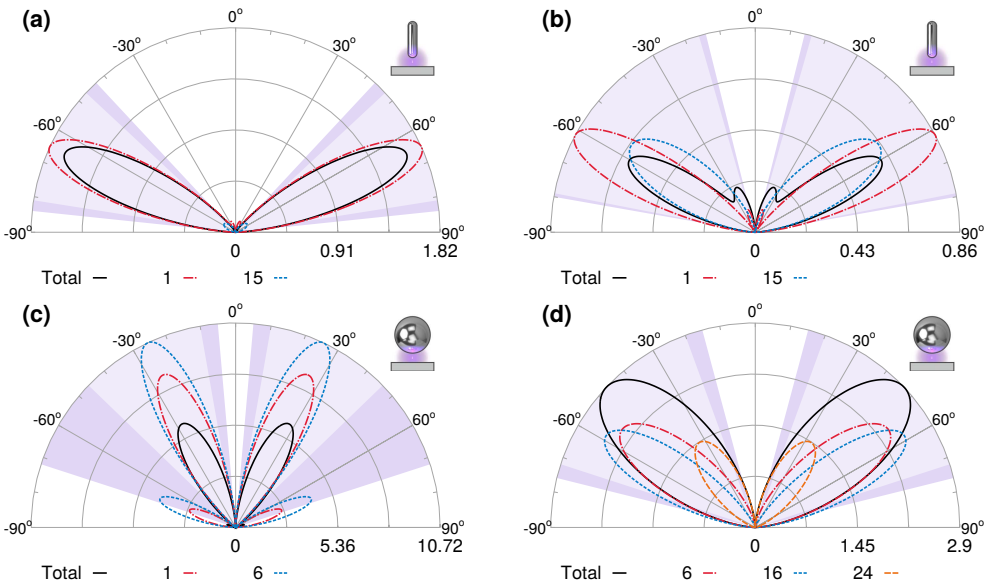

Figure 4.14: Radiation patterns for nanoparticles with a 60 nm semi-axis and 5 nm gap (black solid line) and the dominant modes at selected wavelengths. The light shaded areas indicate the angles into which 90% of the total energy is scattered, and the dark shaded areas increase this to 95%. For the nanorod there are two dominant modes (dashed red and blue lines) at 164 nm (a) and at 190 nm (b). The radiation pattern of the total field results from the interference among the modes; in both cases the total intensity is reduced along the direction of maximal emission of the dominant mode. For the nanosphere, the total field at the corresponding resonances is more strongly backscattered than for the nanorod, see (c) at 170 nm and (d) at 210 nm, where there is a third mode which contributes significantly to the total field.

the gap is increased.

As we have shown, each spectral feature in Fig. (4.11) and Fig. (4.12) can be described using a very small number of modes, and so we can further characterize these features by investigating the field distributions of the relevant modes in the near and far field. For the nanorod, with 60 nm semi-axis, there are two dominant modes which contribute significantly to the far field enhancement at the shorter wavelength resonances shown in Fig. (4.13b), at 164 nm, shown in Fig. (4.14a), and at 190 nm, Fig. (4.14b). The radiation pattern of the total field results from the interference among the modes and in both cases the total intensity is reduced along the direction of maximal emission of the dominant mode. For the nanosphere, with 60 nm radius, the total fields at the corresponding

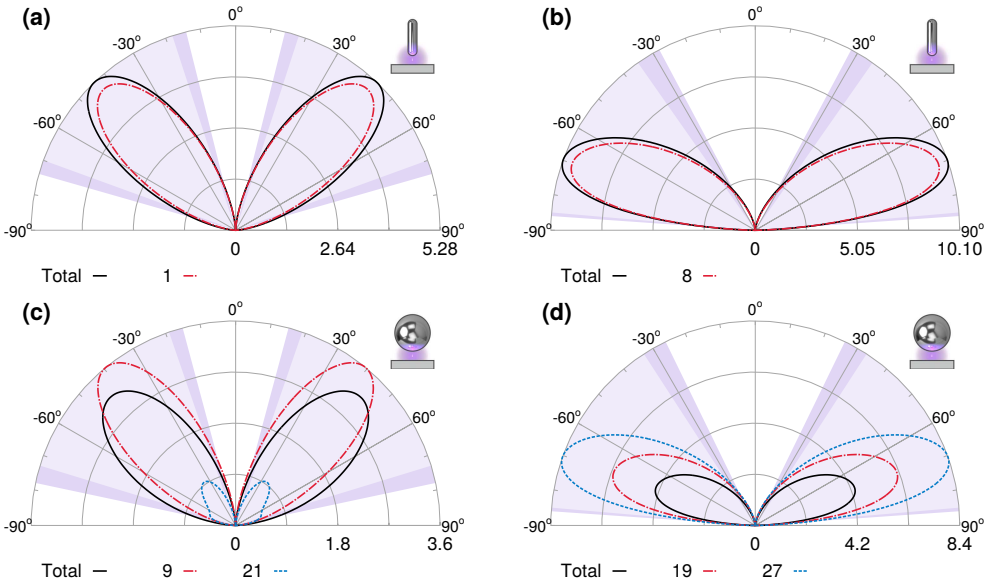

Figure 4.15: As in the previous figure, the light shaded areas indicate the angles into which 90% of the total energy is scattered, and the dark shaded areas increase this to 95%. For the nanorod the total field and the dominant mode radiation patterns are almost indistinguishable when there is only one dominant mode as at 260 nm, (a), and 560 nm, (b). In these two cases, the residual emission due to weak modes leads to a small increase along the direction of maximal emission of the dominant mode. The radiation patterns for the nanosphere at 280 nm (c) and 600 nm (d) strongly resemble those for the nanorod, however the total field for the nanosphere is always less than that of the resonant modes due to negative interference from another mode.

resonances in Fig. (4.13d) are more strongly backscattered than for the nanorod, shown in Fig. (4.14c) at 170 nm, and in Fig. (4.14d) at 210 nm, where there is a third mode which contributes significantly to the total field. For the nanorod, at the two bright resonances at longer wavelengths there is only one dominant mode and the total field and the dominant mode radiation patterns are almost indistinguishable, at 260 nm, Fig. (4.15a), and 560 nm, Fig. (4.15b). In these two cases, the residual emission due to weak modes leads to a small increase along the direction of maximal emission of the dominant mode. The radiation patterns at the longer wavelength resonances for the nanosphere at 280 nm, Fig. (4.15c), and 600 nm, Fig. (4.15d), strongly resemble those for the nanorod, however the total field for the nanosphere is always less than that of the resonant modes due to negative interference from another mode.

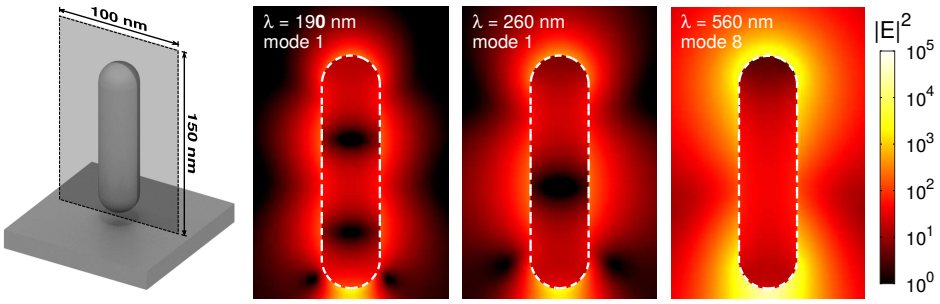

Figure 4.16: Near field intensity maps for individual mode pairs of the 60 nm nanorod with a 5 nm gap, corresponding to modes shown in Fig. (4.14a) and Figs. (4.15a-b). We show the logarithm of the electric field intensity, in arbitrary units, calculated on a 100 nm ×150 nm plane through the centre of the particle, where the bottom edge is adjacent to the substrate interface. The particle boundary is indicated with a white dashed line. The bright mode resonant at 560 nm displays the lightning rod effect, and has a dipolar character. The number of observed nodes increases for resonant modes at shorter wavelengths, which have the character of higher order multipoles.

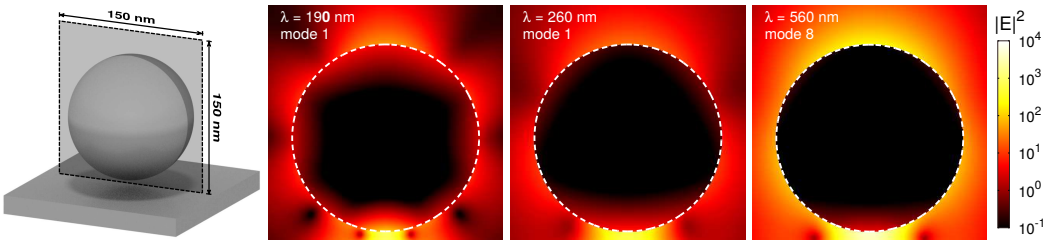

Figure 4.17: Near field intensity maps for individual mode pairs of the 60 nm nanosphere with a 5 nm gap, corresponding to modes shown in Fig. (4.14c) and Figs. (4.15c-d). We show the logarithm of the electric field intensity, in arbitrary units, calculated on a 150 nm ×150 nm plane through the centre of the particle, where the bottom edge is adjacent to the substrate interface. The particle boundary is indicated with a white dashed line. We again observe an increase in the number of nodes in the intensity pattern for modes at shorter wavelengths.

In Fig. (4.16) and Fig. (4.17), we show the near field intensity distributions for three of the brightest resonant modes at select wavelengths for the nanorod and nanosphere, respectively, and which correspond to modes shown in Fig. (4.14) and Fig. (4.15). These field distributions were calculated on a plane normal to the substrate, with the bottom edge adjacent to the substrate interface, which bisects the particle. In both cases, the modes at longer wavelengths have a higher intensity and we observe that the number of nodes in the intensity patterns

increases for modes at shorter wavelengths.

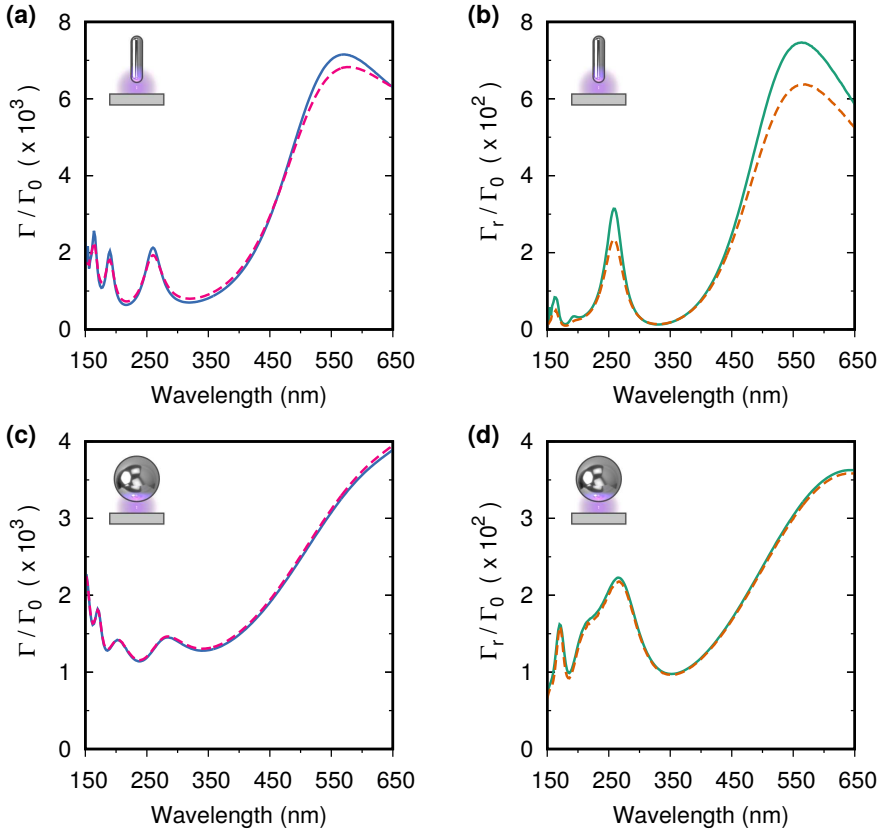

Figure 4.18: The Purcell factors in the middle of a 5 nm gap for a nanorod with 60 nm semi-axis (a), and a nanosphere with 60 nm radius (c), with (red dashed) and without (blue solid) the presence of surface roughness effects. For the same particles, in (b) and (d) respectively, we show the far field radiative enhancement with (orange dashed) and without (green solid) the presence of surface roughness effects. Including surface roughness effects has little effect upon the nanosphere and reduces the magnitudes of the observed resonances of the nanorod by, at most, 25%.

Finally, it is not always easy in experiments to control the quality of the surface roughness of the metallic nanostructures. For this reason we compare, in Fig. (4.18), the Purcell factors and far field radiative enhancement of nanostructures with the same geometry, but different surface roughness. The main effect of surface roughness is a decrease in the scattering length of conduction electrons inside the metal, and can be accounted for by including an additional size dependent damping term in the dielectric function [149], see Sec 3.2.3. The presence of surface roughness affects the nanorod more strongly, as it has a dimension compa-

rable to the mean free path of the conduction electrons in Al ($\approx$ 20 nm [165]), but it only reduces the magnitudes of the observed resonances of the 60 nm nanorod by, at most, 25%. For the 60 nm nanosphere, the effect of surface roughness upon both the emission and far field radiation rates is negligible. As the presence of surface roughness does not affect strongly the results shown in this Section, these very large enhancements can be observed in experiments.

4.3 Summary

In this Chapter, we have presented a new formulation of Green's functions that allows us to find the decay and detection rates, and frequency shifts in nanophotonic systems made by combinations of nanoparticles and substrates. This method uses an analytical decomposition of the Green's functions of the system into continuous spectra of plane waves for substrates and discrete spectra of modes for particles. This provides an efficient way to calculate the Green's functions of complex nanostructures whenever they are required; such as, for instance, electron energy loss spectroscopy [205, 206].

In Sec. 4.2, we have used this theory to show that using aluminium we can achieve Purcell factors of a few thousands over a broad range of wavelengths. Combining the antenna effect of a nanorod with a substrate leads to large values of the Purcell factors and the enhancement of the far field emission in the upper half-space, above the substrate interface, as the gap between the nanorod and substrate is narrowed. At the mode resonances, the largest values of the Purcell factors correspond to enhancement in the far field emission in the upper half-space of over 3 orders of magnitude. Higher directionality of the radiation patterns and frequency selectivity could be achieved by combining more than one nanorod with layered substrates [151].

The near and far field response is determined by very few pairs of principal internal and scattering modes, where the two brightest modes have broad resonances that can be tuned from the visible to the ultraviolet by changing the length of the nanorods. In this way one can optimize the nanostructure with respect

to the emitter simply choosing the size of the nanoparticle so that a radiative resonance is tuned with the fluorescence frequency. As a result of the very low numbers of dominant modes near these bright resonances, the ratios Γ_r/Γ depend only weakly on the size of the gap, so that the enhancement of the radiation rates can be maximized by using small gaps. An aluminium nanosphere coupled to a substrate has a similar response, with broader bright resonances and weaker enhancements. These resonances allow us to enhance by orders of magnitude the Purcell factors and the radiative rates from the visible to the deep ultraviolet.

Conclusions

Summary

In this thesis we have presented theoretical and numerical results related to the application of the theory of principal modes (TPM) to the description of phenomena related to the optical excitation of plasmonic nanostructures. In Chap. 1 we reviewed this semi-analytical theory, which provides an unambiguous method of defining resonances in Maxwell's equations that can be applied to any dielectric or metal particle, without sharp edges. The electromagnetic response of the particle is decomposed into internal and scattering modes that are coupled pair-wise at the surface, as are Mie's solutions for the sphere, and resonances are defined geometrically via the spatial correlation between mode pairs. We have shown that principal modes can be defined for multiple particle systems by hybridizing the single particle modes, including self-consistently multiple scattering to all orders.

In Chap. 2, we have applied the TPM to investigate the complex spatial features of spectroscopic transmission images obtained using a scanning near-field optical microscope (SNOM) to illuminate gold nanodiscs. In aperture SNOM, a near-field probe with a metal coated tip is used to locally excite a sample and the resulting transmission signal is measured in the far-field. We discussed the modelling of the field from such a probe, and identified a simple model which employs a coherent superposition of electric and magnetic dipoles located in the aperture plane of the probe. Experimental results were presented, which were produced as part of an internaional collaboration with institutes in Japan, for nanodiscs with diameters between $400 - 800$ nm, and with a thickness of 35 nm.

Using the TPM, and a simplifed model of the experimental conditions including the dipole tip model, we found that the numerical calculations were able to qualitatively reproduce the observed transmission images for both sizes of discs over a wide range of wavelengths. A modal analysis showed that the characteristic features of the observed images arise from the contributions of only a few fundamental modes of the discs. By studying the resonances of these modes, we were able to describe the evolution of the spatial features with the wavelength of the excitation. For the large disc, two distinct spatial patterns are observed between $\lambda = 700$ nm and $\lambda = 800$ nm that can be understood in terms of the dominant modes alternately moving close to, and far from, resonance.

Chap. 3 discussed schemes for the coherent control of photonic processes using conventional light sources and multipolar waves. Control schemes using the TPM have previously been reported for linear media with a local response [51]. These schemes were reviewed and we identified the conditions for the control field which enable either the suppression or maximization of selected modes. Equivalent schemes were then presented for the coherent control of light and currents in nonlinear media and for particles with a nonlocal response.

In Sec. 3.2, we used the hydrodynamical model to include nonlocality in Maxwell's equations and discussed the structure of the transverse and longitudinal modes. We devised a scheme to control these modes using an external plane wave and an internal multipolar wave, generated by pumping an impurity, or colour centre, embedded in the particle. We compared the effects of coherent control for particles with local and nonlocal responses, using small aluminium spheres (Sec. 3.3). In both cases, we can introduce sharp features in the directional scattering and minimize absorption, depending upon which modes are controlled, by scanning the phase of the external control wave. It is only for very small spheres, with radii < 3 nm, that the difference between the two responses can be clearly distinguished in the far field.

In Sec. 3.4, the scheme presented for the coherent control of nonlinear processes can be applied independently of the specific multiphoton process at the origin of the multipolar waves. As before, the control introduces narrow features

in the response of the particle, which enables us to change the radiation pattern, suppress radiative losses or reduce absorption. There is also a high sensitivity to small variations in the local environment, including sub-wavelength spatial shifts.

In Chap. 4, we have derived a new analytical formulation of the Greens's functions for inhomogeneous systems, containing multiple particles and substrates, using the principal modes. These Green's functions include multiple scattering to all orders, and can be decomposed into continuous spectra of plane and evanescent waves for the substrate, and discrete spectra of modes for the particles. The rates of the decay and far field enhancement, as well as resonant frequency shifts, for dipole emitters can be efficiently calculated using these Green's functions. By analysing the mode resonances, we are able to design nanostructures which result in enhancements of the far field radiation rate of several orders of magnitude. We have found that the combination of a nanorod and a substrate, comprised of the same material, produce much larger enhancements than for a lone nanorod or a coaxial nanorod dimer. For nanostructures made of aluminium, enhancements of over three orders of magnitude for the rate of far-field emission were observed in the ultraviolet.

In Appendix A, we numerically tested the implementation of the principal modes to solve the scattering problem, monitoring the convergence of the solutions when increasing the function space. The functions used in Chap. 3 and Chap. 4 were derived in Appendix B and C respectively.

Applications and future work

SNOM imaging is a popular method for investigating the spatial structure and dynamic properties of plasmons. One of the most commonly used particle shapes is the nanorod, due to the geometric simplicity and strong field enhancements observed. Rather counter-intuitively, reproducing the near-field transmission images for long, thin nanorods (such as those in Ref. [91]) has proven to be a more difficult task than for discs. In this case, the simplified model of the experiment

is insufficient to account for the observed patterns. This is most likely due to the strong anisotropy of a nanorod on a substrate, the presence of which breaks the rotational symmetry of the system, strongly affecting the character of the modes. In this case, the inclusion of the substrate is paramount which requires optimising the code to deal with the lower degree of symmetry. This can be achieved using Group theory to identify the irreducible representations, and is presently being implemented. This will also enable us to investigate many other geometries with lower, or no symmetry and for which the presence of the substrate may be important.

In Sec. 3.3, we investigated the effects of nonlocality in very small spheres, with radii ≤ 5 nm. Particles of this size with embedded impurities could be very challenging to produce, and would interact weakly with light. However, the control method described applies to any system in which transverse and longitudinal waves are supported. In particular, systems such as core-shell spherical particles, with diameters of $50 - 100$ nm and an external layer with nonlocal response of a few nanometres, have similar properties to the spheres we consider here and interact more strongly with light. Consequently, these types of systems would be better from the point of view of applications. In this case, the control can be modelled similarly to the control method we described by using the Mie theory for layered spheres [218, 219]. However, depending on the materials used, there could be electron spill-out between the inner core and outer layer which would need to be included in the modelling of nonlocality [212].

A particle with this type of control, if placed at the juncture between two chains of nanoparticles, could allow or interdit the passage of light at the frequency where the control is being operated, as even the surface field outside the particle can be made negligible. In this example, the external field would be the field emitted from the end of one chain near to the sphere. For this specific application, however, one would have to consider carefully the distance between particles: for sub-nanometer distances modifications to the nonlocal theory [212] and quantum effects such as spill-out charges [213] need to be included in the model.

Also, with appropriate control beams and pump, the nonlinear control scheme presented in Sec. 3.4 could be used to control the directionality of nonlinearly generated electromagnetic waves not only in a single sphere, but also in a regular array of spheres, for which both the radiation patterns and the spatial positions could be determined. This can be very useful for applications such as optical antennae and for surface enhanced spectroscopy, providing a reference of regularly spaced optical nano-beacons for the localization of molecules.

The large enhancements we observed in Chap. 4 show that these nanostructures can be extremely useful to efficiently detect weakly fluorescent molecules, and may open fluorescence up to metabolic bio-markers or amino acids which appear in the genetic code and for which fluorescence has not yet been detected. However, the enhancements due to the structures we have considered are strongly anisotropic, and apply only for dipoles with polarizations aligned parallel to the nanorod axis. For molecular detection, enhancements for arbitrary polarizations are desirable to increase efficiency. Considering more complex particle geometries or arrangements could potentially provide more isotropic enhancements, which could be efficiently investigated using our method. Also, weakly radiative modes for nanorods have sharp line shapes, sufficiently large Q-factors, and may be suitable for nanolasing in the ultraviolet, as they are for nanolasing in the visible [220] and, depending on the dipole moment of the emitter, can be used to observe memory effects in the coupling between the emitter and radiation [199]. While experimental details such as the type of spacer used may be molecule dependent, the overall principles of gap enhanced fluorescence discussed in this Chapter should apply to a very broad class of emitters.

Finally, a large part of my doctoral work has been concerned with the development of the numerical codes used to produce the results contained in this thesis. These codes use routines for the special functions provided in Ref. [148], which are copyrighted, preventing their release to the public domain. An effort to write, or find efficient open-source versions of these routines would allow these codes to be made accessible to the nanophotonics community, and help to find

new applications for the TPM.

Appendix A

Numerical tests

In this appendix we compare the validity of the numerical solutions to the scattering problem calculated via three different methods: the discrete source method using QR decomposition to solve Eqn. (1.6) in a least squares sense (hereafter referred to as QR); construction of the principal modes by

1. Using QR decompositions to find orthonormal bases corresponding to Eqs. (1.7,1.8),
2. Forming the scalar product between the unitary matrices, U^i and U^s,
3. Finding the paired sets of principal modes via a singular value decomposition corresponding to Eq. (1.9),
4. Analytically solving for the $\mathbf{a}^i$ and $\mathbf{a}^s$ coefficients,

(this approach being referred to as the QR+SVD method); and finally, purely using singular value decompositions to find the orthonormal bases and then the principal modes (referred to as SVD+SVD). In all cases, standard linear algebra routines were used to perform the decompositions and matrix products [221].

To provide a fair comparison between the algorithms we limit the rank of the output spaces for each method, via regularisation, to be the same for all methods and then study the effect of incrementing this limit. Simulations were run for two distinct particle types, a nano-disc of radius 400 nm and depth 35 nm and a nano-rod of length 400 nm and diameter 35 nm, both with rounded edges. Other than their geometries, the two particles differ in the type of sources used

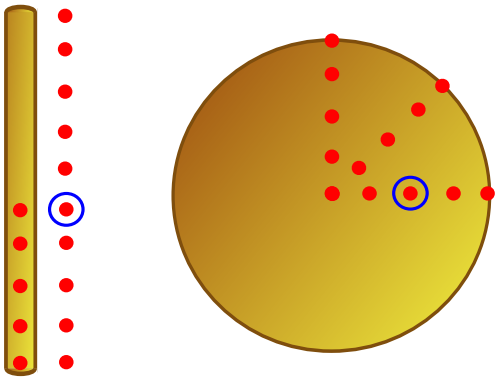

Figure A.1: Sampling points of near field excitation for a rounded gold nano-disc and nano-rod. The red points indicate the approximate location of the near field source as it was scanned above the gold nano-particles at a height of 50nm, for a rod with dimensions (l = 400 nm, d = 35 nm) and a disc (d = 800 nm, z = 35 nm). The blue circles indicate the location of the near field source used for the DSCS calculations. There are 15 sampling points for each particle (the centre of the disc was sampled with 3 different polarisations.) All of the following simulations were performed using these particles.

to represent the fields. For the rod, multipole sources are distributed along the symmetry axis in the real space, whereas for the disc the sources are located in the complex space—effectively making these ring sources distributed concentrically along the particle radius. The particles were illuminated by a near field source of wavelength 720 nm comprised of a combination of electric and magnetic point dipoles located 50 nm above the particle surface. The approximate locations of the near field source, which is moved to obtain average values for some tests by using different locations and polarisations of the source, are highlighted in Fig. (A.1).

Firstly, we compare the convergence of the solutions by plotting the DSCS, *i.e.* the angular variation of the electric field intensity in the far field, for each of the three methods by increasing the rank from an effective minimum. These results were obtained by calculating the light scattered by the excited particles into the far field along the generatrix line, $\phi = 0$, and sampling θ at equal intervals between the poles of the symmetry axis for the two particles at 0 and π, as shown in Fig. (A.2). We observe that for minimal rank there is an obvious advantage to the principal mode methods, which while not fully converged show the main features of the spectrum at the correct angles. The QR solution however,

for both the rod and disc particles, fails to even approximately produce these features of the solution when the rank is minimal. As the rank is increased both Principal Mode methods converge more rapidly than the pure QR solution, which requires the maximum rank considered to show full convergence for the disc, and only an approximate convergence for the rod. Note that with these particular source configurations, the upper bound on the rank obtainable for SVD+SVD and QR+SVD when no limit is imposed is almost half that observed for the QR algorithm.

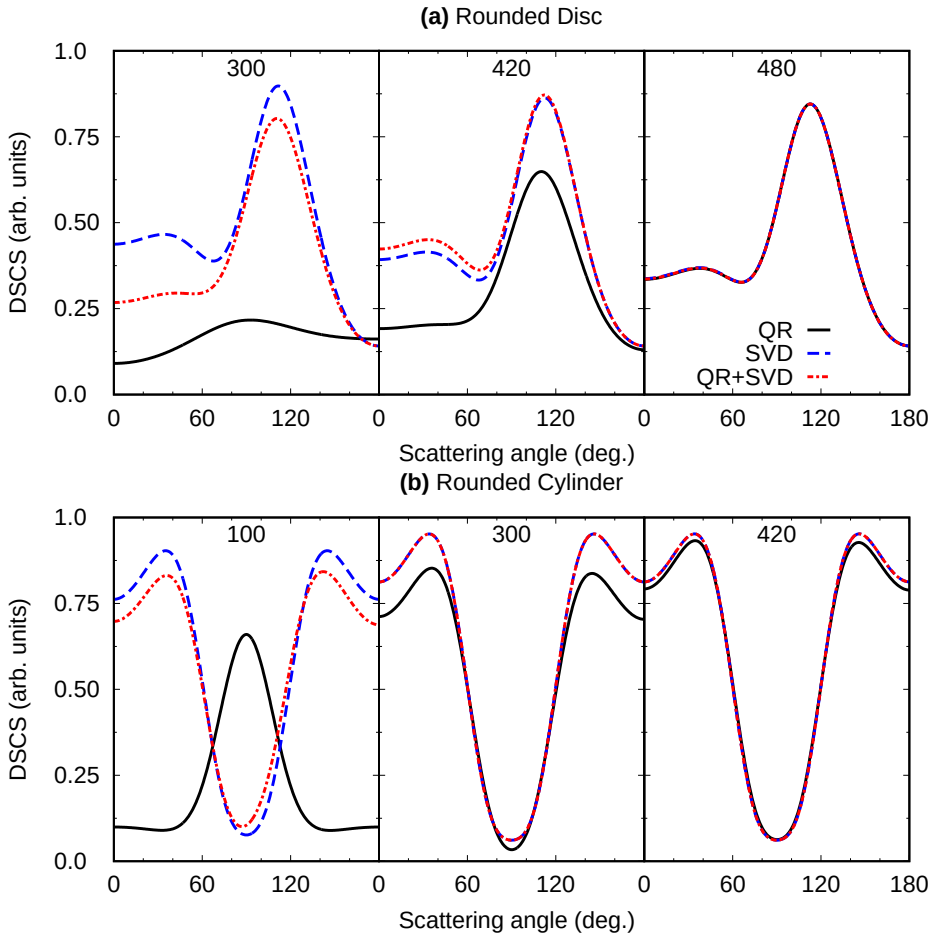

Figure A.2: Convergence of the DSCS along the generatrix line with increasing rank. The DSCS, in arbitrary units, for the three different algorithms plotted against the far field angle θ, varied incrementally between 0 and π between the poles of the particle's symmetry axis showing convergence with increasing rank of the solution matrices for a (a) disc and (b) rod.

We have observed that for low rank solutions there is a clear advantage to using a method which splits the space into two subspaces, not only for the extra

Algorithm	Time (s)
QR	102
SVD+SVD	260
QR+SVD	194
Using stored modes	36

Table A.1: Average total computational time for a full solution of the scattering problem at unrestricted rank for a single wavelength near-field excitation of the disc shaped particle using an AMD Opteron 6344 processor with a 2.6 GHz clock speed. Timings are averaged over 5 runs. For the QR+SVD and purely SVD methods we highlight the time taken for the initial calculation and also the subsequent calculations for the same particle where the principal modes are read back in from disc storage.

information about the system which this gives, but also for the accuracy of the calculations. There is also another advantage to using the principal mode methods, due to the sequential way in which the surface fields are calculated using SVD+SVD they can be stored to be used again for a different excitation of the same particle. While, for the initial calculation QR proves to be slightly quicker, as shown in Table A.1, for multiple calculations the SVD+SVD and QR+SVD methods need only calculate the principal mode fields once and the subsequent calculations are then significantly faster by factors of $\sim$5 for QR+SVD and $\sim$7 for SVD+SVD.

Appendix B

Principal modes of a sphere

In this appendix, the formulae for the principal modes of a sphere are derived from the spherical wave solutions of the Helmholtz equation [148, 78]. These modes are equivalent to Mie's solutions for a sphere, and we give both the transverse and longitudinal modes used in Chap. 3.

B.1 Transverse modes

The transverse spherical wave solutions of the Helmholtz equation are [148]:

$$\begin{aligned} \boldsymbol{M}_{lm}(r,\theta,\phi) &= z_l(kr)\boldsymbol{m}_{lm}(\Omega), & \text{(B.1)} \\ \boldsymbol{N}_{lm}(r,\theta,\phi) &= k^{-1}\nabla\times\boldsymbol{M}_{lm}(r,\theta,\phi) \\ &= \hat{\boldsymbol{r}}\frac{iz_l(kr)}{kr}\sqrt{l(l+1)}Y_{lm}(\Omega)+\frac{\partial_{kr}[krz_l(kr)]}{kr}\boldsymbol{n}_{lm}(\Omega), & \text{(B.2)} \end{aligned}$$

where the vector spherical harmonics are defined as:

$$\begin{aligned} \boldsymbol{m}_{lm}(\Omega) &= \frac{i}{\sqrt{l(l+1)}}\left(\hat{\boldsymbol{\theta}}\frac{im}{\sin\theta}-\hat{\boldsymbol{\phi}}\partial_\theta\right)Y_{lm}(\Omega), & \text{(B.3)} \\ \boldsymbol{n}_{lm}(\Omega) &= \hat{\boldsymbol{r}}\times\boldsymbol{m}_{lm}(\Omega)=\frac{i}{\sqrt{l(l+1)}}\left(\hat{\boldsymbol{\theta}}\partial_\theta+\hat{\boldsymbol{\phi}}\frac{im}{\sin\theta}\right)Y_{lm}(\Omega). & \text{(B.4)} \end{aligned}$$

The solid angle $\Omega = (\theta, \phi)$, and $\hat{\boldsymbol{r}}$, $\hat{\boldsymbol{\theta}}$ and $\hat{\boldsymbol{\phi}}$ are orthogonal unit vectors in a spherical coordinate system, and Y_{lm} are the scalar spherical harmonics [78]. The radial function $z_l(kr)$, of order l, can be either the spherical Bessel function of the first kind, $j_l(k_i r)$, in the internal space, defining regular standing waves, or

the spherical Hankel function of the first kind, $h_l(k_s r)$, in the scattering space, defining waves propagating radially outward from the coordinate origin. We identify the function used, and the relevant space, via a superscript index: where i indicates the internal space and use of the Bessel function, while s indicates the scattering space and Hankel function. The electric and magnetic components of the transverse magnetic, or electric multipole, Mie modes can be defined using these wave solutions and we can write the normalized internal and scattering modes for a given l and m as,

$$\boldsymbol{i}_{lm}^{TM} = \frac{[\boldsymbol{N}_{lm}^{i}, -iC^{i}\boldsymbol{M}_{lm}^{i}]}{R_l^i}, \tag{B.5}$$

$$\boldsymbol{s}_{lm}^{TM} = \frac{[\boldsymbol{N}_{lm}^{s}, -iC^{s}\boldsymbol{M}_{lm}^{s}]}{R_l^s}, \tag{B.6}$$

where the bracketed notation defines the electric and magnetic parts of the mode successively, and $C^i = \sqrt{\epsilon^i/\mu^i}$, where ϵ^i is the relative permittivity of the transverse waves inside the sphere that includes also the free carriers contribution, and μ^i is the relative permeability of the sphere, while $C^s = \sqrt{\epsilon^e/\mu^e}$ is similarly defined for the external medium. The normalization factors are,

$$\begin{aligned} R_l^i &= |[\boldsymbol{N}_{lm}^{i}, -iC^{i}\boldsymbol{M}_{lm}^{i}]| \qquad (B.7)\\ &= \left[|j_l(k_i r)|^2\left(\frac{l(l+1)}{|k_i r|^2} + |C^i|^2\right) + \left|\frac{\partial_{k_i r}[k_i r j_l(k_i r)]}{k_i r}\right|^2\right]^{1/2}, \\ R_l^s &= |[\boldsymbol{N}_{lm}^{s}, -iC^{s}\boldsymbol{M}_{lm}^{s}]| \qquad (B.8)\\ &= \left[|h_l(k_s r)|^2\left(\frac{l(l+1)}{|k_s r|^2} + |C^s|^2\right) + \left|\frac{\partial_{k_s r}[k_s r h_l(k_s r)]}{k_s r}\right|^2\right]^{1/2}. \end{aligned}$$

The transverse electric, or magnetic multipole, Mie modes, $\boldsymbol{i}_{lm}^{TE}$ and $\boldsymbol{s}_{lm}^{TE}$, can be obtained by exchanging $\boldsymbol{M}_{lm}$ and $\boldsymbol{N}_{lm}$ in Eqs. (B.5-B.8).

B.2 Longitudinal modes

The hydrodynamical model leads to two different dispersion relations, ϵ_t, ϵ_l for the transverse, or divergence free, waves and the longitudinal, or curl free, waves,

the latter being associated to charge density waves. These relations are,

$$\epsilon_t = \epsilon_b - \frac{\omega_p^2}{\omega(\omega + i\Gamma)}, \tag{B.9}$$

$$\epsilon_L = \epsilon_b - \frac{\omega_p^2}{\omega(\omega + i\Gamma) - \beta^2 k^2}, \tag{B.10}$$

where ϵ_b accounts for the ionic background, *i.e.* the bound charges (for the Drude model $\epsilon_b = 1$), $\beta^2 = (3/5)v_F^2$ and v_F is the Fermi velocity. By setting $\epsilon_L = 0$ in Eq. (B.10), we find the wave number for longitudinal waves,

$$k_L = [(\epsilon_b \omega(\omega + i\Gamma) - \omega_p^2)/\epsilon_b \beta^2]^{1/2}. \tag{B.11}$$

To include longitudinal waves in our framework, we just need to add the curl free solution of the Maxwell's equations,

$$\begin{aligned} \boldsymbol{L}_{lm}(r,\theta,\phi) &= k^{-1}\nabla j_l(k_L r)\frac{Y_{lm}(\Omega)}{\sqrt{l(l+1)}} \\ &= \frac{k_L}{k}\left[\hat{\boldsymbol{r}}\partial_{k_L r}[j_l(k_L r)]\frac{Y_{lm}(\Omega)}{\sqrt{l(l+1)}} - i\frac{j_l(k_L r)}{k_L r}\boldsymbol{n}_{lm}(\Omega)\right]. \end{aligned} \tag{B.12}$$

The (electric multipole) longitudinal internal principal modes are then defined as,

$$\boldsymbol{i}_{lm}^L = \frac{e^{i\psi_L}[\boldsymbol{L}_{lm}, 0]}{|L_l|}, \tag{B.13}$$

where the magnetic component of the mode is null. There are no magnetic multipole longitudinal modes. The longitudinal normalization factor, and the relative phase between the internal modes, are respectively,

$$|L_l| = \left|\frac{k}{k_L}\right|\left(\frac{|\partial_{k_L r} j_l(k_L r)|^2}{l(l+1)} + \left|\frac{j_l(k_L r)}{k_L r}\right|^2\right)^{1/2}, \tag{B.14}$$

$$\psi_L = -\mathrm{Im}\big[\log([\boldsymbol{N}_{lm}^i, -iC^i\boldsymbol{M}_{lm}^i]\cdot[\boldsymbol{L}_{lm}, 0])\big]. \tag{B.15}$$

B.3 Biorthogonal modes

For spheres (and for any finite set of modes) the biorthogonal modes can be found analytically and depend on all internal and scattering modes with the same l and m, correlated at the surface of the sphere, according to the formula,

$$\boldsymbol{u}_j' = \boldsymbol{u}_i G_{ij}^{-1}, \tag{B.16}$$

where $\boldsymbol{u}_1 = \boldsymbol{s}_{lm}$, $\boldsymbol{u}_2 = \boldsymbol{i}_{lm}$, $\boldsymbol{u}_3 = \boldsymbol{i}^L_{lm}$, G^{-1} is the inverse of the (Gram) matrix with elements $G_{ij} = (\boldsymbol{u}_i \cdot \boldsymbol{u}_j)$ and we sum over repeated indexes, where $\boldsymbol{i}^L_{lm}$ is the longitudinal mode spatially correlated to $\boldsymbol{s}_{lm}$ and $\boldsymbol{i}_{lm}$. For the magnetic multipole Mie modes, there are only two mode vectors $\boldsymbol{u}_1$ and $\boldsymbol{u}_2$.

Appendix C

Electromagnetic Green's functions

The classical dyadic Green's functions act as the propagators for the electric and magnetic fields emitted by point dipoles. In this Appendix, we derive the the Green's functions for both a homogeneous and a planar, multi-layered medium that are used in Chap. 4.

C.1 Green's function for homogeneous media

In the frequency domain, assuming an harmonic time dependence $\mathrm{e}^{-i\omega t}$, the Maxwell equations for a generalised medium supporting free charges and currents are[78],

$$\nabla \times \boldsymbol{E}(\boldsymbol{r}) = i\omega \boldsymbol{B}(\boldsymbol{r}) \tag{C.1}$$

$$\nabla \times \boldsymbol{H}(\boldsymbol{r}) = -i\omega \boldsymbol{D}(\boldsymbol{r}) + \boldsymbol{J}(\boldsymbol{r}) \tag{C.2}$$

$$\nabla \cdot \boldsymbol{D}(\boldsymbol{r}) = \rho(\boldsymbol{r}) \tag{C.3}$$

$$\nabla \cdot \boldsymbol{B}(\boldsymbol{r}) = 0 \tag{C.4}$$

where $\boldsymbol{E}$ denotes the electric field, $\boldsymbol{B}$ is the magnetic induction, $\boldsymbol{H}$ is the magnetic field, $\boldsymbol{D}$ is the electric displacement field, $\boldsymbol{J}$ is the current density, and ρ is the charge density. The constitutive relations for a non-dispersive, linear, isotropic

medium are[78],

$$\boldsymbol{D}(\boldsymbol{r}) = \epsilon_0 \epsilon_r \boldsymbol{E}(\boldsymbol{r}) \qquad (\boldsymbol{P} = \epsilon_0 \chi_e \boldsymbol{E}) \tag{C.5}$$

$$\boldsymbol{B}(\boldsymbol{r}) = \mu_0 \mu_r \boldsymbol{H}(\boldsymbol{r}) \qquad (\boldsymbol{M} = \mu_0 \chi_m \boldsymbol{H}) \tag{C.6}$$

where $\boldsymbol{P}$ is the polarization, $\boldsymbol{M}$ is the magnetization, ϵ_0 and μ_0 are the permittivity and permeability of free space respectively, ϵ_r and μ_r are the relative permittivity and permeability of the medium. The linear electric and magnetic susceptibilities $\chi_{e/m}$ relate the electric and magnetic fields to the induce polarization and magnetization respectively. The relative permittivity and permeability both have a functional dependence upon the position $\boldsymbol{r}$ (as well as ω).

By substituting the constitutive relations, Eqs. (C.5) and (C.6), and Eq. (C.1) into Eq. (C.2), we can find the inhomogeneous wave equation for the complex electric field in a linear isotropic medium,

$$\nabla \times \frac{1}{\mu_r} \nabla \times \boldsymbol{E} - \left(\frac{\omega}{c}\right)^2 \epsilon_r \boldsymbol{E} = i\omega\mu_0\mu_r \boldsymbol{J}. \tag{C.7}$$

We can write an equivalent wave equation using the electric Green's function for infinitesimal point sources,

$$\nabla \times \frac{1}{\mu_r} \nabla \times G(\boldsymbol{r}, \boldsymbol{r'}) - \left(\frac{\omega}{c}\right)^2 \epsilon_r G(\boldsymbol{r}, \boldsymbol{r'}) = \mathbb{I}\delta(\boldsymbol{r} - \boldsymbol{r'}), \tag{C.8}$$

where $\mathbb{I}$ is the identity matrix and $\delta(\boldsymbol{r} - \boldsymbol{r'})$ is the Dirac delta function which is zero everywhere except at $\boldsymbol{r} = \boldsymbol{r'}$, and is normalised such that $\int_V \delta(\boldsymbol{r} - \boldsymbol{r'}) dV(\boldsymbol{r'}) = 1$. From the continuity equation it follows that $\nabla \cdot \boldsymbol{E} = (i\omega\epsilon_0\epsilon_r)^{-1} \nabla \cdot \boldsymbol{J}$, and using the vector identity ($\nabla \times \nabla \times \boldsymbol{A} = \nabla(\nabla \cdot)\boldsymbol{A} - \nabla^2 \boldsymbol{A}$) on the first term, we can rewrite Eq. (C.7) as,

$$\left(k^2 + \nabla^2\right) \boldsymbol{E} = -i\omega\mu_0\mu_r \left[\mathbb{I} + \frac{\nabla\nabla}{k^2}\right] \cdot \boldsymbol{J}, \tag{C.9}$$

with the wave number in the medium $k = \sqrt{\epsilon_r \mu_r}\omega/c$. Using Eq. (C.8), we can write a particular solution to Eq. (C.7) relating the electric field to the current density,

$$\boldsymbol{E}(\boldsymbol{r}) = i\omega\mu_0\mu_r \int_V G(\boldsymbol{r}, \boldsymbol{r'}) \cdot \boldsymbol{J}(\boldsymbol{r'}) \mathrm{d}V(\boldsymbol{r'}). \tag{C.10}$$

The general solution includes any homogeneous fields that are present in the medium, but for our purposes we shall assume that this term is zero. We find the

solution to Eq. (C.10) by using the well known scalar Green's function, which is the solution to the scalar Helmholtz equation of the form [78, 122],

$$\left(k^2 + \nabla^2\right) g(\boldsymbol{r}, \boldsymbol{r'}) = -\delta(\boldsymbol{r} - \boldsymbol{r'}). \tag{C.11}$$

In an unbounded isotropic medium, due to the spherical symmetry, the Green's function in Eq. (C.11) does not depend on position but only the distance given by $|\boldsymbol{r} - \boldsymbol{r'}|$. By applying the Sommerfeld radiation condition[222], such that as $|\boldsymbol{r} - \boldsymbol{r'}| \to \infty$, $g(\boldsymbol{r}, \boldsymbol{r'}) \to 0$, the only physical solution is [78, 122],

$$g(\boldsymbol{r}, \boldsymbol{r'}) = \frac{\mathrm{e}^{ik|\boldsymbol{r}-\boldsymbol{r'}|}}{4\pi|\boldsymbol{r} - \boldsymbol{r'}|}, \qquad \boldsymbol{r} \neq \boldsymbol{r'}. \tag{C.12}$$

Using the scalar Green's function in Eq. (C.12) for the response of the field to sources aligned along each orthogonal direction, an expression for the electric dyadic Green's function in a homogeneous medium can be written as [223],

$$\begin{aligned} G(\boldsymbol{r}, \boldsymbol{r'}) &= \left[\mathbb{I} + \frac{\nabla\nabla}{k^2}\right] g(\boldsymbol{r}, \boldsymbol{r'}), \\ &= \left[\mathbb{I} + \frac{\nabla\nabla}{k^2}\right] \frac{\mathrm{e}^{ik|\boldsymbol{r}-\boldsymbol{r'}|}}{4\pi|\boldsymbol{r} - \boldsymbol{r'}|}. \end{aligned} \tag{C.13}$$

This tensor function is symmetric, and consequently has the general property,

$$\left[G(\boldsymbol{r}, \boldsymbol{r'})\right]^{\mathrm{T}} = G(\boldsymbol{r'}, \boldsymbol{r}). \tag{C.14}$$

The expression in Eq. (C.13) contains a singularity for $g(\boldsymbol{r}, \boldsymbol{r'})$ when $\boldsymbol{r} = \boldsymbol{r'}$, which means that the function is divergent when we evaluate fields at the source origin. However, this equation can be treated analytically and, by introducing the notation $\boldsymbol{R} = \boldsymbol{r} - \boldsymbol{r'}$ with $R = |\boldsymbol{r} - \boldsymbol{r'}|$, can be expanded as,

$$G(\boldsymbol{R}) = \left[\left(1 + \frac{ikR - 1}{k^2R^2}\right)\mathbb{I} + \left(\frac{3 - 3ikR - k^2R^2}{k^2R^2}\right)\frac{\boldsymbol{R} \bigotimes \boldsymbol{R}}{R^2}\right]\frac{\mathrm{e}^{ikR}}{4\pi R}, \tag{C.15}$$

where $\bigotimes$ indicates the tensor product. Investigating the behaviour of the function when evaluated at its origin, as R approaches zero, we are left with only the first set of terms on the right-hand side of Eq. (C.15), and by expanding the exponential function as a power series ($\exp(ikR) = 1 + ikR + (1/2)(ikR)^2 + (1/6)(ikR)^3 + \ldots$) we find that [224],

$$G(\boldsymbol{R}) \lim_{R\to 0} = \frac{1}{4\pi}\left(-\frac{1}{k^2R^3} + \frac{1}{2R} + \frac{2ik}{3} + \mathcal{O}(R)\ldots\right)\mathbb{I}. \tag{C.16}$$

We observe that the function is non-uniformly convergent in this limit, and that the only term which does not go to zero or infinity is the leading imaginary term. This result is very useful when we come to calculate the spontaneous decay rate of the current source (dipole or other emitter of finite extent).

The particular solution for the magnetic field, corresponding to Eq. (C.10), induced by the source current, is,

$$\boldsymbol{H}(\boldsymbol{r}) = \int_V [\nabla \times G(\boldsymbol{r}, \boldsymbol{r'})] \cdot \boldsymbol{J}(\boldsymbol{r'}) \mathrm{d}V(\boldsymbol{r'}). \tag{C.17}$$

Due to the duality of the electromagnetic fields as described by Maxwell, the propagation of the magnetic field from an electric source current can be determined through the curl of the electric Green's function, Eq. (C.13), which can be expanded as [223], with $\hat{\boldsymbol{R}} = \boldsymbol{R}/R$,

$$\nabla \times G(\boldsymbol{R}) = \left(ik - \frac{1}{R}\right) \frac{\mathrm{e}^{ikR}}{4\pi R} \left(\hat{\boldsymbol{R}} \times \mathbb{I}\right). \tag{C.18}$$

This tensor function is also singular when evaluated at its origin, but is anti-symmetric due to the term $\hat{\boldsymbol{R}} \times \mathbb{I}$.

We have thus far considered only fields and functions related to electric current sources. A similar approach can be used to find the Green's function for magnetic sources, starting from the magnetic wave equation,

$$\nabla \times \frac{1}{\epsilon_r} \nabla \times \boldsymbol{H} - \left(\frac{\omega}{c}\right)^2 \mu_r \boldsymbol{H} = \nabla \times \frac{\boldsymbol{J}}{\epsilon_r}, \tag{C.19}$$

and finding the solution to the equivalent wave equation for the magnetic Green's function G^M,

$$\nabla \times \frac{1}{\epsilon_r} \nabla \times G^M(\boldsymbol{r}, \boldsymbol{r'}) - \left(\frac{\omega}{c}\right)^2 \mu_r G^M(\boldsymbol{r}, \boldsymbol{r'}) = \mathbb{I}\delta(\boldsymbol{r} - \boldsymbol{r'}). \tag{C.20}$$

The magnetic Green's function is formally the same as the electric function, however different conditions are applied for magnetic sources at boundaries. Fortunately, we can obtain the expressions for the magnetic sources simply by exchanging $\boldsymbol{E} \Rightarrow \boldsymbol{H}$, $\boldsymbol{H} \Rightarrow -\boldsymbol{E}$ and $\mu_0\mu_r \Leftrightarrow \epsilon_0\epsilon_r$ in the electric source expressions [122], for any of the Green's functions described in this Section.

C.2 Green's functions for planarly layered media

For planarly layered media, the dyadic Green's function describing the propagation of electric and magnetic fields in an inhomogeneous medium must include terms describing the reflection and transmission of the *primary* fields at interfaces. The description of these additional *secondary* fields can be obtained by expanding the homogeneous Green's function in terms of plane waves, and applying the Fresnel coefficients to find the amplitudes of these waves at each interface. Here, we provide a treatment for the simplest case: a dipole radiating above a half-space. This case is very useful, as it can be effectively used to describe emitters and scatterers suspended on a supporting substrate, or as an approximation for nano-cavities in which the base is a thin layer of a lossy material.

We begin by considering the dyadic Green's function for a homogeneous medium, which we derived in the previous section (Eq. C.13). Assuming that the source is located at the origin ($\boldsymbol{r'} = 0$), and using $R = \sqrt{x^2 + y^2 + z^2}$, the Weyl identity for the scalar Green's function can be used to expand the spherical wave function as a linear superposition of plane waves,

$$\frac{\mathrm{e}^{ikR}}{R} = \frac{i}{2\pi} \iint_{-\infty}^{+\infty} \frac{\mathrm{e}^{i(k_x x + k_y y + k_z |z|)}}{k_z} \mathrm{d}k_x \mathrm{d}k_y, \tag{C.21}$$

with $k = \sqrt{k_x^2 + k_y^2 + k_z^2}$. This expression is only valid for (slightly) lossy dielectrics and so we require that both $\mathrm{Im}(k_z) > 0$ and $\mathrm{Re}(k_z) > 0$ for the integrals to converge [223] in a homogeneous medium. Using the Weyl identity, it is possible to obtain the Fourier integral form of Eq. (C.13), assuming an isotropic homogeneous medium [122],

$$G(\boldsymbol{r}, \boldsymbol{r'}) = \frac{i}{8\pi^2} \iint_{-\infty}^{+\infty} \frac{\mathrm{d}k_x \mathrm{d}k_y}{k^2 k_z} \begin{pmatrix} k^2 - k_x^2 & -k_x k_y & \mp k_x k_z \\ -k_x k_y & k^2 - k_y^2 & \mp k_y k_z \\ \mp k_x k_z & \mp k_y k_z & k^2 - k_z^2 \end{pmatrix} \mathrm{e}^{i(k_x x + k_y y + k_z |z|)}. \tag{C.22}$$

Here, the upper sign is for fields evaluated with $z > 0$ and the lower sign is for $z < 0$ (*i.e.* above and below the dipole position), hence the integral is defined in

a fixed plane with z constant. This form of integral is called an angular spectrum representation, as the spherical dipole fields are represented by a spectrum of plane and evanescent waves[1].

The reflected and transmitted wave Fresnel coefficients for a single interface are found using the material properties, with the layers above and below the interface indexed as 1 and 2 respectively,

$$r^s = \frac{\mu_{r_2} k_{z_1} - \mu_{r_1} k_{z_2}}{\mu_{r_2} k_{z_1} + \mu_{r_1} k_{z_2}} \qquad r^p = \frac{\epsilon_{r_2} k_{z_1} - \epsilon_{r_1} k_{z_2}}{\epsilon_{r_2} k_{z_1} + \epsilon_{r_1} k_{z_2}} \tag{C.23}$$

$$t^s = \frac{2\mu_{r_2} k_{z_1}}{\mu_{r_2} k_{z_1} + \mu_{r_1} k_{z_2}} \qquad t^p = \frac{2\epsilon_{r_2} k_{z_1}}{\epsilon_{r_2} k_{z_1} + \epsilon_{r_1} k_{z_2}}. \tag{C.24}$$

Using these coefficients, we can write an expression for the reflected part of the homogeneous Green's function, assuming that the dipole is in the upper half-space, where $\boldsymbol{r'} = (x', y'z')$ with both $z, z' > 0$, where we can decompose Eq. (C.22) in terms of the s-polarized (TE) and p-polarized (TM) waves, which are completely decoupled [122],

$$G^R(\boldsymbol{r}, \boldsymbol{r'}) = \frac{i}{8\pi^2} \int_{-\infty}^{+\infty}\!\!\!\int [M^s + M^p]\, \mathrm{e}^{i\left(k_x(x-x') + k_y(y-y') + k_{z_1}(z+z')\right)} \mathrm{d}\boldsymbol{k}_{||}, \tag{C.25}$$

$$M^s = \frac{r^s}{k_{z_1} k_{||}^2} \begin{pmatrix} k_y^2 & -k_x k_y & 0 \\ -k_x k_y & k_x^2 & 0 \\ 0 & 0 & 0 \end{pmatrix}, \tag{C.26}$$

$$M^p = \frac{-r^p}{k_1^2 k_{||}^2} \begin{pmatrix} k_x^2 k_{z_1} & k_x k_y k_{z_1} & k_x k_{||}^2 \\ k_x k_y k_{z_1} & k_y^2 k_{z_1} & k_y k_{||}^2 \\ -k_x k_{||}^2 & -k_y k_{||}^2 & -k_{||}^4 / k_{z_1} \end{pmatrix}, \tag{C.27}$$

with the two-dimensional transverse wave vector $\boldsymbol{k}_{||} = (k_x, k_y)$, and under the condition $\mathrm{Im}(k_{z_1}) \geq 0$.

We can write a similar Green's function for the transmitted wave, in the lower half space, using the transmitted Fresnel coefficients [122]. For a dipole above a multilayered planar interface, reflections from the lower layers (below the topmost interface) can be included by introducing generalized Fresnel coefficients. The amplitudes of the reflected and transmitted waves are given by recursive functions

[1] Evanescent waves decay exponentially away from the interface.

of the Fresnel coefficients at each interface [223], for an arbitrary number of thin[2] layers.

For homogeneous planar layers, each layer has cylindrical symmetry, and so by using rotation operators we can project the function into the arbitrarily defined $x-z$ plane [224, 225],

$$G^R(\boldsymbol{r},\boldsymbol{r'}) = \frac{i}{8\pi^2}\iint_{-\infty}^{+\infty}\frac{\mathrm{d}\boldsymbol{k}_{||}}{k_{z_1}}\left[S^{-1}(k_{||})M^{sp}(k_{||})S(k_{||})\right]\mathrm{e}^{i\boldsymbol{k}_{||}\cdot(\boldsymbol{\rho}-\boldsymbol{\rho'})+ik_{z_1}(z+z')}, \quad \text{(C.28)}$$

where $M^{sp}(k_{||}) = S(k_{||})\left(M^s + M^p\right)S^{-1}(k_{||})$ is the rotated coefficient matrix for both the TE and TM waves, which has only 5 non-zero components. The Jacobian rotation matrices are written as functions of the transverse (parallel to the interface) wave number [225],

$$S(k_{||}) = \frac{1}{k_{||}}\begin{pmatrix} k_x & k_y & 0 \\ -k_y & k_x & 0 \\ 0 & 0 & k_{||} \end{pmatrix}, \qquad S^{-1}(k_{||}) = \frac{1}{k_{||}}\begin{pmatrix} k_x & -k_y & 0 \\ k_y & k_x & 0 \\ 0 & 0 & k_{||} \end{pmatrix}. \quad \text{(C.29)}$$

We can then analytically solve the integral of the angular projection along φ, the angle between the transverse wave vector $\boldsymbol{k}_{||}$ and the x-axis, by making the substitution $\mathrm{d}k_x\mathrm{d}k_y = k_{||}\mathrm{d}k_{||}\mathrm{d}\varphi$,

$$G^R(\boldsymbol{r},\boldsymbol{r'}) = \frac{i}{4\pi}\int_0^{\infty}\frac{k_{||}\mathrm{d}k_{||}}{k_{z_1}}\mathrm{e}^{ik_{z_1}(z+z')}\int_0^{2\pi}\frac{\mathrm{d}\varphi}{2\pi}\left[S^{-1}(k_{||})M^{sp}(k_{||})S(k_{||})\right]\mathrm{e}^{ik_{||}|\boldsymbol{\rho}+\boldsymbol{\rho'}|\cos\varphi} \quad \text{(C.30)}$$

Since Sommerfeld's work on radiating dipole antennas above a lossy half-space [222], it has been known that spherical waves can be expanded as an integral summation of conical, or cylindrical, waves. Following this example, we simplify the angular integral in Eq. (C.30) using the expansion of a plane wave as a series of cylindrical waves, via the Jacobi-Anger expression,

$$\mathrm{e}^{ikR\cos\varphi} = J_0(kR) + 2\sum_{l=1}^{\infty} i^l J_l(kR)\cos(l\varphi), \quad \text{(C.31)}$$

where $J_n(z)$ are the "cylindrical" Bessel functions of the first kind, of order n and argument z. Using the relations $k_x/k \equiv \cos\varphi$ and $k_y/k \equiv \sin\varphi$, the terms

[2]With respect to the oscillation wavelength.

inside the rotated coefficient matrix M^{sp} can be written in terms of second order trigonometric functions and, with $\bar{\rho} = |\boldsymbol{\rho} + \boldsymbol{\rho'}|$, we can now expand the waves as,

$$\mathrm{e}^{ik_{||}\bar{\rho}\cos\varphi} \equiv J_0(k_{||}\bar{\rho}) + 2iJ_1(k_{||}\bar{\rho})\cos\varphi - 2J_2(k_{||}\bar{\rho})\cos 2\varphi. \tag{C.32}$$

Once we have used this expansion to solve the angular integral, we are left with a line integral over $k_{||}$ which can be efficiently calculated using adaptive quadrature techniques, such as the Gauss-Kronrod quadrature [226]. We note that the function G^R is highly singular, and one has to discretize the domain of integration to isolate the poles at $k_{||} = k_1$ and use the branch cuts at $k_{z_1} = \pm\sqrt{k_1^2 - k_{||}^2}$, in the domain where $k_{||} > k_1$[3], to maintain the radiation condition ($\mathrm{Im}(k_{z_1}) \geq 0$) and allow the integral to properly converge.

An expression for the reflected Green's function defining propagation of the magnetic field can also be obtained by taking the curl of Eq. (C.25), where the curl operator acts independently on each column of the Green's tensor with $\partial_x = ik_x$, $\partial_y = ik_y$ and $\partial_z = ik_{z_1}$, and then following the same projection and expansion procedure to simplify the integral. The rotated coefficient matrix for the magnetic field contains only 4 non-zero components, but it contains terms with third order trigonometric functions and so we must extend the cylindrical expansion in Eq. (C.32) in order to solve the angular integral.

An advantage of using the angular spectrum representation for the Green's functions is that an analytical far field form of these expressions can be readily obtained using the method of stationary phase [227]. In this model, only the plane wave propagating directly toward the far field evaluation point is considered, with wave vector aligned with the unit vector pointing in the direction of the far field position, as all other waves cancel out due to destructive interference. A list of these expressions can be found in Appendix D of Ref. [122].

For more complex geometries, such as an emitter embedded within a stratified medium, we have to include the (multiple) reflections from both the upper and lower layers in the Green's function [151], but the method applied is very similar to that which we have described here.

[3]When $k_{||} > k_1$ the longitudinal wave number k_{z_1} is entirely imaginary, representing evanescent waves.

Bibliography

[1] R. H. Ritchie, "Plasma losses by fast electrons in thin films," *Phys. Rev.*, vol. 106, pp. 874–881, 1957.

[2] C. J. Powell and J. B. Swan, "Origin of the Characteristic Electron Energy Losses in Aluminum," *Phys. Rev.*, vol. 115, pp. 869–875, 1959.

[3] C. J. Powell, "The origin of the characteristic electron energy losses in aluminium and magnesium," *J. Nucl. Energy C*, vol. 2, no. 1, p. 57, 1961.

[4] S. Kawata, *Near-Field Optics and Surface Plasmon Polaritons*. Berlin: Springer-Verlag, 1 ed., 2001.

[5] M. E. Stewart, C. R. Anderton, L. B. Thompson, J. Maria, S. K. Gray, J. A. Rogers, and R. G. Nuzzo, "Nanostructured plasmonic sensors," *Chem. Rev.*, vol. 108, no. 2, pp. 494–521, 2008.

[6] C. Valsecchi and A. G. Brolo, "Periodic metallic nanostructures as plasmonic chemical sensors," *Langmuir*, vol. 29, no. 19, pp. 5638–5649, 2013.

[7] P. Anger, P. Bharadwaj, and L. Novotny, "Enhancement and quenching of single-molecule fluorescence," *Phys. Rev. Lett.*, vol. 96, p. 113002, Mar 2006.

[8] S. Kühn, U. Håkanson, L. Rogobete, and V. Sandoghdar, "Enhancement of single-molecule fluorescence using a gold nanoparticle as an optical nanoantenna," *Phys. Rev. Lett.*, vol. 97, p. 017402, Jul 2006.

[9] G. C. Schatz and R. P. V. Duyne, "Electromagnetic mechanism of surface-enhanced spectroscopy," in *Handbook of Vibrational Spectroscopy* (J. M. Chalmers and P. R. Griffiths, eds.), Wiley, 2002.

[10] M. Moskovits, "Surface-enhanced raman spectroscopy: a brief retrospective," *J. Raman Spectrosc.*, vol. 36, no. 6-7, pp. 485–496, 2005.

[11] W. L. Barnes, A. Dereux, and T. W. Ebbesen, "Surface plasmon subwavelength optics," *Nature*, vol. 424, no. 6950, pp. 824–830, 2003.

[12] M. A. Noginov, G. Zhu, A. M. Belgrave, R. Bakker, V. M. Shalaev, E. E. Narimanov, S. Stout, E. Herz, T. Suteewong, and U. Wiesner, "Demonstration of a spaser-based nanolaser," *Nature*, vol. 460, no. 7259, pp. 1110–1112, 2009.

[13] M. W. Knight, H. Sobhani, P. Nordlander, and N. J. Halas, "Photodetection with active optical antennas," *Science*, vol. 332, no. 6030, pp. 702–704, 2011.

[14] J. Schuller, E. Barnard, W. Cai, Y. C. Jun, J. White, and M. Brongersma, "Plasmonics for extreme light concentration and manipulation," *Nat. Mater.*, vol. 9, pp. 193–204, 2010.

[15] Q. Zhao, J. Zhou, F. Zhang, and D. Lippens, "Mie resonance-based dielectric metamaterials," *Mater. Today*, vol. 12, no. 12, pp. 60–69, 2009.

[16] J. B. Pendry, D. Schuring, and D. R. Smith, "Controlling electromagnetic fields," *Science*, vol. 312, pp. 1780–1782, 2006.

[17] U. Kreibig and M. Vollmer, *Optical Properties of Metal Clusters*. Berlin: Springer-Verlag, 1 ed., 1995.

[18] K. L. Kelly, E. Coronado, L. L. Zhao, and G. C. Schatz, "The optical properties of metal nanoparticles: the influence of size, shape, and dielectric environment," *J. Phys. Chem. B*, vol. 107, no. 3, pp. 668–677, 2003.

[19] C. F. Bohren and D. R. Huffman, *Absorption and Scattering of Light by Small Particles*. Wiley, 1998.

[20] G. Mie, "Beiträge zur optik trüber medien, speziell kolloidaler metallösungen," *Ann. Phys.*, vol. 330, p. 377, 1908.

[21] R. Gans, "Über die form ultramikroskopischer goldteilchen," *Ann. Phys.*, vol. 342, no. 5, pp. 881–900, 1912.

[22] B. Gallinet, J. Butet, and O. J. F. Martin, "Numerical methods for nanophotonics: standard problems and future challenges," *Laser Photonics Rev.*, vol. 9, no. 6, pp. 577–603, 2015.

[23] F. Papoff and B. Hourahine, "Geometrical Mie theory for resonances in nanoparticles of any shape," *Opt. Express*, vol. 19, pp. 21432–21444, 2011.

[24] K. Imura, T. Nagahara, and H. Okamoto, "Near-field two-photon-induced photoluminescence from single gold nanorods and imaging of plasmon modes," *J. Phys. Chem. B*, vol. 109, no. 27, pp. 13214–13220, 2005.

[25] R. C. Dunn, "Near-field scanning optical microscopy," *Chem. Rev.*, vol. 99, no. 10, pp. 2891–2928, 1999.

[26] D. W. Pohl, "Optics at the nanometre scale," *Philos. Trans. A: Math. Phys. & Eng. Sci.*, vol. 362, no. 1817, pp. 701–717, 2004.

[27] E. Betzig, J. K. Trautman, T. D. Harris, J. S. Weiner, and R. L. Kostelak, "Breaking the diffraction barrier: Optical microscopy on a nanometric scale," *Science*, vol. 251, no. 5000, pp. 1468–1470, 1991.

[28] S. I. Bozhevolnyi, J. Beermann, and V. Coello, "Direct observation of localized second-harmonic enhancement in random metal nanostructures," *Phys. Rev. Lett.*, vol. 90, p. 197403, 2003.

[29] H. Okamoto and K. Imura, "Visualizing the optical field structures in metal nanostructures," *J. Phys. Chem. Lett.*, vol. 4, no. 13, pp. 2230–2241, 2013.

[30] E. J. R. Vesseur, R. de Waele, M. Kuttge, and A. Polman, "Direct observation of plasmonic modes in au nanowires using high-resolution cathodoluminescence spectroscopy," *Nano Lett.*, vol. 7, no. 9, pp. 2843–2846, 2007.

[31] M. W. Knight, L. Liu, Y. Wang, L. Brown, S. Mukherjee, N. S. King, H. O. Everitt, P. Nordlander, and N. J. Halas, "Aluminum plasmonic nanoantennas," *Nano Lett.*, vol. 12, no. 11, pp. 6000–6004, 2012.

[32] D. Rossouw, M. Couillard, J. Vickery, E. Kumacheva, and G. A. Botton, "Multipolar plasmonic resonances in silver nanowire antennas imaged with a subnanometer electron probe," *Nano Lett.*, vol. 11, no. 4, pp. 1499–1504, 2011.

[33] B. S. Guiton, V. Iberi, S. Li, D. N. Leonard, C. M. Parish, P. G. Kotula, M. Varela, G. C. Schatz, S. J. Pennycook, and J. P. Camden, "Correlated optical measurements and plasmon mapping of silver nanorods," *Nano Lett.*, vol. 11, no. 8, pp. 3482–3488, 2011.

[34] I. Alber, W. Sigle, S. Müller, R. Neumann, O. Picht, M. Rauber, P. A. van Aken, and M. E. Toimil-Molares, "Visualization of multipolar longitudinal and transversal surface plasmon modes in nanowire dimers," *ACS Nano*, vol. 5, no. 12, pp. 9845–9853, 2011.

[35] A. L. Koh, A. I. Fernndez-Domnguez, D. W. McComb, S. A. Maier, and J. K. W. Yang, "High-resolution mapping of electron-beam-excited plasmon modes in lithographically defined gold nanostructures," *Nano Lett.*, vol. 11, no. 3, pp. 1323–1330, 2011.

[36] D. J. Tannor and S. A. Rice, "Control of selectivity of chemical reaction via control of wave packet evolution," *J. Chem. Phys.*, vol. 83, no. 10, pp. 5013–5018, 1985.

[37] P. Brumer and M. Shapiro, "Control of unimolecular reactions using coherent-light," *Chem. Phys. Lett.*, vol. 126, no. 6, pp. 541–546, 1986.

[38] M. Stockman, S. Faleev, and D. Bergman, "Coherent control of femtosecond energy localization in nanosystems," *Phys. Rev. Lett.*, vol. 88, p. 067402, 2002.

[39] M. Sukharev, T. Seideman, R. Gordon, A. Salomon, and Y. Prio, "Phase and polarization control as a route to plasmonic nanodevices," *Nano Lett.*, vol. 6, pp. 715–719, 2006.

[40] H. Noh, Y. Chong, A. D. Stone, and H. Cao, "Perfect coupling of light to surface plasmons by coherent absorption," *Phys. Rev. Lett.*, vol. 108, p. 186805, 2012.

[41] R. Pierrat, C. Vandenbem, M. Fink, and R. Carminati, "Subwavelength focusing inside an open disordered medium by time reversal at a single point antenna," *Phys. Rev. A*, vol. 87, p. 041801, 2013.

[42] S. G. Rodrigo, H. Harutyunyan, and L. Novotny, "Coherent control of light scattering from nanostructured materials by second-harmonic generation," *Phys. Rev. Lett.*, vol. 110, p. 177405, 2013.

[43] L. Cao, R. Nome, J. Montgomery, S. Gray, and N. Scherer, "Controlling plasmonic wave packets in silver nanowires," *Nano Lett.*, vol. 10, pp. 3389–33394, 2010.

[44] M. Martin Aeschlimann, M. Bauer, D. Bayer, T. Tobias Brixner, F. Garcia de Abajo, W. Pfeiffer, M. Rohmer, C. Spindler, and F. Felix Steeb, "Adaptive subwavelength control of nano-optical fields," *Nature*, vol. 446, pp. 301–304, 2007.

[45] A. Kubo, K. Onda, H. Petek, Z. Sun, Y. Jung, and H. Kim, "Femtosecond imaging of surface plasmon dynamics in a nanostructured silver film," *Nano Lett.*, vol. 5, pp. 1123–1127, 2005.

[46] S. Choi, D. Park, C. Lienau, M. S. Jeong, C. C. Byeon, D.-K. Ko, and D. S. Kim, "Femtosecond phase control of spatial localization of the optical near-field in a metal nanoslit array," *Opt. Express*, vol. 16, no. 16, pp. 12075–12083, 2008.

[47] M. Aeschlimann, M. Bauer, D. Bayer, T. Brixner, S. Cunovic, F. Dimler, A. Fischer, W. Pfeiffer, M. Rohmer, C. Schneider, F. Steeb, C. Strüber,

and D. V. Voronine, "Spatiotemporal control of nanooptical excitations," *P. Natl. Acad. Sci.*, vol. 107, no. 12, pp. 5329–5333, 2010.

[48] M. Abb, P. Albella, J. Aizpurua, and O. Muskens, "All-optical control of a single plasmonic nanoantenna-ITO hybrid," *Nano Lett.*, vol. 11, pp. 2457–2463, 2011.

[49] J. Zhang, K. MacDonald, and N. Zheludev, "Controlling light-with-light without nonlinearity," *Light: Sci. Appl.*, vol. 1, p. e18, 2012.

[50] M. I. Stockman, "Nanoplasmonics: past, present, and glimpse into future," *Opt. Express*, vol. 19, no. 22, pp. 22029–22106, 2011.

[51] B. Hourahine and F. Papoff, "Optical control of scattering, absorption and lineshape in nanoparticles," *Opt. Express*, vol. 21, pp. 20322–20333, 2013.

[52] S. V. Gaponenko and D. V. Guzatov, "Possible rationale for ultimate enhancement factor in single molecule raman spectroscopy," *Chem. Phys. Lett.*, vol. 477, pp. 411–414, 2009.

[53] M. D. Doherty, A. Murphy, R. J. Pollard, and P. Dawson, "Surface-enhanced raman scattering from metallic nanostructures: Bridging the gap between the near-field and far-field responses," *Phys. Rev. X*, vol. 3, p. 011001, 2013.

[54] Y. Yang, J. M. Callahan, T.-H. Kim, A. S. Brown, and H. O. Everitt, "Ultraviolet nanoplasmonics: A demonstration of surface-enhanced raman spectroscopy, fluorescence, and photodegradation using gallium nanoparticles," *Nano Lett.*, vol. 13, no. 6, pp. 2837–2841, 2013.

[55] J. Ren, Y. Gu, D. Zhao, F. Zhang, T. Zhang, and Q. Gong, "Evanescent-vacuum-enhanced photon-exciton coupling and fluorescence collection," *Phys. Rev. Lett.*, vol. 118, p. 073604, 2017.

[56] P. Michler, A. Kiraz, C. Becher, W. V. Schoenfeld, P. M. Petroff, L. Zhang, E. Hu, and A. Imamoglu, "A quantum dot single-photon turnstile device," *Science*, vol. 290, no. 5500, pp. 2282–2285, 2000.

[57] M. Gratzel, "Photoelectrochemical cells," *Nature*, vol. 414, pp. 338–344, 2001.

[58] R. Chikkaraddy, X. Zheng, F. Benz, L. J. Brooks, B. de Nijs, C. Carnegie, M.-E. Kleemann, J. Mertens, R. W. Bowman, G. A. E. Vandenbosch, V. V. Moshchalkov, and J. J. Baumberg, "How ultranarrow gap symmetries control plasmonic nanocavity modes: From cubes to spheres in the nanoparticle-on-mirror," *ACS Photonics*, vol. 4, no. 3, pp. 469–475, 2017.

[59] G. Zengin, M. Wersäll, S. Nilsson, T. Antosiewicz, M. Käll, and T. Shegai, "Realizing strong light-matter interactions between single-nanoparticle plasmons and molecular excitons at ambient conditions," *Phys. Rev. Lett.*, vol. 114, 2015.

[60] R. Chikkaraddy, B. de Nijs, F. Benz, S. J. Barrow, O. A. Scherman, E. Rosta, A. Demetriadou, P. Fox, O. Hess, and J. J. Baumberg, "Single-molecule strong coupling at room temperature in plasmonic nanocavities," *Nature*, vol. 535, pp. 127–130, 2016.

[61] M. J. McClain, A. E. Schlather, E. Ringe, N. S. King, L. Liu, A. Manjavacas, M. W. Knight, I. Kumar, K. H. Whitmire, H. O. Everitt, P. Nordlander, and N. J. Halas, "Aluminum nanocrystals," *Nano Lett.*, vol. 15, pp. 2751–2755, 2015.

[62] S. K. Jha, N. Mojarad, M. Agio, J. F. Löffler, and Y. Ekinci, "Enhancement of the intrinsic fluorescence of adenine using aluminum nanoparticle arrays," *Opt. Express*, vol. 23, pp. 24719–24729, 2015.

[63] N. S. King, L. Liu, X. Yang, B. Cerjan, H. O. Everitt, P. Nordlander, and N. J. Halas, "Fano resonant aluminum nanoclusters for plasmonic colorimetric sensing," *Nano Lett.*, vol. 9, pp. 10628–10636, 2015.

[64] C. Jordan, "Essai sur la géométrie à n dimension," *B. Soc. Math. Fr.*, vol. 3, pp. 103–174, 1875.

[65] A. Knyazev, A. Jujusnashvili, and M. Argentati, "Angles between Infinite Dimensional Subspaces with Applications to the Rayleigh-Ritz and Alternating Projectors Methods," *Journ. of Func. Analys.*, vol. 259, pp. 1323–1345, 2010.

[66] A. Doicu, T. Wriedt, and Y. Eremin, *Light Scattering by Systems of Particles*. Springer, 2006.

[67] K. Holms, B. Hourahine, and F. Papoff, "Calculation of internal and scattered fields of axisymmetric nanoparticles at any point in space," *J. Opt. A: Pure Appl. Opt.*, vol. 11, p. 054009, May 2009.

[68] A. Aydin and A. Hizal, "On the completeness of the spherical vector wave functions," *Journ. Math. Anal. and Appl.*, vol. 117, p. 428, 1986.

[69] V. S. Vladimirov, *Equations of mathematical physics*. Moscow: MIR, 1984.

[70] A. Doicu and T. Wriedt, "Calculation of the t matrix in the null-field method with discrete sources," *J. Opt. Soc. Am. A*, vol. 16, pp. 2539–2544, OCT 1999.

[71] A. Doicu and T. Wriedt, "Extended boundary condition method with multipole sources located in the complex plane," *Opt. Commun.*, vol. 139, pp. 85–91, 1997.

[72] T. Rother, M. Kahnert, A. Doicu, and J. Wauer, "Surface Green's Function of the Helmholtz Equation in Spherical Coordinates," *Prog. Electromag. Res.*, vol. 38, pp. 47–95, 2002.

[73] S. Silver, ed., *Microwave antenna theory and design*. New York: McGraw-Hill, 1949.

[74] C. Müller, ed., *Grundprobleme der mathematischen Theorie elektromagnetischer Schwingungen*. Berlin: Springer, 1957.

[75] A. Knyazev and M. Argentati, "Principal angles between subspaces in an A-based scalar product: algorithms and perturbation estimates," *SIAM J. Sci. Comput.*, vol. 23, no. 6, pp. 2008–2040, 2002.

[76] D. McArthur, B. Hourahine, and F. Papoff, "Evaluation of E. M. fields and energy transport in metallic nanoparticles with near field excitation," *Phys. Sci. Int. Jour.*, vol. 4, no. 4, pp. 564–575, 2014.

[77] E. Hannan, "The general theory of canonical correlation and its relation to functional analysis," *J. Aust. Math. Soc.*, vol. 2, pp. 229–242, 1961/1962.

[78] J. D. Jackson, *Classical electrodynamics*. New York: Wiley, 1999.

[79] B. F. Farrell and P. J. Ioannou, "Generalized stability theory. part i: Autonomous operators," *Journ. of Atm. Sc.*, vol. 53, pp. 2025–2040, 1996.

[80] B. Hourahine, K. Holms, and F. Papoff, "Accurate near and far field determination for non spherical particles from Mie-type theory," *J. Phys.: Conf. Ser.*, vol. 367, p. 012010, 2012.

[81] G. New, "The origin of excess noise," *Journ. Mod. Optics*, vol. 42, pp. 799–810, 1995.

[82] W. J. Firth and A. Yao, "Giant excess noise and transient gain in misaligned laser cavities," *Phys. Rev. Lett.*, vol. 95, p. 073903, 2005.

[83] F. Papoff, G. D'Alessandro, and G.-L. Oppo, "State dependent pseudoresonances and excess noise," *Phys. Rev. Lett.*, vol. 100, p. 123905, 2008.

[84] M. I. Tribelsky and B. S. Lukyanchuk, "Anomalous light scattering by small particles," *Phys Rev. Lett.*, vol. 97, 2006.

[85] J. A. Stratton and L. J. Chu, "Diffraction theory of electromagnetic waves," *Phys. Rev.*, vol. 56, pp. 99–107, 1939.

[86] G. Roll and G. Schweiger, "Geometrical optics model of Mie resonances," *J. Opt. Soc. Am. A*, vol. 17, pp. 1301–1311, 2000.

[87] Y. Han and Z. Wu, "Scattering of a spheroidal particle illuminated by a gaussian beam," *Appl. Optics*, vol. 40, pp. 2501–2509, 2001.

[88] M. I. Mishchenko, J. H. Hovernier, and L. D. Travis, eds., *Light scattering by nonspherical particles: Theory, Measurements and Applications*. Academic Press, 2000.

[89] P. G. Etchegoin, E. C. Le Ru, and M. Meyer, "An analytic model for the optical properties of gold," *J. Chem. Phys.*, vol. 125, p. 164705, 2006.

[90] P. G. Etchegoin, E. C. Le Ru, and M. Meyer, "Erratum: "An analytic model for the optical properties of gold" [J. Chem. Phys. 125, 164705 (2006)]," *J. Chem. Phys.*, vol. 127, p. 189901, 2007.

[91] H. Okamoto and K. Imura, "Near field optical imaging of enhanced electric fields and plasmon waves in metal nanostructures," *Prog. Surf. Sci.*, vol. 84, pp. 199–229, 2009.

[92] J. E. Inglesfield, "A method of embedding," *J. Phys. C*, vol. 14, p. 3795, 1981.

[93] G. A. Baraff and M. M Schlüter, "The LCAO approach to the embedding problem," *J. Phys. C*, vol. 19, p. 4383, 1986.

[94] J. E. Inglesfield, "The embedding method for electromagnetics," *J. Phys. A*, vol. 31, p. 8495, 1998.

[95] G. Gouesbet and G. Grehan, "Generalized Lorenz-Mie theory for assemblies of spheres and aggregates," *J. Opt. A*, vol. 1, p. 706, 1999.

[96] F. J. G. de Abajo, "Nonlocal effects in the plasmons of strongly interacting nanoparticles, dimers, and waveguides," *J. Phys. Chem. C*, vol. 112, no. 46, pp. 17983–17987, 2008.

[97] P. Ginzburg and A. V. Zayats, "Localized surface plasmon resonances in spatially dispersive nano-objects: Phenomenological treatise," *ACS Nano*, vol. 7, no. 5, pp. 4334–4342, 2013.

[98] J. W. Pitera, M. Falta, and W. F. van Gunsteren, "Dielectric properties of proteins from simulation: The effects of solvent, ligands, pH, and temperature," *Biophys. J.*, vol. 80, pp. 2546–2555, 2001.

[99] E. Abbe, "Beiträge zur theorie des mikroskops und der mikroskopischen wahrnehmung," *Arch. Mikrosk. Anat.*, vol. 9, pp. 413–418, Dec 1873.

[100] J. W. Goodman, *Introduction to Fourier Optics*. New York: AMcGraw-Hil, 1968.

[101] K. Imura, K. Ueno, H. Misawa, H. Okamoto, D. McArthur, B. Hourahine, and F. Papoff, "Plasmon modes in single gold nanodiscs," *Opt. Express*, vol. 22, pp. 12189–12199, 2014.

[102] S. Webster, D. A. Smith, and D. N. Batchelder, "Raman microscopy using a scanning near-field optical probe," *Vibrat. Spec.*, vol. 18, no. 1, pp. 51 – 59, 1998.

[103] K. Kneipp, H. Kneipp, P. Corio, S. D. M. Brown, K. Shafer, J. Motz, L. T. Perelman, E. B. Hanlon, A. Marucci, G. Dresselhaus, and M. S. Dresselhaus, "Surface-enhanced and normal stokes and anti-stokes raman spectroscopy of single-walled carbon nanotubes," *Phys. Rev. Lett.*, vol. 84, pp. 3470–3473, Apr 2000.

[104] U. C. Fischer and D. W. Pohl, "Observation of single-particle plasmons by near-field optical microscopy," *Phys. Rev. Lett.*, vol. 62, pp. 458–461, Jan 1989.

[105] R. Esteban, R. Vogelgesang, J. Dorfmüller, A. Dmitriev, C. Rockstuhl, C. Etrich, and K. Kern, "Direct near-field optical imaging of higher order plasmonic resonances," *Nano Lett.*, vol. 8, no. 10, pp. 3155–3159, 2008.

[106] E. H. Synge, "Xxxviii. a suggested method for extending microscopic resolution into the ultra-microscopic region," *Philos. Mag.*, vol. 6, no. 35, pp. 356–362, 1928.

[107] E. A. Ash and G. Nicholls, "Super-resolution aperture scanning microscope," *Nature*, vol. 237, no. 5357, pp. 510–512, 1972.

[108] G. Binnig, H. Rohrer, C. Gerber, and E. Weibel, "Tunneling through a controllable vacuum gap," *Appl. Phys. Lett.*, vol. 40, no. 2, pp. 178–180, 1982.

[109] D. W. Pohl, W. Denk, and M. Lanz, "Optical stethoscopy: Image recording with resolution $\lambda/20$," *Appl. Phys. Lett.*, vol. 44, no. 7, pp. 651–653, 1984.

[110] A. Lewis, M. Isaacson, A. Harootunian, and A. Muray, "Development of a 500 Å spatial resolution light microscope," *Ultramicroscopy*, vol. 13, no. 3, pp. 227 – 231, 1984.

[111] E. Betzig, P. L. Finn, and J. S. Weiner, "Combined shear force and near-field scanning optical microscopy," *Appl. Phys. Lett.*, vol. 60, pp. 2484–2486, May 1992.

[112] R. Toledo-Crow, P. Yang, Y. Chen, and M. Vaez-Iravani, "Near-field differential scanning optical microscope with atomic force regulation," *Appl. Phys. Lett.*, vol. 60, no. 24, pp. 2957–2959, 1992.

[113] L. Novotny, D. W. Pohl, and B. Hecht, "Scanning near-field optical probe with ultrasmall spot size," *Opt. Lett.*, vol. 20, pp. 970–972, May 1995.

[114] Y. Inouye and S. Kawata, "Near-field scanning optical microscope with a metallic probetip," *Opt. Lett.*, vol. 19, pp. 159–161, Feb 1994.

[115] H. G. Frey, F. Keilmann, A. Kriele, and R. Guckenberger, "Enhancing the resolution of scanning near-field optical microscopy by a metal tip grown on an aperture probe," *Appl. Phys. Lett.*, vol. 81, no. 26, pp. 5030–5032, 2002.

[116] R. C. Reddick, R. J. Warmack, and T. L. Ferrell, "New form of scanning optical microscopy," *Phys. Rev. B*, vol. 39, pp. 767–770, Jan 1989.

[117] D. Courjon, K. Sarayeddine, and M. Spajer, "Scanning tunneling optical microscopy," *Opt. Commun.*, vol. 71, no. 1, pp. 23 – 28, 1989.

[118] J. Kim and K.-B. Song, "Recent progress of nano-technology with nsom," *Micron*, vol. 38, no. 4, pp. 409 – 426, 2007. Microscopy of Nanostructures.

[119] J.-J. Greffet and R. Carminati, "Image formation in near-field optics," *Prog. Surf. Sci.*, vol. 56, no. 3, pp. 133 – 237, 1997.

[120] C. Girard and A. Dereux, "Near-field optics theories," *Rep. Prog. Phys.*, vol. 59, no. 5, p. 657, 1996.

[121] T. Chen, B. Dong, K. Chen, F. Zhao, X. Cheng, C. Ma, S. Lee, P. Zhang, S. H. Kang, J. W. Ha, W. Xu, and N. Fang, "Optical super-resolution imaging of surface reactions," *Chem. Rev.*, vol. 117, no. 11, pp. 7510–7537, 2017.

[122] L. Novotny and B. Hecht, *Principles of Nano-Optics*. Cambridge University Press, second ed., 2012.

[123] K. Imura and H. Okamoto, "Reciprocity in scanning near-field optical microscopy: illumination and collection modes of transmission measurements," *Opt. Lett.*, vol. 31, pp. 1474–1476, May 2006.

[124] L. Novotny and C. Hafner, "Light propagation in a cylindrical waveguide with a complex, metallic, dielectric function," *Phys. Rev. E*, vol. 50, pp. 4094–4106, Nov 1994.

[125] H. A. Bethe, "Theory of diffraction by small holes," *Phys. Rev.*, vol. 66, p. 163182, 1944.

[126] G. Kirchhoff, "Zur Theorie der Lichtstrahlen," *Ann. Phys.*, vol. 254, pp. 663–695, 1883.

[127] W. R. Smythe, "The double current sheet in diffraction," *Phys. Rev.*, vol. 72, pp. 1066–1070, 1947.

[128] C. J. Bouwkamp, "On Bethe's theory of diffraction by small holes," *Philips Res. Reps.*, vol. 5, pp. 321–332, 1950.

[129] C. J. Bouwkamp, "Diffraction theory," *Rep. Prog. Phys.*, vol. 17, no. 1, p. 35, 1954.

[130] J. Babinet, "Mémoires d'optique météorologique," *Compt. Rend. Acad. Sci.*, vol. 4, p. 638, 1837.

[131] C. J. Bouwkamp, "On the diffraction of electromagnetic waves by small circular disks and holes," *Philips Res. Reps.*, vol. 5, pp. 401–422, 1950.

[132] C. Obermüller and K. Karrai, "Far field characterization of diffracting circular apertures," *Appl. Phys. Lett.*, vol. 67, no. 23, pp. 3408–3410, 1995.

[133] A. Drezet, J. C. Woehl, and S. Huant, "Diffraction by a small aperture in conical geometry: Application to metal-coated tips used in near-field scanning optical microscopy," *Phys. Rev. E*, vol. 65, p. 046611, Apr 2002.

[134] O. J. F. Martin, C. Girard, and A. Dereux, "Generalized field propagator for electromagnetic scattering and light confinement," *Phys. Rev. Lett.*, vol. 74, pp. 526–529, Jan 1995.

[135] A. Drezet, M. J. Nasse, S. Huant, and J. C. Woehl, "The optical near-field of an aperture tip," *Europhys. Lett.*, vol. 66, no. 1, p. 41, 2004.

[136] K. Imura, T. Nagahara, and H. Okamoto, "Near-field optical imaging of plasmon modes in gold nanorods," *J. Chem. Phys.*, vol. 122, no. 15, 2005.

[137] C. Sönnichsen, T. Franzl, T. Wilk, G. von Plessen, J. Feldmann, O. Wilson, and P. Mulvaney, "Drastic reduction of plasmon damping in gold nanorods," *Phys. Rev. Lett.*, vol. 88, p. 077402, Jan 2002.

[138] P. Hanarp, M. Käll, and D. S. Sutherland, "Optical properties of short range ordered arrays of nanometer gold disks prepared by colloidal lithography," *J. Phys. Chem. B*, vol. 107, no. 24, pp. 5768–5772, 2003.

[139] C. Langhammer, B. Kasemo, and I. Zorić, "Absorption and scattering of light by Pt, Pd, Ag, and Au nanodisks: Absolute cross sections and branching ratios," *J. Chem. Phys.*, vol. 126, no. 19, 2007.

[140] K. Ueno, S. Juodkazis, V. Mizeikis, K. Sasaki, and H. Misawa, "Spectrally-resolved atomic-scale length variations of gold nanorods," *J. Am. Chem. Soc.*, vol. 128, no. 44, pp. 14226–14227, 2006.

[141] K. Imura, K. Ueno, H. Misawa, and H. Okamoto, "Anomalous light transmission from plasmonic-capped nanoapertures," *Nano Lett.*, vol. 11, no. 3, pp. 960–965, 2011.

[142] K. Imura, T. Nagahara, and H. Okamoto, "Characteristic near-field spectra of single gold nanoparticles," *Chem. Phys. Lett.*, vol. 400, no. 46, pp. 500 – 505, 2004.

[143] J. A. Veerman, M. F. Garcia-Parajo, L. Kuipers, and N. F. Van Hulst, "Single molecule mapping of the optical field distribution of probes for near-field microscopy," *J. Microsc.*, vol. 194, no. 2-3, pp. 477–482, 1999.

[144] F.-P. Schmidt, H. Ditlbacher, U. Hohenester, A. Hohenau, F. Hofer, and J. R. Krenn, "Dark plasmonic breathing modes in silver nanodisks," *Nano Lett.*, vol. 12, no. 11, pp. 5780–5783, 2012.

[145] A. Taflove and S. C. Hagness, *Computational Electrodynamics: The Finite Difference Time-Domain Method*. Boston, MA: Artech House Publishers, 1995.

[146] B. T. Draine and P. J. Flatau, "Discrete-dipole approximation for scattering calculations," *J. Opt. Soc. Am. A*, vol. 11, pp. 1491–1499, Apr 1994.

[147] B. Hourahine and F. Papoff, "The geometrical nature of optical resonances: from a sphere to fused dimer nanoparticles," *Meas. Sci. Technol.*, vol. 23, p. 084002, 2012.

[148] A. Doicu, Y. Eremin, and T. Wreidt, *Acoustic and Electromagnetic Scattering Analysis Using Discrete Sources*. Academic Press, 2000.

[149] E. A. Coronado and G. C. Schatz, "Surface plasmon broadening for arbitrary shape nanoparticles: A geometrical probability approach," *J. Chem. Phys.*, vol. 119, no. 7, pp. 3926–3934, 2003.

[150] "Optical constants of BK7." `https://refractiveindex.info`.

[151] M. Paulus, P. Gay-Balmaz, and O. J. F. Martin, "Accurate and efficient computation of the Green's tensor for stratified media," *Phys. Rev. E*, vol. 62, pp. 5797–5807, Oct 2000.

[152] F. Papoff, D. Mcarthur, and B. Hourahine, "Coherent control of radiation patterns of nonlinear multiphoton processes in nanoparticles," *Sci. Rep.*, vol. 5, p. 12040, 2015.

[153] D. McArthur, B. Hourahine, and F. Papoff, "Dataset on coherent control of fields and induced currents in nonlinear multiphoton processes in a nanosphere," *Sci. Data*, vol. 2, p. 150064, 2015.

[154] D. McArthur, B. Hourahine, and F. Papoff, "Coherent control of plasmons in nanoparticles with nonlocal response," *Opt. Comm.*, vol. 382, pp. 258 – 265, 2017.

[155] C. Kittel, *Introduction to solid state physics*, ch. 14. John Wiley & Sons, 8$^{\text{th}}$ ed., 2004.

[156] A. Melnyk and M. J. Harrison, "Theory of optical excitation of plasmons in metals," *Phys. Rev. B*, vol. 2, no. 4, p. 835, 1970.

[157] R. Ruppin, "Optical properties of small metal spheres," *Phys. Rev. B*, vol. 11, pp. 2871–2876, 1975.

[158] C. David and F.-J. G. de Abajo, "Spatial nonlocality in the optical response of metal nanoparticles," *J. Phys. Chem.*, vol. 115, pp. 19470–19475, 2011.

[159] C. Cirací, R. T. Hill, J. J. Mock, Y. Urzhumov, A. I. Fernández-Domínguez, S. A. Maier, J. B. Pendry, A. Chilkoti, and D. R. Smith, "Probing the

ultimate limits of plasmonic enhancement," *Science*, vol. 337, pp. 1072–1074, 2012.

[160] A. Moreau, C. Cirací, and R. D. Smith, "Impact of nonlocal response on metallodielectric multilayers and optical patch antennas," *Phys. Rev. B*, vol. 87, p. 045401, 2013.

[161] T. Christensen, W. Yan, S. Raza, A.-P. Jauho, N. A. Mortensen, and M. Wubs, "Nonlocal response of metallic nanospheres probed by light, electrons, and atoms," *ACS Nano*, vol. 2, pp. 1745–1758, 2014.

[162] A. D. Boardman, *Electromagnetic Surface Modes*. Wiley, 1982.

[163] V. V. Datsyuk, "A generalization of the mie theory for a sphere with spatially dispersive permittivity," *Ukr. J. Phys.*, vol. 56, no. 2, pp. 122–129, 2011.

[164] M. S. Zhdanov, *Integral Transforms in Geophysics*. Springer-Verlag, 1988.

[165] D. Gall, "Electron mean free path in elemental metals," *J. Appl. Phys.*, vol. 119, no. 8, p. 085101, 2016.

[166] N. A. Mortensen, S. Raza, M. Wubs, T. Søndergaard, and S. I. Bozhevolnyi, "A generalized non-local optical response theory for plasmonic nanostructures," *Nat. Comm.*, vol. 5, no. 3809, 2014.

[167] J. Butet, G. Bachelier, I. Russier-Antoine, C. Jonin, E. Benichou, and P. F. Brevet, "Interference between selected dipoles and octupoles in the optical second-harmonic generation from spherical gold nanoparticles," *Phys. Rev. Lett.*, vol. 105, p. 077401, 2010.

[168] W. Wasylkiwskyj, *Signals and Transforms in Linear Systems Analysis*. New York: Springer, 2013.

[169] H. Chew, P. J. McNulty, and M. Kerker, "Model for raman and fluorescent scattering by molecules embedded in small particles," *Phys. Rev. A*, vol. 13, pp. 396–404, 1976.

[170] A. S. Davydov, *Quantum Mechanics*. Pergamon Press, 1965.

[171] T. F. Heinz, "Second-order nolinear optical effects at surfaces and interfaces," in *Nonlinear surface electromagnetic phenomena* (H. Ponath and G. Stegeman, eds.), Amsterdam: Elsevier, 1991.

[172] A. D. Rakić, "Algorithm for the determination of intrinsic optical constants of metal films: application to aluminum," *Applied optics*, vol. 34, no. 22, pp. 4755–4767, 1995.

[173] S. Roke, M. Bonn, and A. V. Petukhov, "Nonlinear optical scattering: The concept of effective susceptibility," *Phys. Rev. B*, vol. 70, p. 115106, 2004.

[174] F. X. Wang, F. J. Rodríguez, W. M. Albers, R. Ahorinta, J. E. Sipe, and M. Kauranen, "Surface and bulk contributions to the second-order nonlinear optical response of a gold film," *Phys. Rev. B*, vol. 80, p. 233402, 2009.

[175] A. Bostrom, G. Kristensson, and S. Strom, "Transformation properties of plane, spherical and cylindrical scalar and vector wavefunctions," in *Field Representations and Introduction to Scattering* (V. V. Varadan, A. Lakhtakia, and V. K. Varadan, eds.), Elsevier Science Publisher, 1991.

[176] C. Cirací, E. Poutrina, M. Scalora, and D. R. Smith, "Second-harmonic generation in metallic nanoparticles: Clarification of the role of the surface," *Phys.Rev. B*, vol. 86, p. 115451, 2012.

[177] G. Bachelier, J. Butet, I. Russier-Antoine, C. Jonin, E. Beninchou, and P. F. Brevet, "Origin of optical second-harmonic generation in spherical gold nanoparticles: Local surface and nonlocal bulk contributions," *Phys. Rev. B*, vol. 82, p. 235403, 2010.

[178] J. I. Dadap, J. Shan, and T. F. Heinz, "Theory of optical second-harmonic generation from a sphere of centrosymmetric material: small-particle limit," *J. Opt. Soc. Am. B*, vol. 21, pp. 1328–1348, 2004.

[179] B. R. W., *Nonlinear optics*. Academic Press, 3 ed., 2008.

[180] J. E. Sipe, V. C. Y. So, M. Fukui, and G. I. Stegeman, "Analysis of second-harmonic generation at metal surfaces," *Phys. Rev. B*, vol. 21, pp. 4389–4402, May 1980.

[181] P. A. Franken, A. E. Hill, C. W. Peters, and G. Weinreich, "Generation of optical harmonics," *Phys. Rev. Lett.*, vol. 7, pp. 118–119, Aug 1961.

[182] A. D. Rakić, A. B. Djurišić, J. M. Elazar, and M. L. Majewski, "Optical properties of metallic films for vertical-cavity optoelectronic devices," *Appl. Opt.*, vol. 37, pp. 5271–5283, Aug 1998.

[183] J. Butet, J. Duboisset, G. Bachelier, I. Russier-Antoine, E. Benichou, C. Jonin, and P. F. Brevet, "Optical second harmonic generation of single metallic nanoparticles embedded in a homogeneous medium," *Nano Lett.*, vol. 10, no. 5, pp. 1717–1721, 2010.

[184] I. Russier-Antoine, E. Benichou, G. Bachelier, C. Jonin, and P. F. Brevet, "Multipolar contributions of the second harmonic generation from silver and gold nanoparticles," *J. Phys. Chem. C*, vol. 111, no. 26, pp. 9044–9048, 2007.

[185] A. Capretti, E. F. Pecora, C. Forestiere, L. Dal Negro, and G. Miano, "Size-dependent second-harmonic generation from gold nanoparticles," *Phys. Rev. B*, vol. 89, p. 125414, Mar 2014.

[186] J. Rudnick and E. A. Stern, "Second-harmonic radiation from metal surfaces," *Phys. Rev. B*, vol. 4, pp. 4274–4290, Dec 1971.

[187] G. S. Agarwal, "Quantum electrodynamics in the presence of dielectrics and conductors. i. electromagnetic-field response functions and black-body fluctuations in finite geometries," *Phys. Rev. A*, vol. 11, pp. 230–242, 1975.

[188] S. Scheel, L. Knöll, and D.-G. Welsch, "Qed commutation relations for inhomogeneous kramers-kronig dielectrics," *Phys. Rev. A*, vol. 58, pp. 700–706, 1998.

[189] S. Scheel, L. Knöll, and D.-G. Welsch, "Spontaneous decay of an excited atom in an absorbing dielectric," *Phys. Rev. A*, vol. 60, pp. 4094–4104, 1999.

[190] H. T. Dung, S. Y. Buhmann, L. Knöll, D.-G. Welsch, S. Scheel, and J. Kästel, "Electromagnetic-field quantization and spontaneous decay in left-handed media," *Phys. Rev. A*, vol. 68, p. 043816, 2003.

[191] J. J. Bowman, T. B. A. Senior, P. L. E. Uslenghi, and J. S. Asvestas, *Electromagnetic and acoustic scattering by simple shapes*. North-Holland Pub. Co., 1970.

[192] M. Wubs, L. G. Suttorp, and A. Lagendijk, "Multiple-scattering approach to interatomic interactions and superradiance in inhomogeneous dielectrics," *Phys. Rev. A*, vol. 70, p. 053823, 2004.

[193] G. Boudarham and M. Kociak, "Modal decompositions of the local electromagnetic density of states and spatially resolved electron energy loss probability in terms of geometric modes," *Phys. Rev. B*, vol. 85, p. 245447, 2012.

[194] C. Sauvan, J. P. Hugonin, I. S. Maksymov, and P. Lalanne, "Theory of the spontaneous optical emission of nanosize photonic and plasmon resonators," *Phys. Rev. Lett.*, vol. 110, p. 237401, 2013.

[195] M. B. Doost, W. Langbein, and E. A. Muljarov, "Resonant-state expansion applied to three-dimensional open optical systems," *Phys. Rev. A*, vol. 90, p. 013834, 2014.

[196] G. M. Akselrod, C. Argyropoulos, T. B. Hoang, C. Cirací, C. Fang, J. Huang, D. R. Smith, and M. H. Mikkelsen, "Probing the mechanisms of large purcell enhancement in plasmonic nanoantennas," *Nature Phot,*, vol. 8, pp. 835–840, 2014.

[197] A. W. Schell, P. Engel, J. F. M. Werra, C. Wolff, K. Busch, and O. Benson, "Scanning single quantum emitter fluorescence lifetime imaging: Quantita-

tive analysis of the local density of photonic states," *Nano Lett.*, vol. 14, pp. 2623–2627, 2014.

[198] C. V. Vlack, P. Yao, and S. Hughes, "Optical forces between coupled plasmonic nanoparticles near metal surfaces and negative index material waveguides," *Phys. Rev. B*, vol. 83, p. 245404, 2011.

[199] W. Vogel and D.-G. Welsh, *Quantum Optics*. Weinheim: Wiley-VCH, 3rd ed., 2006.

[200] E. Eremina, Y. Eremin, and T. Wriedt, "Analysis of the light scattering properties of a gold nanorod on a plane surface via discrete sources method," *Optics Communications*, vol. 273, pp. 278–285, 2007.

[201] E. M. Purcell, "Spontaneous emission probabilities at radio frequencies," *Phys. Rev.*, vol. 69, p. 681, 1946.

[202] R. Carminati, J.-J. Greffet, C. Henkel, and J. M. Vigoureux, "Radiative and non-radiative decay of a single molecule close to a metallic nanoparticle," *Opt. Commun.*, vol. 261, no. 2, pp. 368 – 375, 2006.

[203] W. E. Lamb and R. C. Retherford, "Fine structure of the hydrogen atom by a microwave method," *Phys. Rev.*, vol. 72, pp. 241–243, Aug 1947.

[204] H. A. Bethe, "The electromagnetic shift of energy levels," *Phys. Rev.*, vol. 72, p. 339, 1947.

[205] S. Viarbitskaya, A. Teulle, R. Marty, J. Sharma, C. Girard, A. Arbouet, and E. Dujardin, "Tailoring and imaging the plasmonic local density of states in crystalline nanoprisms," *Nat. Materials*, vol. 12, pp. 426–432, 2013.

[206] F. J. G. de Abajo and M. Kociak, "Probing the photonic local density of states with electron energy loss spectroscopy," *Phys. Rev. Lett.*, vol. 100, p. 106804, 2008.

[207] K. Joulain, R. Carminati, J. Mulet, and J. Greffet, "Definition and measurement of the local density of electromagnetic states close to an interface," *Phys. Rev. B*, vol. 68, p. 245405, 2003.

[208] A. Narayanaswamy and G. Chen, "Dyadic green's functions and electromagnetic local density of states," *J. Quant. Spectrosc. Radiat. Transfer*, vol. 111, pp. 1877–1884, 2010.

[209] M. Pelton, "Modified spontaneous emission in nanophotonic structures," *Nat. Photon.*, vol. 9, pp. 427–435, 2015.

[210] A. Volkmer, K. Wynne, and D. J. S. Birch, "Protein detection by optical shift of a resonant microcavity," *Chem. Phys. Letts.*, vol. 299, pp. 395–402, 1999.

[211] C. D. McGuinness, K. Sagoo, D. McLoskey, and D. J. S. Birch, "A new subnanosecond LED at 280 nm: application to protein fluorescence," *Meas. Sci. Technol.*, vol. 15, pp. L19–L22, 2004.

[212] G. Toscano, J. Straubel, A. Kwiatkowski, C. Rockstuhl, F. Evers, H. Xu, N. A. Mortensen, and M. Wubs, "Resonance shifts and spill-out effects in self-consistent hydrodynamic nanoplasmonics," *Nat. Commun.*, vol. 6, p. 7132, 2015.

[213] W. Zhu, R. Esteban, A. G. Borisov, J. J. Baumberg, P. Nordlander, H. J. Lezec, J. Aizpurua, and K. B. Crozier, "Quantum mechanical effects in plasmonic structures with subnanometre gaps," *Nat. Commun.*, vol. 7, p. 11495, 2016.

[214] D. O. Sigle, J. Mertens, L. O. Herrmann, R. W. Bowman, S. Ithurria, B. Dubertret, Y. Shi, H. Y. Yang, C. Tserkezis, J. Aizpurua, and J. J. Baumberg, "Monitoring morphological changes in 2d monolayer semiconductors using atom-thick plasmonic nanocavities," *ACS Nano*, vol. 9, no. 1, pp. 825–830, 2015.

[215] I. Malitson, "Interspecimen comparison of the refractive index of fused silica," *J. Opt. Soc. Am.*, vol. 55, pp. 1205–1209, 1965.

[216] M. A. Noginov, G. Zhu, A. M. Belgrave, R. Bakker, V. M. Shalaev, E. E. Narimanov, S. Stout, E. Herz, T. Suteewong, and U. Wiesner, "Demonstration of a spaser-based nanolaser," *Nature*, vol. 460, pp. 1110–1113, 2009.

[217] M. Khajavikhan, A. Simic, M. Katz, J. H. Lee, B. Slutsky, A. Mizrahi, V. Lomakin, and Y. Fainman, "Thresholdless nanoscale coaxial lasers," *Nature*, vol. 482, pp. 204–207, 2012.

[218] A. L. Aden and M. Kerker, "Scattering of electromagnetic waves from two concentric spheres," *J. Appl. Phys.*, vol. 22, pp. 1242–1246, 1951.

[219] J. Lock and P. Laven, "Understanding light scattering by a coated sphere part 1: Theoretical considerations," *J. Opt. Soc. Am. A*, vol. 29, pp. 1489–1497, 2012.

[220] T. K. Hakala, H. T. Rekola, A. I. Väkeväinen, J.-P. Martikainen, M. NeČada, A. Moilanen, and P. Törmä, "Lasing in dark and bright modes of a finite-sized plasmonic lattice," *Nat. Commun.*, vol. 8, no. 2, p. 13687, 2017.

[221] E. Anderson, Z. Bai, C. Bischof, S. Blackford, J. Demmel, J. Dongarra, J. Du Croz, A. Greenbaum, S. Hammarling, A. McKenney, and D. Sorensen, *LAPACK Users' Guide*. Philadelphia, PA: Society for Industrial and Applied Mathematics, third edition ed., 1999.

[222] A. Sommerfeld, "Über die ausbreitung der wellen in der drahtlosen telegraphie," *Ann. Phys.*, vol. 333, no. 4, pp. 665 –736, 1909.

[223] W. C. Chew, ed., *Waves and Fields in Inhomogenous Media*. Wiley-IEEE Press, 1999.

[224] G. Panasyuk, J. Schotland, and V. Markel, "Short-distance expansion for the electromagnetic half-space Green's tensor: General results and an ap-

plication to radiative lifetime computations," *J. Phys. A: Math. Theor.*, vol. 42, no. 27, 2009.

[225] A. A. Maradudin and D. L. Mills, "Scattering and absorption of electromagnetic radiation by a semi-infinite medium in the presence of surface roughness," *Phys. Rev. B*, vol. 11, pp. 1392–1415, Feb 1975.

[226] "Fortran adaptive integration routines." `http://www.netlib.org/quadpack`.

[227] L. Mandel and E. Wolf, eds., *Optical Coherence and Quantum Optics*. New York: Cambridge University Press, 1995.